



**Politecnico  
di Torino**



**TECHNISCHE  
UNIVERSITÄT  
DARMSTADT**

Politecnico di Torino

Corso di Laurea Magistrale in Ingegneria Aerospaziale, Aerostrutture  
A.a. 2021/2022  
Sessione di Laurea Ottobre 2022

**Modeling and validation of lightweight  
lattice structures for high specific energy  
absorption**

Relatore:  
Prof. Giorgio De Pasquale

Co-tutor presso Politecnico di Torino:  
Research Assistant Antonio Coluccia

Tutor presso TU Darmstadt:  
Prof. Christian Mittelstedt

Co-tutor presso TU Darmstadt:  
Research Assistant Guillaume Meyer

Candidato:  
Stefania Liseni  
Matr. s288785



To my mother,  
my every success will be yours.





The numerical and experimental research activities, required for this thesis, were carried out at the Institute Konstruktiver Leichtbau und Bauweisen, Technische Universität Darmstadt.



# Abstract

The introduction of lattice structures, in order to reduce weight and increase structural performances, is becoming more and more requested in fields such as aerospace, automotive and biomedical. These challenges are satisfied by the advent of innovative additive manufacturing techniques, which have enabled not only the realization of complex structures, but also the implementation of alloys whose characteristics can be well suited to demanding fields of application. Within the scope of this thesis, the main characteristics of lattices are explored, outlining the differences according to topology, arrangement and density of unit cells. The main aim is the implementation of a structural optimization method by which, based on the above-mentioned properties, each different configuration shows significant improvements in energy absorption (EA). A central part of the work is the analysis of how the topology impacts mechanical and energy performances, whereby lattice samples are tested using FEA (Ansys), carrying out static simulations. The material, AlSi10Mg, follows a bilinear model and it is currently one of the most used for additive manufacturing of light-weight lattice structures.

Identified the basic properties, the ultimate goal has been to improve them through structural optimization, based on the stress field within the specimens, with considerations of manufacturability to ensure desired printing quality. The optimization is performed through the implementation of a Matlab code, that aims to construct two processes of thickness reassignment, based on the homogenization of the stress field. The same code is able to extrapolate 3D databases containing all mechanical and energy characteristics, automatically performing a static bilinear analysis of the specimens, with reduced computational time. The results obtained are validated again by means of software and ultimately through the experimental campaign.

As achievements, the implementation of the two processes leads to an improvement of the stiffness and, at the same time, to a homogenization of the Von-Mises stress (comparing the models with the uniform original design), achieving good control on the cracking mechanism and generating a well-determined *failure path*. The main final gain concerns energy absorption, as both in specific (SEA) and volumetric (VEA) terms, significant percentages of increment are highlighted, satisfying the fundamental requirement for many of the applications of interest.

# Contents

<b>1</b>	<b>Introduction</b>	<b>1</b>
1.1	Cellular materials	1
1.1.1	Lattice structures	3
1.1.2	Mechanical properties	5
1.1.3	Manufacturing techniques	7
1.1.4	Applications	9
1.2	Main purposes	10
<b>2</b>	<b>General models</b>	<b>12</b>
2.1	Material	12
2.2	Selection of specimen configurations	14
2.3	Mesh-sensitivity analysis	14
2.3.1	Analysis settings	15
2.3.2	Results	15
2.4	Bilinear static simulation of the 1D beam model	17
2.4.1	Results	17
2.5	Validation of the 1D beam models	19
2.5.1	First comparison	19
2.5.2	Second comparison	22
<b>3</b>	<b>Bilinear static simulations</b>	<b>24</b>
3.1	General configurations	24
3.2	Samples with (10,10,10) cells along (x,y,z)	25
3.2.1	Finite element modelling	25
3.2.2	Boundary conditions and loads	26

3.2.3	Results	26
3.2.4	Stress state analysis of the samples	30
3.2.5	Stress field	32
3.2.6	Deformation planes	34
3.2.7	Qualitative validation of the results	35
3.3	Samples with (10,10,15) cells along (x,y,z)	38
3.3.1	Boundary conditions and loads	38
3.3.2	Results	38
3.3.3	Stress field	40
3.4	Samples with (10,10,20) cells along (x,y,z)	41
3.4.1	Boundary conditions and loads	42
3.4.2	Results	42
3.4.3	Stress field	43
3.5	Middle region evaluation	46
3.6	Effect of variable imposed displacement	46
3.7	Size effects	50
3.8	Sensitivity analysis for accuracy study	51
3.9	Computational time for the three sample sizes	53
<b>4</b>	<b>Topological optimization of the samples</b>	<b>55</b>
4.1	Data extraction in table format	56
4.2	Optimization of diameters	58
4.3	Optimization processes	59
4.3.1	First process	59
4.3.2	Second process	62
4.4	Implementation of optimization processes: results	63
4.4.1	Threshold equal to 25% above the mean value	63
4.4.2	Threshold equal to the minimum stress value	67
4.4.3	Threshold equal to the average	70
4.5	Energy extraction in table format	73
<b>5</b>	<b>Limit imposed for 3D printing (SLM)</b>	<b>74</b>
5.1	Results for the three cases	75

5.1.1	Threshold equal to 25% above the mean value	75
5.1.2	Threshold equal to the minimum stress value	77
5.1.3	Threshold equal to the mean value	80
5.2	Verification of the Matlab optimization approaches	83
5.2.1	Validation for BCC sample graded by Process 1	83
5.2.2	Validation for BCC sample graded by Process 2	86
5.2.3	Validation for BCCZ sample graded by Process 1	87
5.2.4	Validation for BCCZ sample graded by Process 2	90
5.3	Comparison of the computational costs	92
<b>6</b>	<b>Experimental tests</b>	<b>93</b>
6.1	Experimental Setup	95
6.1.1	Density measurement	97
6.1.2	Static compression testing	99
6.2	Data processing	99
6.3	Stress-strain curves	100
6.3.1	Average representation of stress-strain curves	103
6.4	Young modulus	105
6.5	Yield point	105
6.6	Plateau region	106
6.7	Densification region	107
6.8	Energy absorption	109
6.8.1	Macro areas of characterization	111
6.8.2	Identification of the macro-behavior	113
6.9	Overall comparative analysis of the results	115
<b>7</b>	<b>Conclusions</b>	<b>120</b>
	<b>Bibliography</b>	<b>122</b>
<b>A</b>	<b>Stress extraction in table format</b>	<b>130</b>
A.1	Initial uniform configuration	130
A.2	Optimized samples	134
A.2.1	Threshold equal to the mean value - Process 1 and 2	134

<b>B Optimized samples: new thicknesses extraction in table format</b>	<b>139</b>
B.1 Threshold equal to the mean value - Process 1 . . . . .	139
B.2 Threshold equal to the mean value - Process 2 . . . . .	141
<b>C Optimized samples: SEA extraction in table format</b>	<b>143</b>
C.1 Threshold equal to the mean value - Process 1 . . . . .	143
C.2 Threshold equal to the mean value - Process 2 . . . . .	145
<b>D Optimized samples: VEA extraction in table format</b>	<b>147</b>
D.1 Threshold equal to the mean value - Process 1 . . . . .	147
D.2 Threshold equal to the mean value - Process 2 . . . . .	149
<b>Acknowledgments</b> . . . . .	150

# List of Figures

1.1	Cellular solids classification, [1]. . . . .	2
1.2	The idealization of 3D structure of open and closed cell foams, [2]. . . . .	2
1.3	Classification of lattice structures: (a) random lattice structures; (b) periodic lattice structures; (c) pseudo periodic lattice structures, [3]. . . . .	3
1.4	(a) BCC, (b) BCCZ, (c) FCC, (d) FCCZ, (e) FBCC, (f) FBCCZ - unit cell topology.	4
1.5	Examples of (a) bending-dominated and (b) stretch-dominated structures, [4].	5
1.6	General compressive behaviour of stretch and bending-dominated lattice struc- tures, [5]. . . . .	6
1.7	Manufacturing methods for lattice structures, [6]. . . . .	8
1.8	Anti-icing system of an aircraft wing, [7]. . . . .	9
1.9	Medical implant using lattice structure, [8]. . . . .	10
1.10	Micro-heat exchanger (a) schematic of operation, (b) image of electroplated micro-lattice with solder at node, [9]. . . . .	10
2.1	Material bilinear behaviour. . . . .	13
2.2	Samples with four unit cells for each side. . . . .	14
2.3	General BCs and imposed displacement for 4x4x4 (cells) samples. . . . .	15
2.4	Trends of Force Reaction and Deformation Probe output, considering different element sizes (range values). . . . .	16
2.5	Comparison of the sigma-stress curves of the 4x4x4 cell samples. . . . .	17
2.6	EA and SEA of the 4x4x4 (cells for each dimension) samples. . . . .	18
2.7	VEA of the 4x4x4 (cells for each dimension) samples. . . . .	18
2.8	(a) BCC, (b) BCCZ, (c) FCC, (d) FCCZ, (e) FBCC, (f) FBCCZ, single RVEs chosen for the confrontations. . . . .	20
2.9	Overlaid comparison for SEA for the 1D beam and 3D models ([10]). . . . .	20
2.10	Overlaid comparison for VEA for the 1D beam and 3D models ([10]). . . . .	21



2.11	Stress strain curves for (a) the 1D and (b) 3D models, [11].	22
2.12	Overlaid comparison for SEA for the 1D beam and 3D models, [11].	23
3.1	Sample configurations 30x30x30 mm.	25
3.2	BCs and load for the selected samples.	26
3.3	Relative Density and Force reaction along z-axis of the samples	27
3.4	Stress-strain curves for the six samples of dimension 30x30x30 mm.	29
3.5	EA and SEA for the samples of dimensions 30x30x30 mm.	30
3.6	VEA for the samples of dimensions 30x30x30 mm.	30
3.7	User define output equal to the absolute value of the maximum combined stress for a beam.	31
3.8	Von-Mises stress output in a 3D discretization.	31
3.9	Stress field for BCC and BCCZ samples with 10x10x10 configuration.	32
3.10	Stress field for FCC and FCCZ samples with 10x10x10 configuration.	32
3.11	Stress field for FBCC and FBCCZ samples with 10x10x10 configuration.	33
3.12	Qualitative schematizations of the stress fields for the six 10x10x10 samples.	33
3.13	Total deformations of the six tested samples.	34
3.14	Deformation planes of the six 10x10x10 samples.	35
3.15	Characteristics and topologies. assumed in [12]	36
3.16	Overlaid comparison for SEA for the two 1D beam models, [11].	36
3.17	Overlaid comparison for VEA for the two 1D beam models, [11].	36
3.18	Von Mises Stress for BCC and BCCZ samples, [12].	37
3.19	Von Mises Stress for FCC and FCCZ samples, [12].	37
3.20	Von Mises Stress for FBCCZ sample, [12].	37
3.21	Stress-strain curve for the six samples of dimension 30x30x45 mm.	39
3.22	EA and SEA of dimension 30x30x45 mm.	39
3.23	VEA for the six samples of dimension 30x30x45 mm.	39
3.24	Stress field for BCC and BCCZ samples with 10x10x15 configuration.	40
3.25	Stress field for FCC and FCCZ samples with 10x10x15 configuration.	40
3.26	Stress field for FBCC and FBCCZ samples with 10x10x15 configuration.	41
3.27	Qualitative schematizations of the stress fields for the six 10x10x15 samples.	41
3.28	Stress-strain curve for the six samples of dimensions 30x30x60 mm.	42
3.29	EA and SEA for the six samples of dimensions 30x30x60 mm.	43

3.30	VEA for the six samples of dimensions 30x30x60 mm.	43
3.31	Stress field for BCC and BCCZ samples with 10x10x20 configuration.	44
3.32	Stress field for FCC and FCCZ samples with 10x10x20 configuration.	44
3.33	Stress field for FBCC and FBCCZ samples with 10x10x20 configuration.	45
3.34	Qualitative schematizations of the stress fields for the six 10x10x20 samples.	45
3.35	Case 1, Von Mises Stress and corresponding qualitative schematization.	47
3.36	Case 2, Von Mises Stress and corresponding qualitative schematization.	48
3.37	Case 3, Von Mises Stress and corresponding qualitative schematization.	48
3.38	Comparison of the stress-strain curves for the case 1, 2 and 3.	49
3.39	Comparison of (a) Force Reaction and (b) EA, for the Case 1, 2 and 3.	49
3.40	Comparison of (a) SEA and (b) VEA, for the Case 1, 2 and 3.	50
3.41	Stress-strain curve, varying mesh size.	52
3.42	EA and SEA, varying mesh size.	52
3.43	VEA, varying mesh size.	52
3.44	BCC stress field for a mesh size of (a) 0.1 mm and (b) 1.5 mm.	53
4.1	Stress-strain curve of graded lattice structures, [13].	55
4.2	Comparison of deformation modes, [14].	56
4.3	Characteristic planes for the representation of mechanical and energetic prop- erties within samples (extraction of 2D databases from the global 3D one).	57
4.4	Workflow of the process in Matlab.	61
4.5	Workflow of the process in Matlab - implemented formulas.	62
4.6	Planes numbering system.	64
5.1	Geometry of the graded sample post optimization - BCC1.	84
5.2	Comparison of the masses - BCC1.	84
5.3	Stress field of the graded sample post optimization - BCC1.	85
5.4	Comparison of SEA and VEA - BCC1.	85
5.5	Geometry of the graded sample post optimization - BCC2.	86
5.6	Comparison of the masses - BCC2.	86
5.7	Stress field of the graded sample post optimization - BCC2.	87
5.8	Comparison of SEA and VEA - BCC2.	87
5.9	Geometry of the graded sample post optimization - BCCZ1.	88

5.10	Comparison of the masses - BCCZ1.	88
5.11	Stress field of the graded sample post optimization - BCCZ1.	89
5.12	Comparison of SEA and VEA - BCCZ1.	89
5.13	Geometry of the graded sample post optimization.	90
5.14	Comparison of the masses - BCCZ2.	90
5.15	Stress field of the graded sample post optimization - BCCZ2.	91
5.16	Comparison of SEA and VEA - BCCZ2.	91
6.1	Numbering of test specimens on the platforms.	95
6.2	(a) Vacuum Desiccator with tube and stopcock. (b) Ultrasonic Cleaner.	96
6.3	(a) Experimental apparatus for density measurement and (b) SLM Printer EOS M 290.	96
6.4	Temperature cycle for the heat treatment.	97
6.5	Density values of the samples.	98
6.6	ZwickRoell compression testing machines.	99
6.7	Stress-strain curves of all BCC samples until a strain equal to numerical analysis.	101
6.8	Stress-strain curves of all BCC samples until a strain equal to 0.5.	102
6.9	Stress-strain curves of all BCCZ samples until a strain equal to numerical analysis.	102
6.10	Stress-strain curves of all BCCZ samples until a strain equal to 0.5.	103
6.11	Average representation of stress-strain curves of all (a) BCC samples and (b) BCCZ samples.	103
6.12	Average representation of stress-strain curves of all the samples.	104
6.13	Young modulus averaged for the six tested configurations.	105
6.14	Yield stress and strain.	106
6.15	Initial plateau stress and strain.	107
6.16	The energy absorption efficiency for BCC and BCC1 samples.	107
6.17	The energy absorption efficiency for BCC2 and BCCZ samples.	108
6.18	The energy absorption efficiency for BCCZ1 and BCCZ2 samples.	108
6.19	Densification stress and strain.	109
6.20	Energy absorption and specific energy absorption.	110
6.21	Volumetric energy absorption.	110
6.22	Energy absorption and specific energy absorption until the densification point.	110

6.23	Volumetric energy absorption until the densification point.	111
6.24	Stress-strain curve schematization - BCC and BCC1.	112
6.25	Stress-strain curve schematization - BCC2 and BCCZ.	112
6.26	Stress-strain curve schematization - BCCZ1 and BCCZ2.	112
6.27	Mass values for all the configurations.	117
6.28	Mass values for all the configurations.	117
6.29	SEA values for all the configurations.	118
6.30	SEA values for all the configurations.	118
6.31	VEA values for all the configurations.	118
6.32	VEA values for all the configurations.	119
A.1	Central plane (x,y) and upper plane (x,y) for BCC samples.	130
A.2	Lateral external plane (y,z) and diagonal plane for BCC samples.	130
A.3	Central plane (x,y) and upper plane (x,y) for BCCZ samples.	131
A.4	Lateral external plane (y,z) and diagonal plane for BCCZ samples.	131
A.5	Central plane (x,y) and upper plane (x,y) for FCC samples.	131
A.6	Lateral external plane (y,z) and diagonal plane for FCC samples.	132
A.7	Central plane (x,y) and upper plane (x,y) for FCCZ samples.	132
A.8	Lateral external plane (y,z) and diagonal plane for FCCZ samples.	132
A.9	Central plane (x,y) and upper plane (x,y) for FBCC samples.	133
A.10	Lateral external plane (y,z) and diagonal plane for FBCC samples.	133
A.11	Central plane (x,y) and upper plane (x,y) for FBCCZ samples.	133
A.12	Lateral external plane (y,z) and diagonal plane for FBCCZ samples.	134
A.13	Central plane (x,y) and upper plane (x,y) - BCC optimized sample.	134
A.14	Lateral external plane (y,z) and diagonal plane - BCC optimized sample.	135
A.15	Central plane (x,y) and upper plane (x,y) - BCCZ optimized sample.	135
A.16	Lateral external plane (y,z) and diagonal plane - BCCZ optimized sample.	135
A.17	Central plane (x,y) and upper plane (x,y) - FCC optimized sample.	136
A.18	Lateral external plane (y,z) and diagonal plane - FCC optimized sample.	136
A.19	Central plane (x,y) and upper plane (x,y) - FCCZ optimized sample.	136
A.20	Lateral external plane (y,z) and diagonal plane - FCCZ optimized sample.	137
A.21	Central plane (x,y) and upper plane (x,y) - FBCC optimized sample.	137
A.22	Lateral external plane (y,z) and diagonal plane - FBCC optimized sample.	137

A.23 Central plane (x,y) and upper plane (x,y) - FBCCZ optimized sample. . . . .	138
A.24 Lateral external plane (y,z) and diagonal plane - FBCCZ optimized sample. . .	138
B.1 Diameter of struts per cell - BCC1. . . . .	139
B.2 Diameter of struts per cell - BCCZ1. . . . .	140
B.3 Diameter of struts per cell - BCC2. . . . .	141
B.4 Diameter of struts per cell - BCCZ2. . . . .	142
C.1 SEA per cell - BCC1. . . . .	143
C.2 SEA per cell - BCCZ1. . . . .	144
C.3 SEA per cell - BCC2. . . . .	145
C.4 SEA per cell - BCCZ2. . . . .	146
D.1 VEA per cell - BCC1. . . . .	147
D.2 VEA per cell - BCCZ1. . . . .	148
D.3 VEA per cell - BCC2. . . . .	149
D.4 VEA per cell - BCCZ2. . . . .	150

# List of Tables

2.1	Results of the sensitivity analysis.	16
2.2	Results from bilinear static analyses on the 4x4x4 samples.	18
3.1	Physical properties from bilinear static analyses.	27
3.2	General results from bilinear static analyses for the 30x30x30 mm samples.	28
3.3	General results from bilinear static analyses for the 30x30x45 mm samples.	38
3.4	General results from bilinear static analyses for the 30x30x60 mm samples.	42
3.5	Dimension along (x,y,z) of the middle stress band.	46
3.6	Computer technical specifications used for the analyses.	54
3.7	Time costs for all the static analyses done.	54
4.1	A and B values for relative density based on topology.	60
4.2	Maximum and minimum thicknesses for a threshold of 25%.	64
4.3	Masses for the uniform, graded by process 1 and 2 samples, with a threshold equal to the 25%.	65
4.4	SEA for the uniform, graded by process 1 and 2 samples, with a threshold equal to the 25%.	65
4.5	VEA for the uniform, graded by process 1 and 2 samples, with a threshold equal to the 25%.	65
4.6	Percentages of increments of SEA e VEA, threshold equal to the 25%.	66
4.7	Percentages of increments of the mass, threshold equal to the 25%.	66
4.8	Maximum and minimum thicknesses for the lower threshold.	67
4.9	Masses for the uniform, graded by process 1 and 2 samples, with the minimum threshold.	68
4.10	SEA for the uniform, graded by process 1 and 2 samples, with the minimum threshold.	68

4.11 VEA for the uniform, graded by process 1 and 2 samples, with the minimum threshold.	68
4.12 Percentages of increments of SEA and VEA, minimum threshold.	69
4.13 Percentages of increments of the mass, minimum threshold.	69
4.14 Maximum and minimum thicknesses for a threshold equal to the average value of the stress.	70
4.15 Masses for the uniform, graded by process 1 and 2 samples, with a threshold equal to the average value of the stress.	71
4.16 SEA for the uniform, graded by process 1 and 2 samples, with a threshold equal to the average value of the stress.	71
4.17 VEA for the uniform, graded by process 1 and 2 samples, with a threshold equal to the average value of the stress.	72
4.18 Percentages of increments of SEA e VEA, threshold equal to the average value of the stress.	72
4.19 Percentages of increments of the mass, threshold equal to the average value of the stress.	72
5.1 Upper limit of diameters of each unit cell - control to insert for the optimization processes.	74
5.2 Maximum and minimum thicknesses for a threshold of 25%, with the upper limit.	75
5.3 Masses for the uniform, graded by process 1 and 2 samples, with a threshold equal to the 25% considering the upper limit.	76
5.4 SEA for the uniform, graded by process 1 and 2 samples, with a threshold equal to the 25% considering the upper limit.	76
5.5 VEA for the uniform, graded by process 1 and 2 samples, with a threshold equal to the 25% considering the upper limit.	76
5.6 Percentages of increments of SEA and VEA, threshold equal to the 25% and upper limit imposed.	77
5.7 Percentages of increments of the mass, threshold equal to the 25% and upper limit imposed.	77
5.8 Maximum and minimum thicknesses for the minimum threshold selected, with the upper limit.	78

5.9	Masses for the uniform, graded by process 1 and 2 samples, with the minimum threshold, considering the upper limit. . . . .	78
5.10	SEA for the uniform, graded by process 1 and 2 samples, with the minimum threshold, considering the upper limit. . . . .	79
5.11	VEA for the uniform, graded by process 1 and 2 samples, with the minimum threshold, considering the upper limit. . . . .	79
5.12	Percentages of increments of SEA and VEA for the minimum threshold and the upper limit imposed. . . . .	79
5.13	Percentages of increments of the mass for the minimum threshold and the upper limit imposed. . . . .	80
5.14	Maximum and minimum thicknesses for a threshold equal to the average value of the stress, with the upper limit. . . . .	80
5.15	Masses for the uniform, graded by process 1 and 2 samples, with a threshold equal to the average value of the stress, with the upper limit. . . . .	81
5.16	SEA for the uniform, graded by process 1 and 2 samples, with a threshold equal to the average value of the stress, with the upper limit. . . . .	81
5.17	VEA for the uniform, graded by process 1 and 2 samples, with a threshold equal to the average value of the stress, with the upper limit. . . . .	82
5.18	Percentages of increments of SEA and VEA, threshold equal to the average value of the stress, with the upper limit. . . . .	82
5.19	Percentages of increments of the mass, threshold equal to the average value of the stress, with the upper limit. . . . .	82
5.20	Computer technical specifications used for the analyses. . . . .	92
5.21	Computational cost in time for the Ansys and Matlab code static analyses. . .	92
6.1	Sample typologies selected for the experimental tests. . . . .	94
6.2	Maximum and minimum thicknesses for a threshold equal to the mean value (Case 3 with the upper limit), implemented to realise '.stl' files. . . . .	94
6.3	Mass in air, mass in water and density. . . . .	98
6.4	Notations to identify the classification regions. . . . .	111
6.5	Failure mode of specimens during static compression tests. . . . .	114
6.6	Values of specimen mass obtained using Ansys, Matlab code and experimental tests. . . . .	116



6.7	SEA obtained using Ansys, Matlab code and experimental tests.	. . . . .	116
6.8	VEA obtained using Ansys, Matlab code and experimental tests.	. . . . .	116

# Chapter 1

## Introduction

The recent development of Additive Manufacturing techniques, such as FDM (Fused Deposition Modeling), EBM (Electron Beam Melting), SLS (Selective Laser Sintering) and SLM (Selective Laser Melting), has led to great opportunities and changes, regarding the introduction of more efficient structures than traditional ones. The possibility of innovative designs is closely related to the great advantages that such manufacturing methodologies bring, as the possibility of recreating complex component shapes, difficult to reproduce using other traditional processes. In addition to increasingly elaborate designs, 3D printing methods have contributed to reduce the weight-strength relation, broadening the scope of light-weight models like functionally graded materials and lattice structures.

### 1.1 Cellular materials

The growing demand for highly stiff, strong and light-weight structural component, with energy absorption capabilities, is an important requirement in many field of application. In this regard, cellular materials can provide exactly these properties as promising materials for lightweight, efficient, and innovative design of engineering structures. Their composition is given by a solid part, constituted by struts or plates connected at their edge, and void networks. Cellular solids can be classified into two macro-categories, outlined in Figure 1.1, where stochastic (foam) and lattice structures are defined. The former are distinguished into open-foam and closed-foam, while lattice models can be either 2D or 3D.

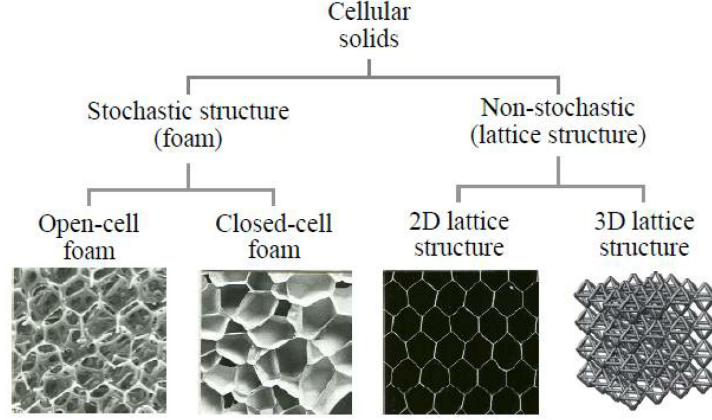


Figure 1.1: Cellular solids classification, [1].

In order to fully understand the very nature of cellular solids, it is relevant to analyze the aspects that influence their basic characteristics such as relative density, cell size and thickness (enclosed within the ‘cell-topology’). Relative density is directly connected to cell topology geometry, therefore mechanical properties of cellular solids can be expressed in terms of these parameters. One of the most important documents about this property is [2], in which Gibson and Ashby idealized the structure of foams (open-cell and closed-cell) in the models shown in Figure 1.2:

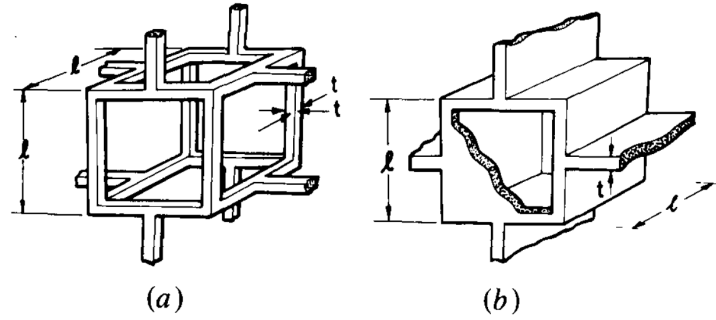


Figure 1.2: The idealization of 3D structure of open and closed cell foams, [2].

The open cell foam is modeled as a cubic array with trusses of size equal to  $l$  and square section of side  $t$ , whereby the relative density  $\rho_R$  is defined as:

$$\rho_R \propto \left(\frac{t}{l}\right)^2 \quad (1.1)$$

A closed-cell foam is modeled similarly and the square struts are replaced by plates of side  $l$  and thickness  $t$ :

$$\rho_R \propto \left(\frac{t}{l}\right) \quad (1.2)$$

As previously mentioned, a further parameter affecting the properties of cellular solids lies in the type of elementary cell selected. Most topologies (hence the configuration of these elementary cells) have been inspired by bio-natural objects such as cytoskeleton of living cells [15] [16], cork, wood, bone and coral [2], generating complex structures with high mechanical and energetic properties, being able to compete with their full-solid counterparts. Indeed, by making a trade-off between performances and weight, they are an excellent option to implement for various applications.

### 1.1.1 Lattice structures

Within the scope of this thesis, the behavior of the macro-category of lattice structures is analyzed through a detailed study of the performance variability (in relation to the implemented topology). However, there is still no unified concept due to the complex composition. Popular definitions of such cellular solids include the work of Gibson and Ashby [2]. Generally, lattice structures are defined as the 3D structures composed of connected unit cells. Tao et al. [1] defined lattice structure as a sort of component formed by spatial periodic unit cells connected through their edges. Concerning their classification, it is of interest to consider three different categories, examined by Dong et al. [17]. The first category is *random lattice structures* or *disordered lattice structures* (shown in Figure 1.3(a)), which includes several topological structures with different diameters distributed in the design space. The second category is *periodic lattice structures*, formed by periodic repeated cells with certain shape, topology, and size (as shown in Figure 1.3(b)). The third kind is *pseudo-periodic lattices*, in which each unit cell has the same topology, but with a different size (Figure 1.3(c)).

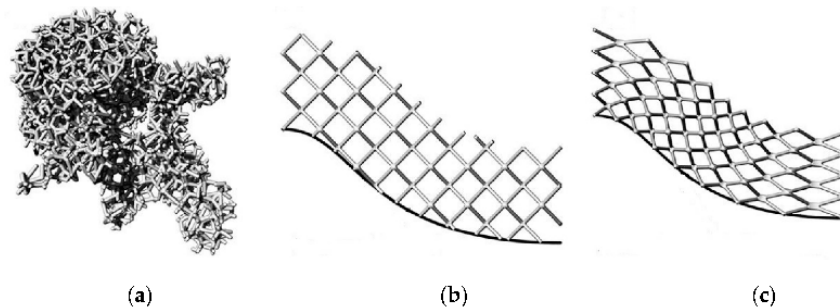


Figure 1.3: Classification of lattice structures: (a) random lattice structures; (b) periodic lattice structures; (c) pseudo periodic lattice structures, [3].

Among the categorizations of interest, struct-based and triply-periodic (TPMS) lattices are

included, in which the smallest unit is called unit cell, defined as the structural part of a lattice, generated by its repetition in a particular format. The fundamental step in constructing lattice structures is the stacking of unit cells in the three directions (x,y,z) [18] because, depending on its configurations, each one has its own characteristics [19]. Therefore, it is of interest to outline the main characteristics of these structures from the different elementary cells, divided mainly into the following categories:

- Body centered cubic (BCC) cell, which is made of 4 struts intersecting at the center of the cube;
- Body centered cubic with reinforced vertical struts (BCCZ) cell, which has the same structure of BCC with the addition of vertical struts in the Z direction;
- Face centered cubic (FCC) cell, made of 8 half-struts that intersect, 2 by 2, at the middle of the lateral face;
- Face centered cubic with reinforced vertical struts (FCCZ) cell, which is the same of FCC with vertical z-struts;
- Face and Body centered cubic (FBCC) cell, which is a combination of FCC and BCC;
- Face and Body centered cubic with reinforced vertical struts (FBCCZ).

The structures of the previously listed cells are shown in Figure 1.4:

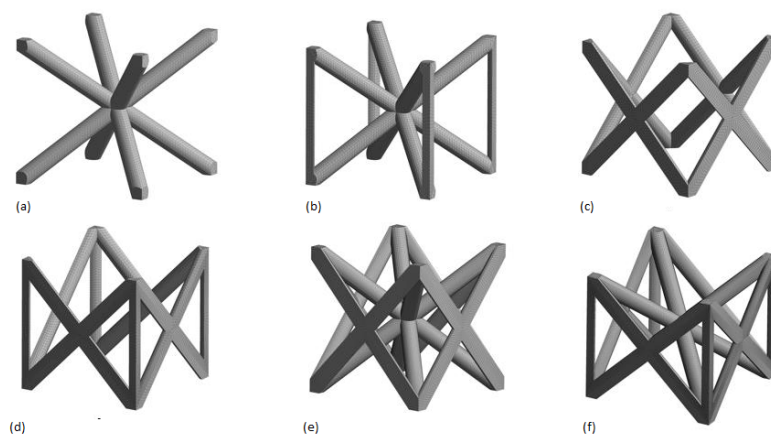


Figure 1.4: (a) BCC, (b) BCCZ, (c) FCC, (d) FCCZ, (e) FBCC, (f) FBCCZ - unit cell topology.

Many other unit cells can be found in literature and are currently under research. Some examples are the auxetic and the octet-truss analyzed by Beharic A. et al [20], vertex cube (VC)

and Edge center cube (ECC) described by Xiao Z. et al [21].

Such topologies are characterised by their Maxwell number,  $M$ , which is dependent on the number of struts ( $s$ ) and nodes ( $n$ ), as extensively discussed in [22]:

$$M = 6 + s - 3n \quad (1.3)$$

The value of this parameter defines an important categorization (shown in the Figure 1.5), investigated in [23], whereby if  $M < 0$ , there are too few struts to equilibrate external forces, causing a bending-dominated behaviour. Different performance occurs when  $M > 0$ , inasmuch as the external loads are equilibrated by axial tension and compression in struts, leading to a stretch-dominated structure [5]. Due to these phenomena, stretch-dominated cells are stiff and strong, while bending-dominated ones are compliant and deform more consistently.

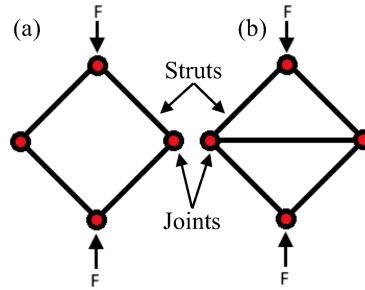


Figure 1.5: Examples of (a) bending-dominated and (b) stretch-dominated structures, [4].

### 1.1.2 Mechanical properties

Thanks to their potential applications, many studies have been conducted to characterize the static and quasi-static mechanical properties, including their experimental characterization. In [24], [25] and [26] can be seen that methods for the characterization of conventional materials are valid for lattices as well. From mechanical characterization, it is clear that lattices tend to keep the same behavior of the general cellular solids, thus three regions of the stress-strain diagram are highlighted:

- linear elastic region;
- plateau region;
- densification region.

These trends are clearly underlined in the Figure 1.6 in which it is possible to appreciate the different behaviour between stretch and bending-dominated lattice structures. During elastic

deformation, the material response is linear elastic, whose slope of the linear section is exactly equal to Young modulus. However, for the most accurate representation of the elastic modulus of metallic cellular structures, Ashby et al. recommend measuring the unloading modulus, as it better represents the structure's performance. Once the elastic limit is reached, for bending-dominated structures, deformation continues with an almost constant stress, referred to the plateau stress, while the trend of the stress-strain curve shows a sort of oscillations in the case of stretch-dominated structures. Once cells deform enough, generating a contact of the struts, the densification strain is reached, with three compressive failure modes:

- sequential cell collapse;
- propagation of cracks through the model;
- diagonal preferential shear planes.

The failure propagation usually originates from a pre-existing defect, and diagonal shear results in an initial loss of strength, which is generally followed by a strengthening during densification. Compressive strength and stiffness are highly dependent on the bending-dominated or the stretch-dominated behaviour, hence it is clear to understand that the latest present greater strength.

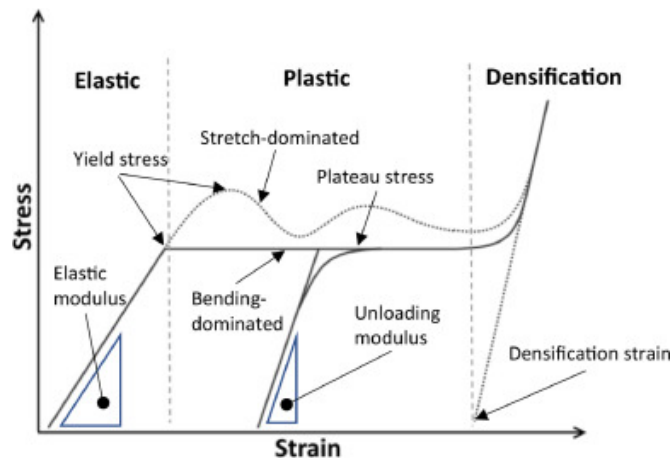


Figure 1.6: General compressive behaviour of stretch and bending-dominated lattice structures, [5].

Although dynamic performance is important for many applications of AM lattice structures, a limited number of studies are presented in the literature to define the dynamic behavior of metallic cellular structures. Harris et al. [27] investigated the dynamic compressive performance of lattice structures manufactured by selective laser melting (SLM) and Tobias M. et

al. [12] focused their attention on the mechanical response of five different topologies (BCC, BCCZ, FCC, FCCZ, and FBCCZ). In this work, the samples were tested under quasi-static and dynamic loads, comparing the results with the numerical models to identify topological and dynamic effects of the SLM process and the main properties of the samples. Thanks to these analysis, general results have been extrapolated, which will be confirmed in the following chapters. The inclusion of z-struts in BCC, FCC and FBCC specimens led to an increase in strength and stiffness and the FCCZ topology was found to be the most efficient topology, in terms of specific strength and energy absorption (SEA), thanks to the more homogeneous distribution of stresses across the structure. Both static and dynamic analysis revealed that specimens failed by the emergence of diagonal shear planes, the orientation of which was dependent on topology, as demonstrated by the numerical models, showing a concentration of the stress in struts connecting diagonally in the opposite corners of the structure.

Further studies were conducted to analyze the increase of the energy absorption (EA), due to the adoption of multi-morphology lattice structures. Among these, José Souza et al. [28] focused on a closed-form analytical methods based on beam theories to calculate the effective properties. The increasing of the energy absorption, introducing different lattice cells topologies, is fully analyzed in [10], where it is pointed out that the FBCCZ topology provided the highest value of EA. Once again, both static and dynamic analyses identified the FCCZ as the most efficient topology for EA (due to the high densification strain). Other analyses are presented by Ryan Alberdi et al. [29], which demonstrated that combining different unit cell architectures it is possible to improve energy absorption. The topologies considered in this work combined stretch-dominated FCC and bending-dominated BCC unit cell, highlighting that the primary collapse mode could be controlled through multi-morphology lattices.

### 1.1.3 Manufacturing techniques

Nowadays, there are many implemented technologies for the realization of lattice structures, from traditional methods, such as water-jet cutting and braising, to advanced manufacturing processes. Traditional manufacturing techniques are useful for creating lattice structures, demonstrating highly accurate of the final model, but taking into account the reticular nature of such structures, these conventional processes are characterized by considerable complexity. The basis of most additive manufacturing processes involves the deposition of material in a 2D layer and applying a successive layer on the top, for which they are more adaptable in



comparison to traditional methods, placing material only where it is required. The two main additive manufacturing processes utilized in the creation of lattice structures are powder bed fusion technologies such as SLS and SLM [6], as can be seen in Figure 1.7. The main advantage of the selective laser melting (SLM) method is in producing metallic fully dense parts. SLM parts will be produced and tested (Chapter 6) in this work to validate the mechanical behavior predicted by the computer modeling performed using finite element analysis (FEA). Another additive manufacturing method very commonly utilized is electron beam melting technology (EBM), which, instead of utilizing laser, utilizes an electron beam as a heat source to fully melt each layer.

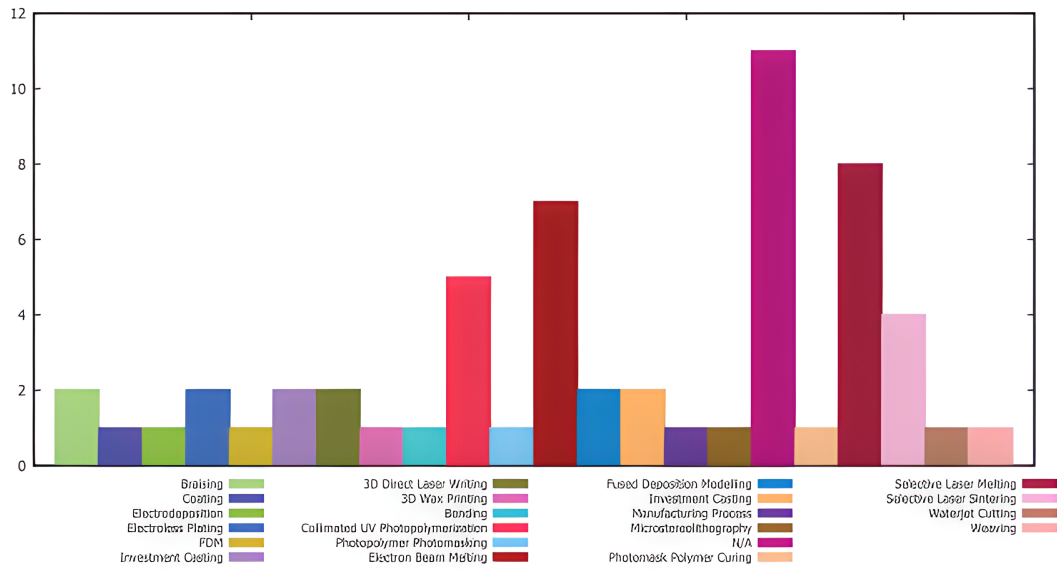


Figure 1.7: Manufacturing methods for lattice structures, [6].

It is also possible to carry out an evaluation of the manufacturability of lattice structures, as shown by Yan et al. [30]. They found that structures with 2–8 mm unit cells could be manufactured without the need of supports. Leary et al. [31] sought to define the manufacturability of particular struct-based topologies and characterize the mechanical performance of lattice structures fabricated in AlSi12Mg, using SLM. Lower limits of manufacturability (in terms of strut diameter and inclination angle) are identified, and the general behavior of different unit cell topologies are characterized.

### 1.1.4 Applications

The practical applications are increasingly used thanks to the properties of the lattice structures, which are influenced by the geometry (size and shape of the structure and its structural elements) and topology. Many studies have been conducted on AM lattice structures, and it has been found that, by tuning lattice geometry and topology, the lattice structures can be manufactured to achieve a broad range of properties [32] that cannot be achieved by their parent bulk material [33], including thermal [34], acoustic [35], and mechanical properties [36].

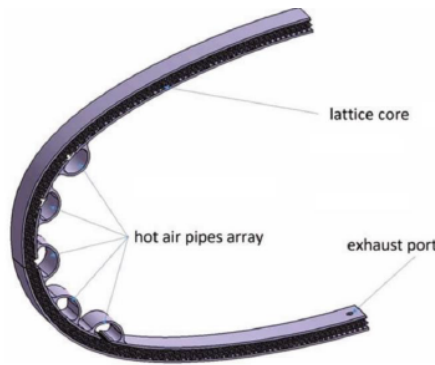


Figure 1.8: Anti-icing system of an aircraft wing, [7].

In the aerospace field, applications of interest include parts realised to generate protections, environmental separations, aerodynamic profiles, embedded hydraulic lines and irregularly shaped pressure vessels. A recent implementation, for the aerospace structures, can be found in [7], where lattices have been studied and characterized in order to use them for the design of an anti-icing system (shown in the Figure 1.8) for the leading edge of an aircraft wing, where the impact energy absorption and heat regulation capacities are both exploited, while Bici et al. [37] investigated a novel wing leading edge that serves both as an impact absorber and as an anti-ice system. Miller et al. [38] patented a new system to protect a flight recorder and Büşra et al. [39], after topology optimizing a suspension arm, infilled it with lattice obtaining both strength improvement and weight reduction. An example for the automotive field is well described in [40], where a rollover component, for F1 vehicles, has been developed employing a hybrid design. On the other hand, in the biomedical field, the lattice structures are of particular interest for the production of bone scaffolds [41], [42]. These materials are also preferred for orthopedic implants to replace a missing joint or to support a damaged bone. Therefore, lattices can substitute the human bones because the internal pores are able to accommodate and guide

the proliferation of living cells. An example, reported in [8], shows this type of applications, in which a bio-medical prototype, produced by EBM, is introduced into the implant design. The Figure 1.9 shows how the 3D printed sternum and rib cage fit inside the patient's body:

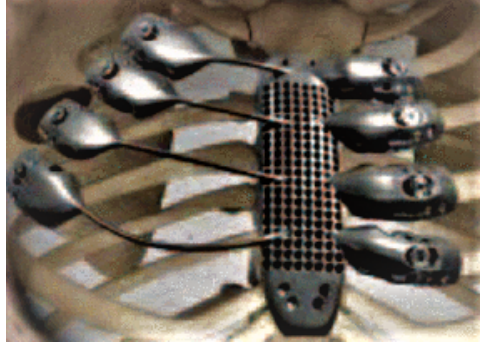


Figure 1.9: Medical implant using lattice structure, [8].

Another relevant application is the use of such structures as heat exchangers (Figure 1.10 widely investigated in [9]. The heat transfer characteristics make it well-suited for high-performance heat exchanging devices as well as more complex devices.

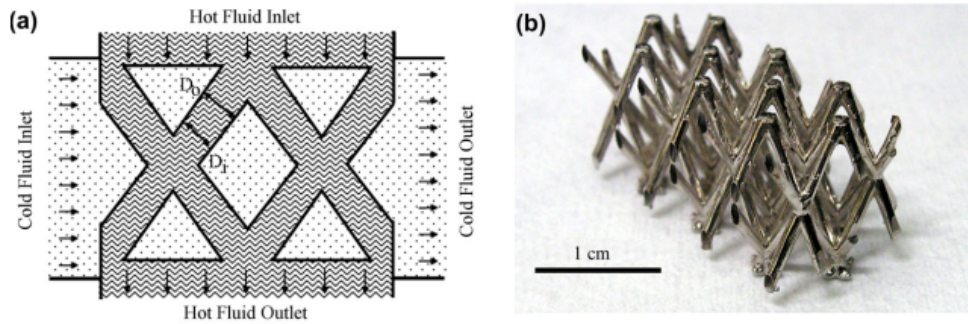


Figure 1.10: Micro-heat exchanger (a) schematic of operation, (b) image of electroplated micro-lattice with solder at node, [9].

## 1.2 Main purposes

Additively manufactured lattices offer a unique solution to lightweight components, adding multi-functionality. The advantages they provide are considerable, ensuring high efficiency also from the point of view of energy absorption. These properties vary greatly based on the internal design of the individual cell units and their position in space.

Based on these considerations, several methodologies have been developed to enhance the

energy properties, based on optimal reconfigurations of the geometries. Design methods are emerging and include a family of topology optimization to tailor local cell density. Since the work of Bendsoe and Kikuchi [43], topology optimization has developed into different branches including Solid Isotropic Material with Penalization (SIMP) [44] and level-set based methods [45], including optimal designs and improved properties. Guo et al. [46] proposed a stress-based topology optimization in the level set-based approach to treat local stress constraints, while Zhang et al. [47] developed a methodology to handle the stress.

The primary aim of this thesis is to conduct an in-depth study of different lattice specimens and, on the basis of a stress field analyses, to implement a Matlab code for the homogenization of the stress distribution, ensuring an increase in energy properties. The energy absorption is closely related to the mechanical behavior, so it is decided to reconfigure the internal stress field, firstly by calculating the internal values using the Ansys software, which imported can be modified as the internal diameters of each specimen strut change. The Matlab code allows local variation of density, following two different approaches, one of which is based on existing workflows proposed in [48]. Post-optimization, the same code enables to recalculate the energy properties, in the form of a 3D database, providing a clear visualization of the internal stress field and the new thicknesses chosen for the struts. In this work, it is reported stress-based optimization, analysis (through Ansys and a Matlab automatic code) and mechanical test validation of the different graded samples. The static compression tests are performed to demonstrate and confirm the results obtained from the finite element models. The findings validate the optimization approach for the particular use and load case and start to build confidence in the approach as an accepted method.

# Chapter 2

## General models

The fundamental step in constructing lattice structures is the stacking of unit cells in x, y, and z directions [49], because, depending on its configurations, they show different characteristics [50]. The cells typologies, analyzed in this chapters, are the six configurations (BCC, BCCZ, FCC, FCCZ, FBCC and FBCCZ), set out in the introduction. They are chosen both to make a close comparison with the results previously obtained in [10] and [11], but at the same time because they are the topologies representative of the macro-behaviour of lattice structures. On the basis of these configurations, primary analyses are carried out to define the parameters necessary for the implementation of more complex models and the optimization processes, set out in the following sections.

### 2.1 Material

The choice of the material, implemented for the specimens, is made on the basis of the production process that will be used for the realization, in order to carry out a further experimental analysis to validate the numerical results. Within the ambit of additive manufacturing technologies, there are different materials of a metallic nature to produce components. The main alloys currently in use, considering production processes like SLM, include:

- Aluminum alloys;
- Titanium alloys;
- Nickel-based alloys;
- Cobalt-Chromium alloys;

The final choice has fallen upon AlSi10Mg because this alloy is one of the most used among other aluminum alloys in the field of light-weight structures, as analyzed in [51]. Other aluminum alloys are employed for lattices as well, such as Al7075 and Al12Si, but AlSi10Mg has been selected because it is the most used material at Konstruktiver Leichtbau und Bauweisen (KLuB, TU Darmstadt), where the final specimens were printed to perform the experimental tests. The density, the modulus and the Poisson Ratio (and  $G$  as a result) used for the linear model are assumed on the basis of experimental discussions present in [52] and correspond to:

- $\rho = 2.68 \frac{g}{cm^3}$ ;
- $E = 75 GPa$ ;
- $\nu = 0.33$ ;
- $G = 28.195 GPa$ .

While for the bilinear model the following values will be used:

- $\sigma_Y = 250 MPa$ ;
- $\epsilon_Y = 0.00333$ ;
- $E_T = 2250 MPa$ .

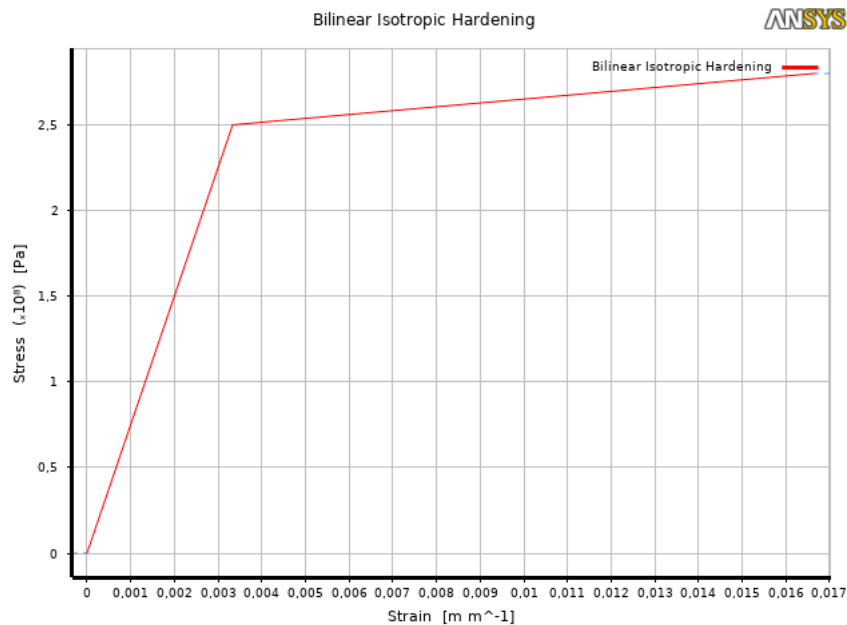
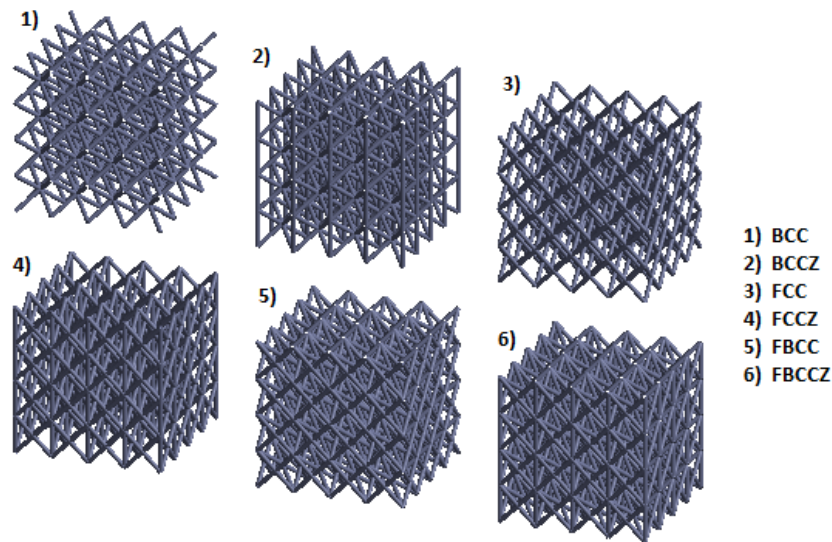


Figure 2.1: Material bilinear behaviour.

## 2.2 Selection of specimen configurations

Before performing the analysis of interest within the Ansys environment, it becomes necessary to set optimal parameters to achieve accurate results. This involves carrying out a sensitivity analysis on representative models, therefore low-dimensional specimens are modeled to conduct this study. The tests are carried out for specimens with four unit cells on each side (in the x,y,z directions), for the six configurations. The static bilinear tests performed refer to models created using beam elements, this allowed to reduce the computational costs of the analysis, reducing calculation times, but at the same time allowing to test and validate the specimens in terms of global behavior and not in reference to the single RVE. For each of the six specimens, shown in the Figure [2.2](#), AlSi10Mg was applied as material, with the same constraint and load conditions:

- a general displacement imposed along z and applied to the nodes belonging to the upper face;
- 'fixed' type constraint, which has been applied to all the nodes belonging to the lower face.



*Figure 2.2: Samples with four unit cells for each side.*

## 2.3 Mesh-sensitivity analysis

Before proceeding with the bilinear static analysis, it is of primary importance to determine the appropriate 'size element' and perform the mesh, in order to minimize the computational



costs of the analyzes and at the same time to have good accuracy on the results. The sensitivity analysis, treated in this paragraph, concerns a 4x4x4 specimen of FBCC-Z unit cells. The choice to carry out the sensitivity analysis on this type of specimen was determined by the fact that the latter is the one consisting of the largest number of struts, in order to highlight any problems related to both software limitations and accuracy.

### 2.3.1 Analysis settings

The chosen specimen is represented in Figure 2.3, whose dimensions are equal to 12 mm for each spatial dimension. The constraint and load conditions are a 'fixed supported' constraint on the lower base and a displacement imposed on the upper surface equal to -1 mm in the z-direction.

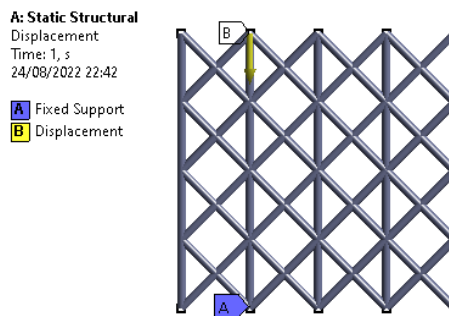


Figure 2.3: General BCs and imposed displacement for 4x4x4 (cells) samples.

The convergence study, as the mesh size changed, was carried out on two different outputs:

- Force Reaction [N];
- Deformation Probe [mm].

The choice of the two different outputs to monitor is necessary to confirm the final and global convergence, whose asymptotic value is not local. In order to make the results of the sensitivity analysis reliable, the geometric node (exactly in the middle) is chosen as the point for the deformation probe. This point is a geometric entity and not a node belonging to the mesh to make the latter stable as the size element varies.

### 2.3.2 Results

Once the model is implemented within Ansys Workbench and the boundary conditions and displacements are set, a static bilinear analysis is carried out, assuming AlSi10Mg as the ma-



terial. The values obtained are collected in Table 2.1 and divided into defined intervals, which represent the ranges of values examined. The Figures 2.4 graphically display the trends of the two outputs and outline the value of the element size for which convergence is reached.

Element size [mm]	Nodes [N]	Elements [N]	Force reaction - Z direction [N]	Deformation probe [mm]
[2.598 - 2.1]	2852	1864	2325	0.11082
[2 - 1.5]	4105	2344	2342.1	9.8795E-2
[1.4 - 1.2]	4505	2504	2342.1	9.8795E-2
[1.1 - 0.7]	6809	3856	2342.1	9.8729E-2
[0.6 - 0.5]	10537	5720	2342.2	9.8719E-2
[0.49 - 0.4]	15545	8224	2342.2	9.8621E-2
[0.39 - 0.3]	29689	15296	2342.2	9.8555E-2
[0.29 - 0.01]	149977	75440	2342.2	9.8555E-2

Table 2.1: Results of the sensitivity analysis.

Graphically, it is possible to appreciate the convergence of the results through the following images:

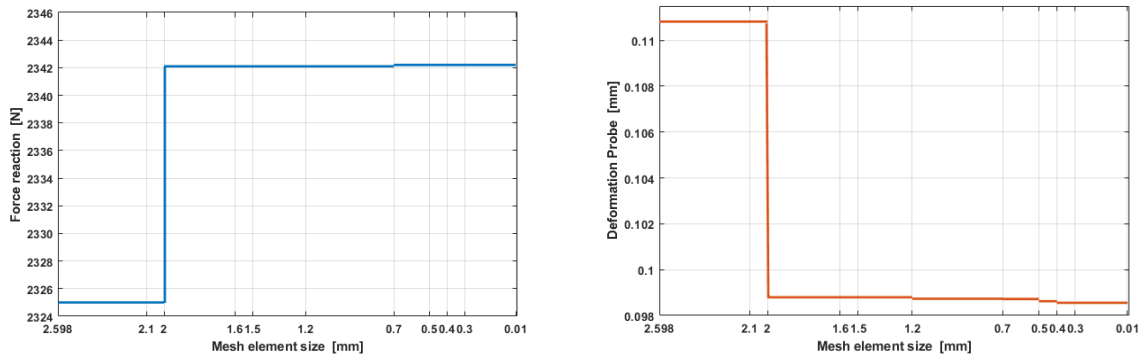


Figure 2.4: Trends of Force Reaction and Deformation Probe output, considering different element sizes (range values).

Having minimum deviations in terms of constraint reactions and deformations, it is possible to assume as perfect element size a value included into the range [2 - 1.5]. In order to increase accuracy, the minimum of the proposed band was chosen, so a value of exactly 1.5 mm, which will be selected for all future analyses, proposed in the following Chapters. This assumption allows to minimize the calculation times, reducing the computational costs to an absolute minimum, but at the same time allowing sufficiently accurate results.

## 2.4 Bilinear static simulation of the 1D beam model

Once the sensitivity analysis has been completed, specimens have been tested assuming a 1D beam model, which provides a faster analysis, but at the same time needs to be compared with the 3D model, presented in the literature. BCC, BCCZ, FCC, FCCZ, FBCC, and FBCCZ cells are all modelled through ANSYS' Design Modeler using cylindrical struts with diameter of 0.37 and length of 3 mm. The Static Structural module is selected to perform the static bilinear simulations and the material AlSi10Mg is assigned to the structure. The results of the simulation are related to the meshing element size established through sensitivity analysis. Maintaining the constraint and load conditions described in the previous section, the static bilinear simulations are carried out for each of the six specimens. Having known the geometric dimensions and the step-by-step values of the force reactions, the two vectors of 'stress' and 'strain' are calculated as:

$$\sigma_i = \frac{F_{Ri}}{A} = [MPa] \quad (2.1)$$

$$\epsilon_i = \frac{F_{Ri}}{L} = [-] \quad (2.2)$$

where A represents the area of the sample, equal to  $144 \text{ mm}^2$  and L the length which corresponds to a value of  $12 \text{ mm}$ .

### 2.4.1 Results

In the Figure [2.5](#) it is possible to evaluate the stress-strain curves, plotted in the same graph:

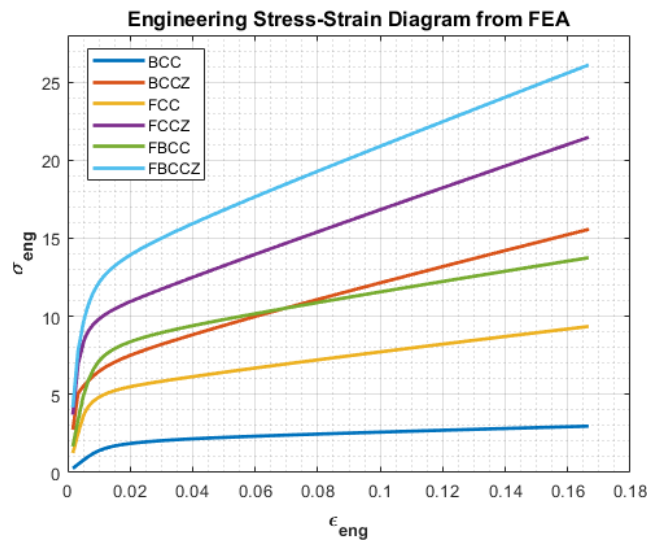


Figure 2.5: Comparison of the sigma-stress curves of the 4x4x4 cell samples.

The results obtained in terms of energy absorption EA, specific energy absorption SEA and volumetric energy absorption VEA are shown in the Table 2.2 and are enclosed graphically in the histograms 2.6 and 2.7. The values are based on the specimen density  $\rho$  and obtained through the integral of stress  $\sigma$  and strain  $\epsilon$ , measured between 0 and the failure  $\epsilon_F$ :

$$SEA = \frac{1}{\rho} \int_0^{\epsilon_f} \sigma d\epsilon = \frac{EA}{m} = \left[ \frac{mJ}{g} \right] \quad (2.3)$$

$$VEA = \int_0^{\epsilon_f} \sigma d\epsilon = \frac{EA}{V} = \left[ \frac{mJ}{mm^3} \right] \quad (2.4)$$

Cell	Force reaction - Z direction [N]	Displacement [mm]	EA [mJ]	SEA [mJ/g]	VEA [mJ/mm <sup>3</sup> ]
BCC	427.421	2	854.844	2230.210	0.495
BCCZ	2242.772	2	4485.409	9549.490	2.596
FCC	1346.609	2	2693.242	6884.462	1.558
FCCZ	3091	2	6182	12943.891	3.577
FBCC	1980.358	2	3816.611	4927.821	2.209
FBCCZ	3758.152	2	7516.245	8730.632	4.349

Table 2.2: Results from bilinear static analyses on the 4x4x4 samples.

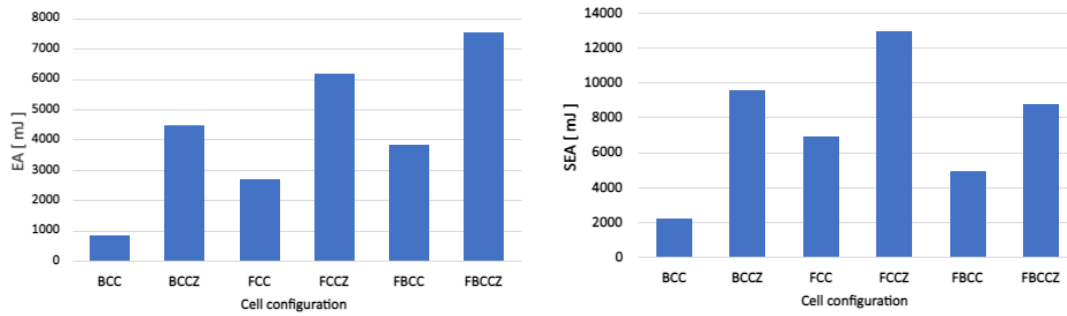


Figure 2.6: EA and SEA of the 4x4x4 (cells for each dimension) samples.

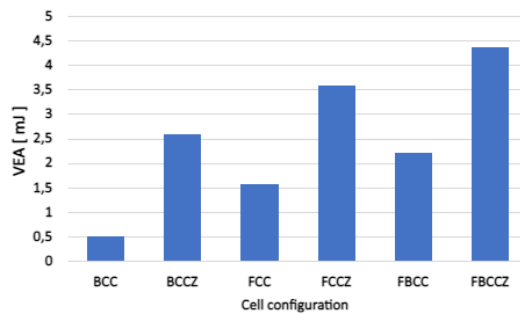


Figure 2.7: VEA of the 4x4x4 (cells for each dimension) samples.

In terms of EA and VEA, the optimal values is achieved by the 4x4x4 specimen composed of FBCCZ cells, while in terms of SEA, the best energy behavior is shown by the specimen composed of FCCZ cells, while the BCC configuration has the lowest values for the three required outputs.

## 2.5 Validation of the 1D beam models

The introduction of a 1D beam model permits to reduce the computational costs of analysis. This is advantageous testing larger and more complex samples. However, this assumption introduces a lower accuracy, so that it is necessary to validate the models obtained by comparing them with those obtained in the case of modelling with 3D elements. In the discussion, two different confrontations will be made in order to validate the models:

- the first one compares the six configurations (BCC, BCCZ, FCC, FCCZ, FBCC, FBCCZ) considering a single RVE with the results obtained in [10], under the same constraint and load conditions;
- the second one compares the six configurations (BCC, BCCZ, FCC, FCCZ, FBCC, FBCCZ) considering a single RVE with the results obtained in [11], under the same constraint and loading conditions.

The two qualitative confrontations are made between 1D and 3D models, on the elementary cells (RVE), while for the third case, two 1D beam models are compared. However, this is done in order to macroscopically compare the analysis results with those reported in the literature [12].

### 2.5.1 First comparison

In this sub-section, a validation is made through the correlation of the trends obtained for the 1D and the 3D model ([10]). For each single configuration, the results are related to a single RVE 3X3X3 mm, as it is not computationally affordable to carry out bilinear analyses with 3D elements on an entire specimen 30x30x30 mm. BCC, BCCZ, FCC, FCCZ, FBCC, and FBCCZ cells are all modelled through ANSYS Design Modeler using cylindrical struts with a diameter of 0.37 mm and a length of 3 mm, as shown in the Figure 2.8:

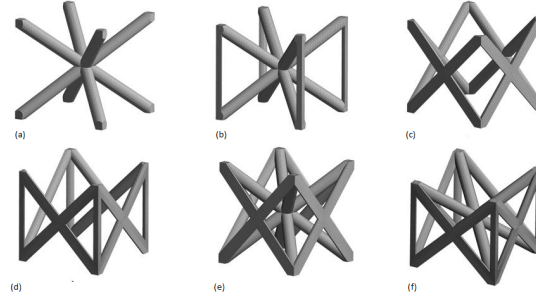


Figure 2.8: (a) BCC, (b) BCCZ, (c) FCC, (d) FCCZ, (e) FBCC, (f) FBCCZ, single RVEs chosen for the confrontations.

The Static Structural module is selected to perform the static bilinear simulations and the material (AlSi10mg) is assigned to the structure. A displacement of -0.02 mm is imposed on the upper surface (with normal +Z) of each cells and a fixed support on the opposite side (on the surfaces with normal -Z) for the both models. From the static bilinear analysis it is possible to obtain in output the force reaction and the directional deformation, from which the stress-strain curves are extracted for each models. The main outputs to be compared, as they will be the focus of this thesis, are the specific and volumetric energy absorption, shown in the Figures 2.9 and 2.10:

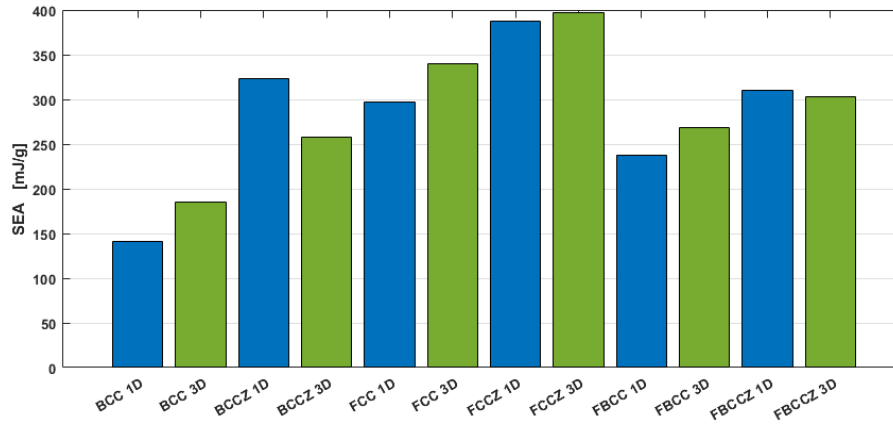


Figure 2.9: Overlaid comparison for SEA for the 1D beam and 3D models ([10]).

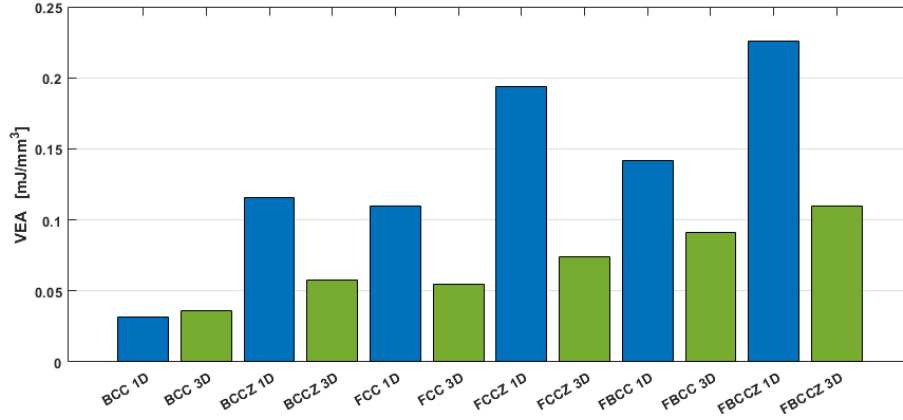


Figure 2.10: Overlaid comparison for VEA for the 1D beam and 3D models ([10]).

In the histograms, the blue columns refer to the 1D model, while the green columns refer to the 3D model. In the 3D models, the main difference is due to the fact that the FBCC surpasses the FCCZ in term of EA and VEA. This shows the higher energy absorption capacity of the FBCC plastic field. A consideration can be done also in the sense of struts orientation: FBCC presents oriented struts instead of vertical ones, as in FCCZ, and their presence influences in a good way force reaction and EA (whose trend is the same as that of VEA) for both the 1D e 3D models.

Moving to SEA, FCCZ cell seems to be the most convenient choice when a compromise between energy absorption and weight has to be done for both the models. Generally, there are deviations in the trends, but the best configurations remain the same (FCCZ for SEA and FBCCZ for VEA). The differences are largely explained by design choices made when, in the 3D case, the end of each struts was constructed considering a slicing process to refine the inter-connection zones. This was not done in the 1D discretization, where a circular cross-section of 0.37 mm diameter was simply assigned. This implies a different mass contribution and results that differ for configurations with a high number of constituent struts.

Differences regarding the VEA values can be seen only as regards the FBCC configuration, which is more suitable than FCC-Z, for the 3D-models. This difference highlights the fact that the 1D models are less accurate than the 3D model, but since the deviations are minimal values, it is considered acceptable to take the 1D approach with beam elements in order to reduce computational costs and times.

## 2.5.2 Second comparison

In this section a comparison is made with the results obtained in [11], analyzing again the behavior of the six single RVEs and assuming the same bilinear material (AlSi10Mg), BCs and load. BCC, BCCZ, FCC, FCCZ, FBCC, and FBCCZ cells are all modelled through ANSYS Design Modeler using cylindrical struts with a diameter of 0.37 mm and a length of 3 mm, introducing 1D beam and 3D elements for structural discretizations. A displacement of -1 mm on the upper surface and a fixed support on the base are imposed for both the models. In this case, from the static bilinear analysis it is possible to compare in output the stress-strain curves for the two cases:

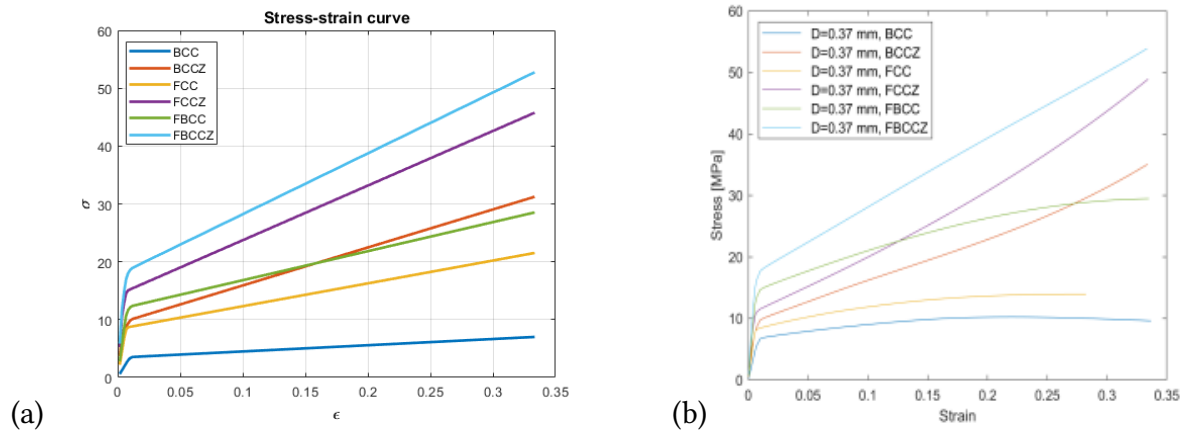


Figure 2.11: Stress strain curves for (a) the 1D and (b) 3D models, [11].

From the plots it is evident how the addition of vertical struts in the Z direction improves the resistance of the structure under load parallel to Z both for 1D approach and for 3D one. In order to estimate the deviations between the two models, the trends for SEA, explanatory of the global behavior, is outlined:

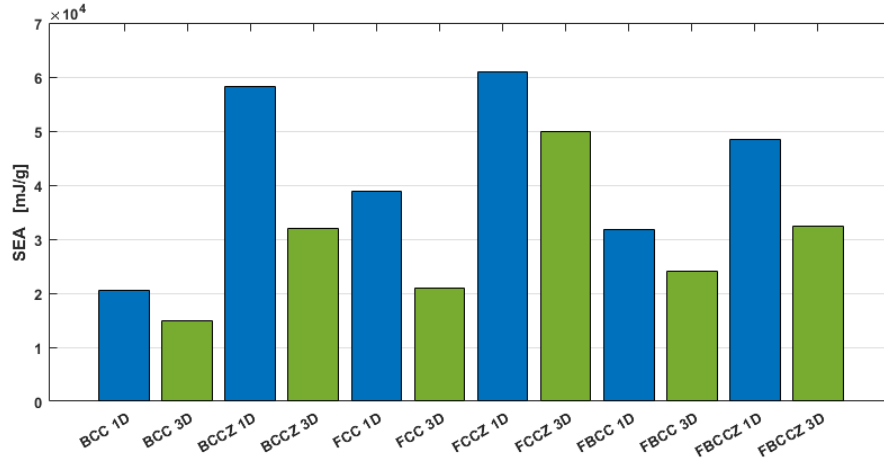


Figure 2.12: Overlaid comparison for SEA for the 1D beam and 3D models, [11].

The Figure 2.12 shows the same trend for SEA, with deviations only in values, but not in trends, as the 1D modeling introduces different masses. The SEA's plots show that FCCZ has consistently the highest value because the addition of Z struts does not increase the density substantially while it greatly influences the structure's behavior under load.

These results generate a strong correlation between the 1D beam model and the 3D one, therefore specimens with the former approach will be modelled in the remainder of the thesis. At the same time, this ensures reliability of the results, but great savings in terms of cost and computational time, leaving scope for more in-depth and diversified investigations.



# Chapter 3

## Bilinear static simulations

### 3.1 General configurations

The overall behavior that the lattice structures show, downstream of a statically applied load, is well described by specimens whose dimensions are sufficiently large. This consideration is reflected in experimental and numerical tests present in [53], [28], [29] since, assuming considerable dimensions, it is ensured that the edge effects do not affect the validity of the analysis outputs. Based on this consideration, three types of specimens will be tested within this chapter, having an increasing number of layers along z-direction (10,15,20). This is of interest as the outputs will be compared not only in terms of mechanical and energetic properties, but also in terms of failure modes and stress fields. This lays the foundation for choosing the best geometric configuration to be carried forward the structural optimization, trying to find a trade-off between accuracy of results and acceptable computational cost and time.

Certain key assumptions were made in this chapter. Struts are modeled as beam elements, which have no physical volume. Within this chapter it is decided to consider the six different configurations of individual RVEs, described in the previous chapter (BCC, BCCZ, FCC, FCCZ, FBCC and FBCCZ). This choice, also adopted in the recently published works [12], becomes necessary to validate the results analyzed in [10]. Since the FEM software employed is Ansys Workbench, Design Modeler is the tool used for geometries. Every cell considered in this investigation presents more than three symmetry planes, and that makes the geometry generation process way easier. Thanks to this property it is possible to make the specimens, for each of the six configurations, by translating and mirroring elementary units through suitable

symmetry planes. The specimens, described within the next three paragraphs, show the same peculiarities, but with different dimensions along the z-axis, so the number of cells along this direction will be 10 (30 mm), 15 (45 mm) and 20 (60 mm). Therefore, AlSi10Mg is chosen as the material, as the aim of the discussion will be their realization using AM techniques and the subsequent experimental tests.

## 3.2 Samples with (10,10,10) cells along (x,y,z)

Each of the specimens is composed of elementary cells of size 3x3x3 mm and has 10 cells for each spatial dimension (length, width and height). Based on these assumptions, the total dimensions for each are 30x30x30 mm, as shown in the Figure 3.1.

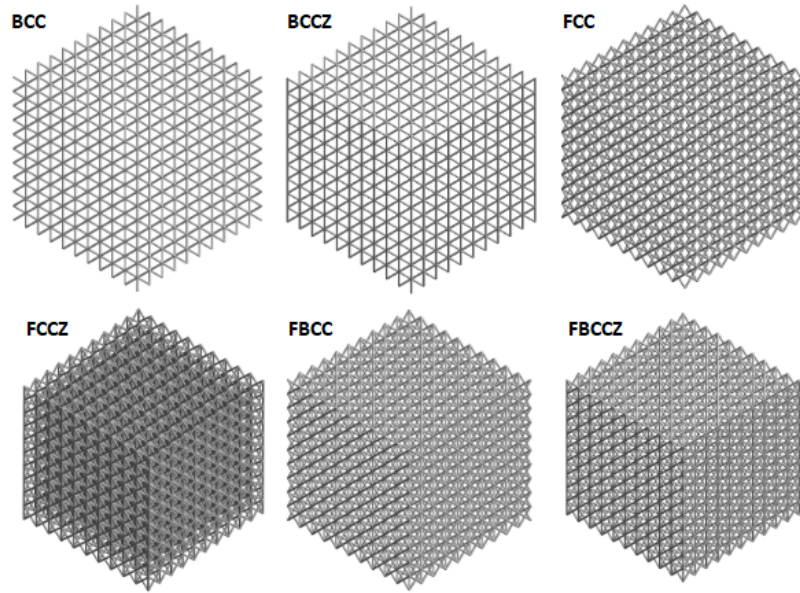


Figure 3.1: Sample configurations 30x30x30 mm.

### 3.2.1 Finite element modelling

To investigate collapse behaviour and deformation mechanisms, a finite element (FE) model was developed to replicate the behaviour of the candidate lattice structures (Fig. 3.1), using the Ansys static solvers. The mesh size was set by means of a minimum 'element size' equal to 1.5 mm, based on the sensitivity analysis. Lattice struts is represented using 2-node linear beam elements, with circular cross-sections that matched the experimental specimen's topological and geometric parameters (0.37 mm diameter, 3 mm cell size, 10 cells in x, y, and z

directions). However, there are known limitations of modelling lattice structures using beam elements, such as the inability to directly model geometric defects (resulted from AM fabrication methods) and the absence of the 'Von-Mises Stress' output (in the Ansys environment). To overcome this problem, the value is extrapolated using appropriate manual commands in the software setting.

### 3.2.2 Boundary conditions and loads

For simplicity and homogeneity of treatment, it is decided to impose, for each of the six specimens, the same constraints and load conditions. A 'fixed' constraint for the bottom surface has been inserted as boundary conditions, so that all spatial translations and rotations of the base are blocked. An 'imposed displacement' of -2 mm along the z direction has been applied to the upper surface (Figure 3.2).

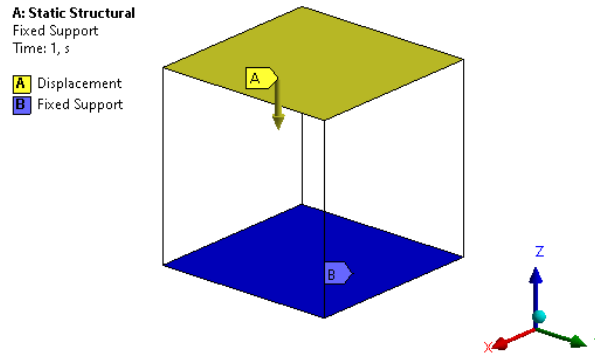


Figure 3.2: BCs and load for the selected samples.

### 3.2.3 Results

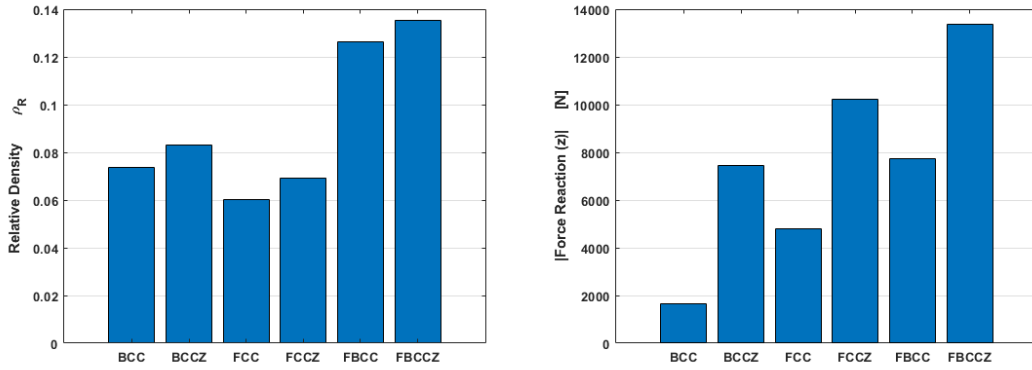
In order to make the results as valid as possible, the 'large deflection' option is set as input for the analysis. It is also chosen to insert a precise number of analysis substeps, to evaluate the outputs in equally spaced intervals, small enough to consider the accuracy acceptable. The main output requested to Ansys is force reaction  $F_z$ , that is the one registered on displaced surfaced. Using  $F_z$  it is possible to calculate specific energy absorption SEA and volumetric energy absorption VEA (that presents the same trend as EA, being the RVE volume the same for every cell and for the whole sample). Using force and RVE section area ( $900 \text{ mm}^2$ ), as well as displacement and RVE edge length, it is possible to evaluate physical and mechanical properties, as shown in the Tables 3.1 and 3.2 below:

	$V_0$ [mm <sup>3</sup> ]	$V$ [mm <sup>3</sup> ]	$\rho_R$	Mass [g]
<b>BCC</b>	27000	1987	7.3590E-2	5.9889
<b>BCC-Z</b>	27000	2246	8.3180E-2	7.0349
<b>FCC</b>	27000	1627	6.0260E-2	5.3789
<b>FCC-Z</b>	27000	1872	6.9330E-2	6.4249
<b>FBCC</b>	27000	3414	12.6440E-2	11.368
<b>FBCC-Z</b>	27000	3658	13.55000E-2	12.414

*Table 3.1: Physical properties from bilinear static analyses.*

In the table, the mass is calculated with the aid of the software,  $V_0$  indicates the volume of the total sample 30x30x30 mm, considering it as a homogeneous cube, while  $V$  is the value of the effective volume, considering the the gaps between the struts. Through the values of  $V_0$  and  $V$  it is possible to evaluate the relative density as:

$$\rho_R = \frac{V}{V_0} \quad (3.1)$$



*Figure 3.3: Relative Density and Force reaction along z-axis of the samples*

The relative density shows how the contributions, in terms of mass, are greater for specimens composed of cells in which the z-struts are present, while the specimen with FCC cells, turns out to be the most convenient alternative in terms of mass reduction.

	BCC	BCCZ	FCC	FCCZ	FBCC	FBCCZ
Engineering strain - $\mu\epsilon$	66666.667	66666.667	66666.667	66666.667	66666.667	66666.667
Force Reaction Z [N]	1635.6	7447.4	4795.9	10224	7740.8	13351
Engineering stress [MPa]	1.1817	8.2749	5.3288	11.3600	8.6009	14.8344
EA [mJ]	3271	14895	9592	20448	15482	26702
SEA [mJ/g]	546.2	2117.3	1783.2	3182.6	1361.9	2151.0
VEA [mJ/mm <sup>3</sup> ]	0.1212	0.5517	0.3553	0.7573	0.5734	0.9890

Table 3.2: General results from bilinear static analyses for the 30x30x30 mm samples.

Stress–strain curves, for the tested specimens, are presented in the Figure 3.4 and the values, for each single load sub-step are calculated having known the geometric dimensions and the step-by-step values of the force reactions:

$$\sigma_i = \frac{F_{Ri}}{A} = [MPa] \quad (3.2)$$

$$\epsilon_i = \frac{F_{Ri}}{L} = [-] \quad (3.3)$$

where A represents the area of the sample, equal to 900 mm<sup>2</sup> and L the length which corresponds to a value of 30 mm.

Specimens with z-strut topologies (BCCZ, FCCZ and FBCCZ) showed greater stiffness and strength than those without, with stress–strain curves that suggest a stretch-dominated response. The FBCC-Z sample has the greatest yield and ultimate strengths, but, because of the greater material presence provided by the struts, when mass is accounted for, FCC-Z is the most efficient topology in terms of strength-to-weight ratio. Taking into account that the BCC and BCC-Z specimens has greater relative density than the FCC and FCC-Z ones (as shown in Table 3.1), the superior specific strength of the FCC and FCC-Z specimens demonstrates that relative density is not the only contributing factor to mechanical performance, and that topology significantly affects qualitative and quantitative performance. All these considerations are well represented by the mechanical behavior revealed by the stress-strain curves, shown in the Figure 3.4. The highest curve is related to FBCC-Z configuration, whereby high values for the volumetric energy of absorption are expected.

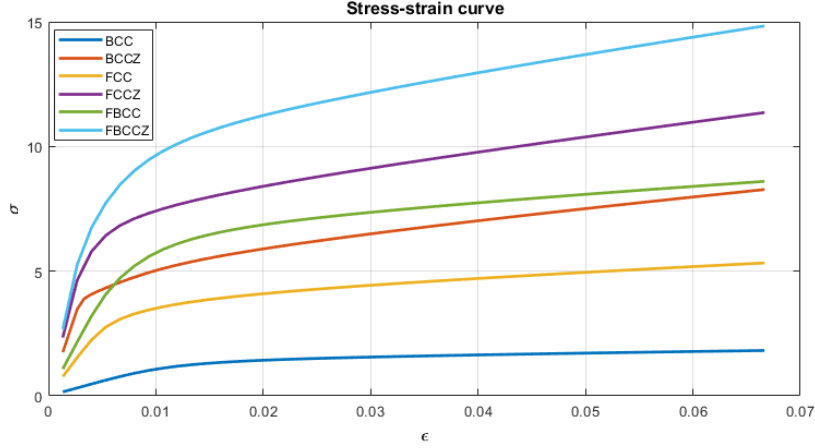


Figure 3.4: Stress-strain curves for the six samples of dimension 30x30x30 mm.

Through the table values, the calculation of the absorbed energy (measured in [mJ]) is immediate. Note the force reaction obtained in the output and the imposed displacement of 2 mm (considered as an absolute value), the results, represented in the histogram [3.5](#), are obtained. The energy absorption during testing per unit volume VEA and per unit mass SEA, based on the specimen density  $\rho$ , are calculated using [3.4](#) and [3.5](#) respectively. Calculations are based on stress  $\sigma$  and strain  $\epsilon$  behaviour, measured between the start of the test and strain at failure  $\epsilon_F$ .

$$SEA = \frac{1}{\rho} \int_0^{\epsilon_f} \sigma d\epsilon = \frac{EA}{m} = \left[ \frac{mJ}{g} \right] \quad (3.4)$$

$$VEA = \int_0^{\epsilon_f} \sigma d\epsilon = \frac{EA}{V} = \left[ \frac{mJ}{mm^3} \right] \quad (3.5)$$

The trend for EA and Force Reaction are very similar, FBCC-Z and FCC-Z present the best values for EA, which are much higher than the corresponding specimens composed of the same cells, but without z-struts (FBCC and FCC). The trend for VEA it is exactly the same recorded for EA, in which the same configurations are preferred for the specimens. In term of SEA values, the trend shows the differences between reinforced and non-reinforced cells. FCC-Z seems again to be the most convenient choice when a compromise between energy absorption and weight has to be done. In general, considering pure EA, VEA and force reaction, the best candidate is FBCC-Z, while comparing the results to the densities that the specimens have, it can be seen that the most convenient choice are the samples with FCC-Z cells.

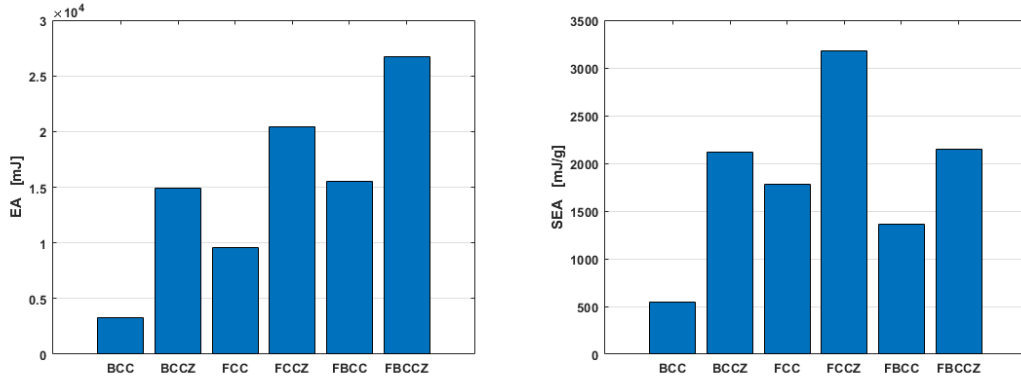


Figure 3.5: EA and SEA for the samples of dimensions 30x30x30 mm.

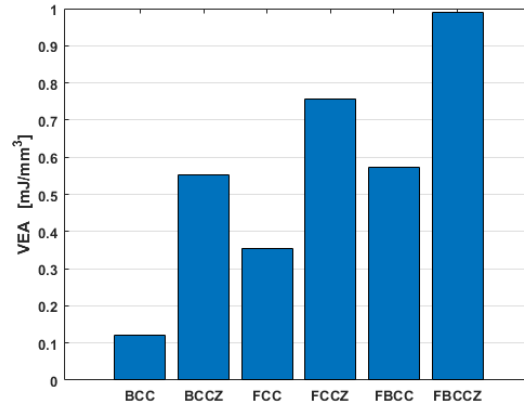


Figure 3.6: VEA for the samples of dimensions 30x30x30 mm.

### 3.2.4 Stress state analysis of the samples

Three beam stress results are included under the Beam Tool object of Ansys:

- Direct Stress;
- Minimum Combined Stress;
- Maximum Combined Stress.

The direct stress component is due to the axial load encountered in a beam element. From any bending loads a bending moment, in both the local Y and Z directions, arises so that four bending components (Y bending stress on top/bottom and Z bending stress on the top/bottom) can be calculated. The minimum bending stress is the lower one, while the maximum bending

stress is the higher of the four bending stresses. On the basis of these assumptions, it is possible to define the minimum combined stress as the linear combination of the direct stress and the minimum bending stress, while the maximum combined stress is the linear combination of the direct stress and the maximum bending one.

Von Mises stress, also called equivalent tensile stress, combines all the components into one value. The value of Von Mises stress is always positive and it can be related to the Maximum Combined Stress (output of Ansys for beam elements), if the absolute value is introduced. As proof of this, it is reported an example in the Figure 3.7. In order to parallel the Von-Mises stress, it is possible to consider a generic truss, with beam element and a circular cross-section, constrained at one end and subjected to a load along  $z$  at the other end. From the definitions previously analyzed, the Maximum Combined stress results, in absolute value, analogous to the Von-Mises stress, as can be seen from the plot in Figures 3.7 and 3.8 (in the case of modelling with 1D beam elements):

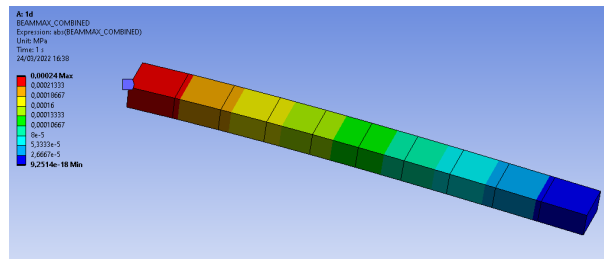


Figure 3.7: User define output equal to the absolute value of the maximum combined stress for a beam.

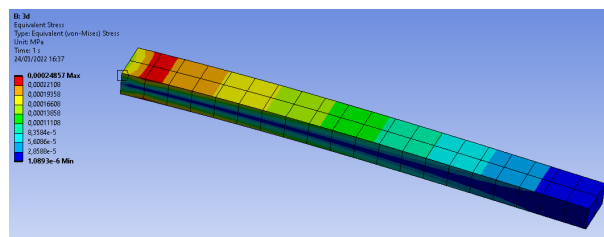


Figure 3.8: Von-Mises stress output in a 3D discretization.

By comparing the results obtained for the truss structure modelled with beam elements and considering a 3D approach, it is clear that, introducing the manual output equal to the absolute value of the maximum combined stress, the 'analogous Von-Mises stress' is obtained. (The analyses are conducted with the same material, BCs and loads.)



### 3.2.5 Stress field

Validated the definition of stress, in the analysis environment of the Ansys software, it is possible to manipulate the output in an automated way and obtain the desired value by entering the absolute value in 'User define output'. The results, shown in the Figure 3.9, 3.10 and 3.11 are comparable with the values obtained in [12] and are of interest to, identify the 'paths' in which the stress is maximum, by means of different graphic visualizations and schematizations proposed in the Figure 3.12.

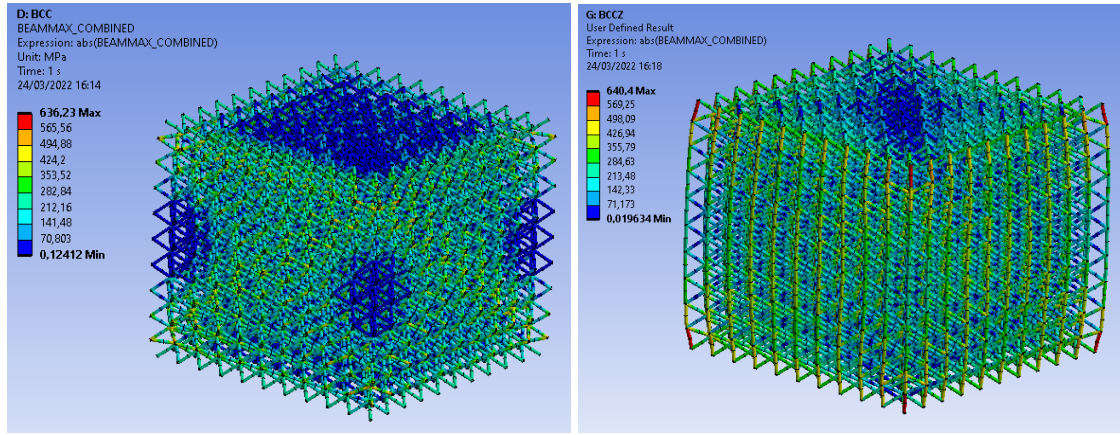


Figure 3.9: Stress field for BCC and BCCZ samples with 10x10x10 configuration.

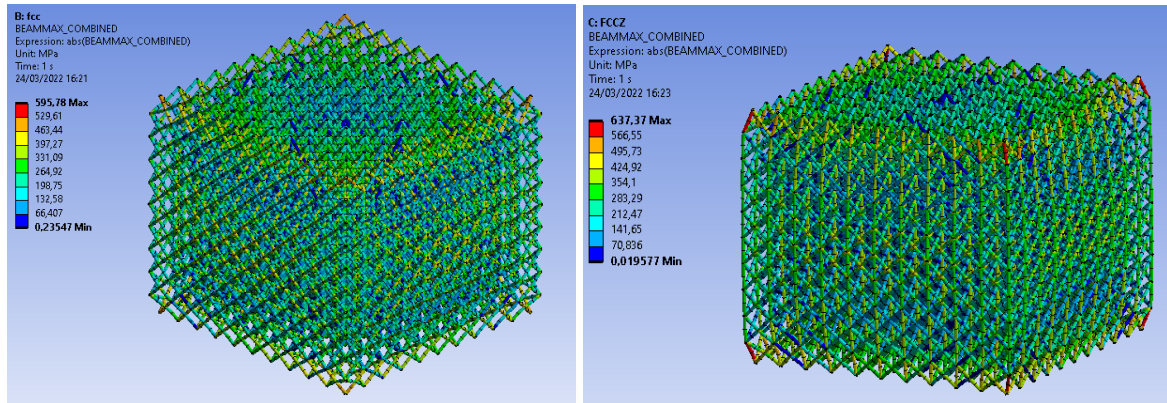


Figure 3.10: Stress field for FCC and FCCZ samples with 10x10x10 configuration.

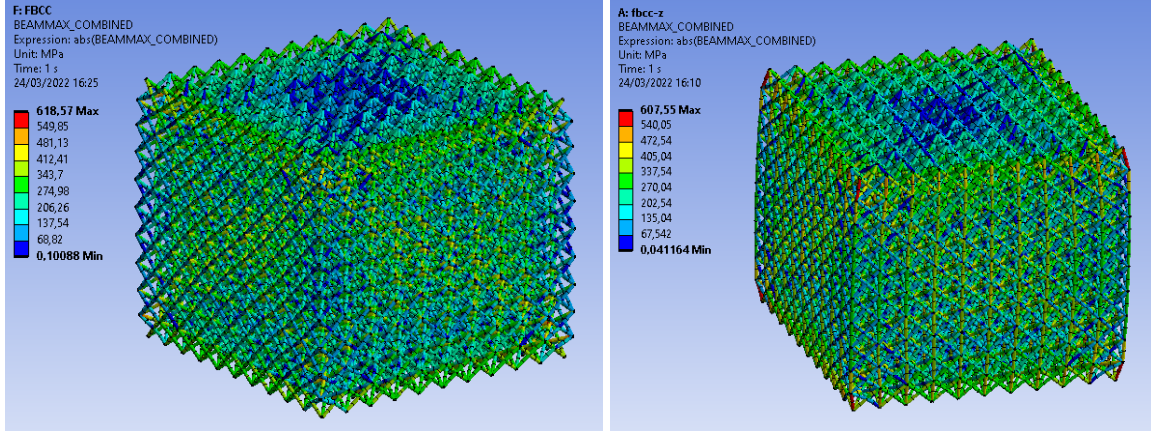


Figure 3.11: Stress field for FBCC and FCBCZ samples with 10x10x10 configuration.

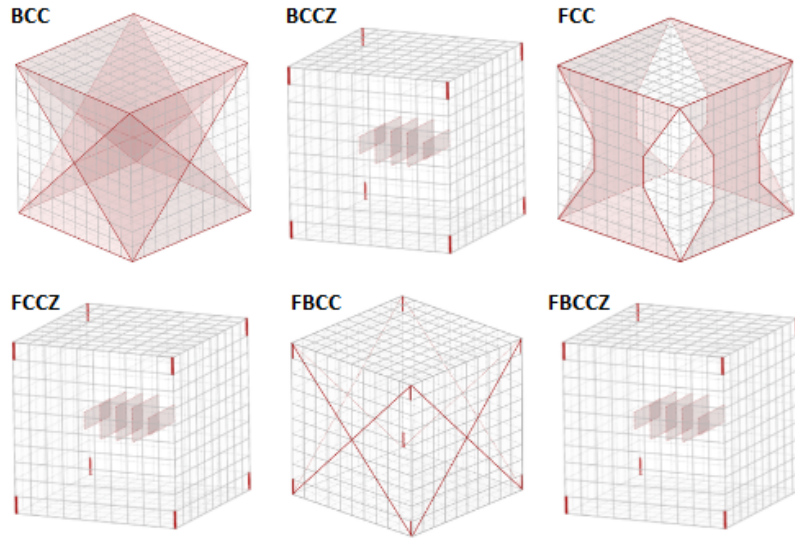


Figure 3.12: Qualitative schematizations of the stress fields for the six 10x10x10 samples.

The stress contours of the BCC and FCC lattice samples elucidate why shear planes emerge with different orientations, depending on the topology. The BCC specimens shows that the struts, connecting the diagonally opposite corners, carry greater stress than the others, and when diagonal shear planes emerge upon failure, they align with these most loaded struts. Similarly for the FCC specimens, it can be seen that stress is more concentrated in the struts connecting opposite corners, though for FCC these most loaded struts span the faces of the lattice structure, rather than across the whole sample. It is also apparent from the stress contours of the BCC and FCC topologies that stress is greatest in struts furthest from the central z-axis of the specimens, suggesting that bending moments are induced within the lattice structures during deformation, and as the moment arm increases in length the further from the centre

of the lattice, the struts on the outer faces carry the greatest stress. At a certain load, these induced stresses exceed the strength of the struts, leading to the emergence of diagonal shear planes. For FBCC-Z sample the 'preferential stress path' is a combination of the previous ones, in which diagonal lines appear on the faces, following the most solicited parts of the sample. In comparison, the BCCZ, FCCZ and FBCCZ configurations show that the z-struts carry the greatest stress. This is to be expected, as the z-struts are aligned to the load. The stress distributions also help to explain the differences between the different topologies in term of energy absorption. The BCC sample has the lowest specific energy absorption capabilities, and the reason for this is demonstrated by the significant variation in the stress states. As few struts are carrying significant stresses, while most struts are barely stressed at all, this leads to inefficiency of the structure and a reduction of the energy absorption is observed.

### 3.2.6 Deformation planes

The total deformations, that each specimen exhibits, are presented in the Figure 3.13. When failure occurred, two diagonal failure planes emerged for FCC, FCC-Z, FBCC and FBCC-Z samples, demonstrating that the orientation of failure planes is dependent on topology.

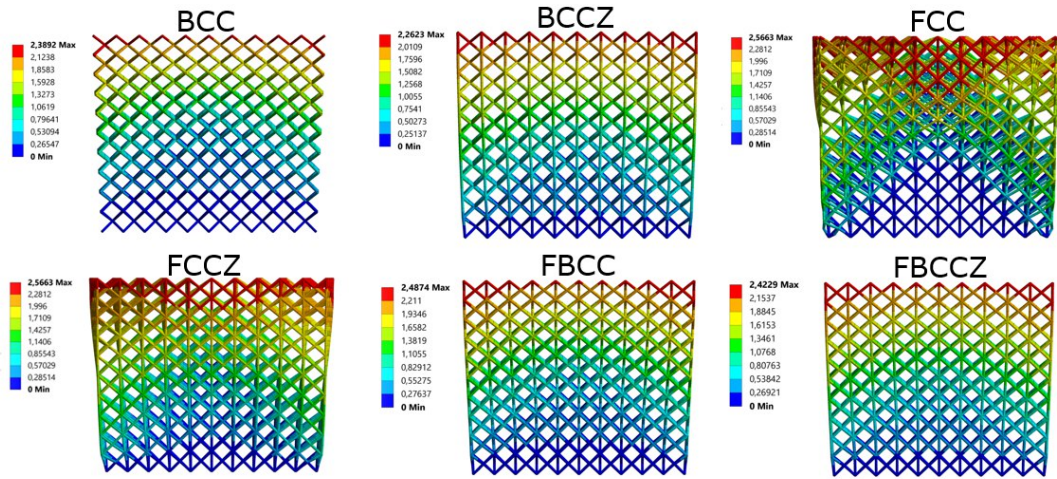
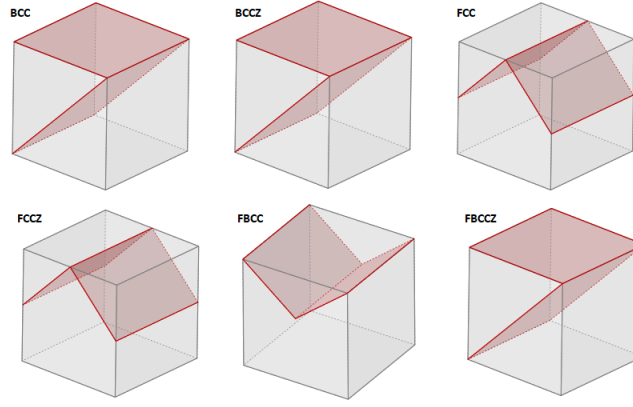


Figure 3.13: Total deformations of the six tested samples.

Specimens failed by the emergence of diagonal planes in which there's a concentration of stresses and the orientation of which is dependent on topology. The orientation of these planes is demonstrated by the numerical models that shows a concentration of the stress in struts connected diagonally (in the opposite corners of the structure).





*Figure 3.14: Deformation planes of the six 10x10x10 samples.*

For BCC, BCCZ and FBCCZ specimens present one diagonal failure plane, while FCC, FCCZ and FBCC show two diagonal planes of failure, which start from the upper central part of each sample. A general relation is extrapolated through the six different configurations: specimens failed by the emergence of diagonal shear planes, the orientation of which is dependent on topology. The reason for the orientation of these shear planes is correlated to the concentration of the stress, observed at the outer corners of each specimen. The failure paths follow these peaks, arranged in diagonal preferential planes, as will be confirmed by the experimental campaign described in Chapter 6. Therefore the interconnection between the modes of deformation and failure and the stress fields is closely related, in the following sections only the results in terms of stress have been reported, as elucidating the failure behavior.

### **3.2.7 Qualitative validation of the results**

In this sub-section a comparison with [12] is done. The models (analysed in the thesis) are not compared with the 3D-element discretized counterpart, but with the same approach with beam elements. This is only of interest to validate the results against established values in the literature. The six samples of size 30x30x30 mm with an aspect ratio of 8.1 will be compared with those describe in [12], in which the aspect ratio is 10.6 and the dimensions are 37.5x37.5x37.5 mm. Placing in similar load and boundary conditions and considering the same material (AlSi10Mg) for the models, it's possible to do a bilinear static study. The qualitative comparisons for SEA and VEA, show the same trends:





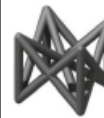
Topology	Body-centred cubic (BCC)	Body-centred cubic with z-struts (BCCZ)	Face-centred cubic (FCC)	Face-centred cubic with z-struts (FCCZ)	Face and body-centred cubic with z-struts (FBCCZ)
Image					
Struts ( $s$ )	8	12	16	20	28
Nodes ( $n$ )	9	9	12	12	13
Maxwell number ( $M$ )	-13	-9	-14	-10	-5
Struts oriented in load direction	No	Yes	No	Yes	Yes
Relative density of CAD model (%)	8.5	9.6	6.99	8.01	15.58

Figure 3.15: Characteristics and topologies. assumed in [12]

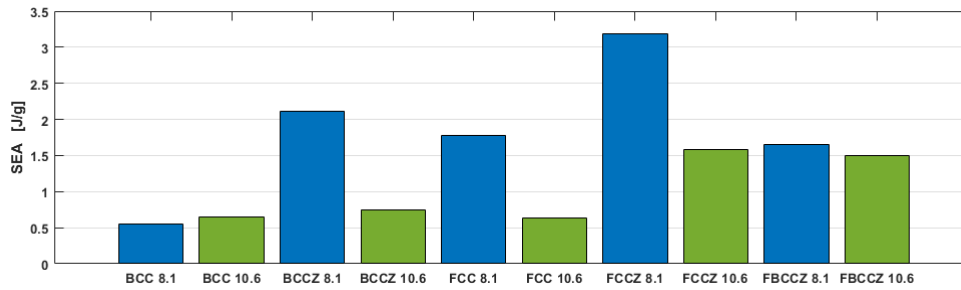


Figure 3.16: Overlaid comparison for SEA for the two 1D beam models, [11].

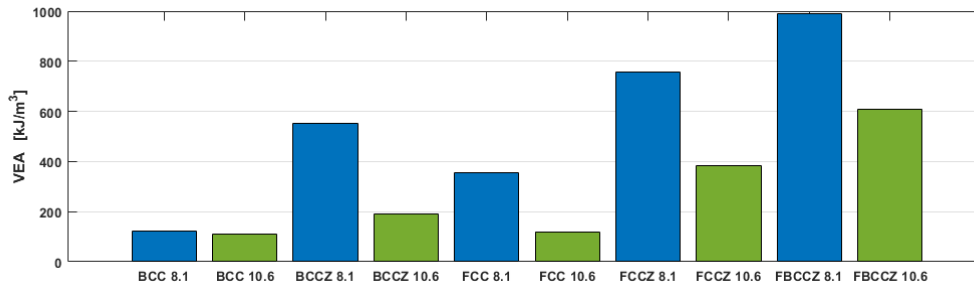


Figure 3.17: Overlaid comparison for VEA for the two 1D beam models, [11].

The trends are qualitatively the same and using similar geometries, loading and constraint conditions, the deviations, even from a numerical point of view, are acceptable.

From the point of view of the stress field, a further comparison can be made with the same results obtained in [12]. The previous stress analysis finds further correspondences with the data reported in the article, hence the same results are defined as above and explained in the Figures 3.18, 3.19 and 3.20, for the five configurations BCC, BCCZ, FCC, FCCZ and FBCCZ.

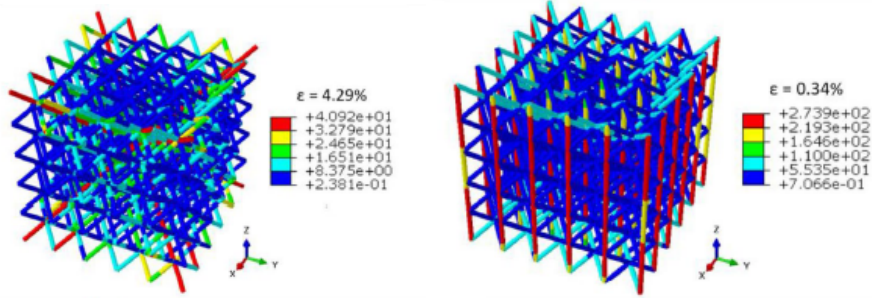


Figure 3.18: Von Mises Stress for BCC and BCCZ samples, [12].

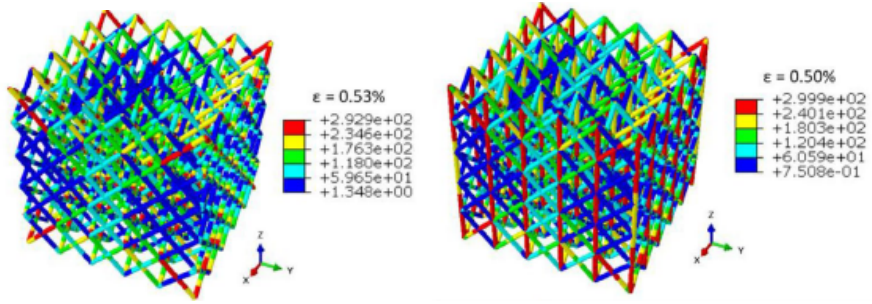


Figure 3.19: Von Mises Stress for FCC and FCCZ samples, [12].

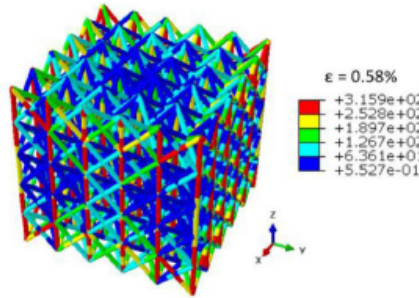


Figure 3.20: Von Mises Stress for FBCCZ sample, [12].

The study in the article also shows that in the presence of the vertical struts (BCCZ, FCCZ and FBCCZ), the stress peaks are distributed along z-lines, while for BCC there are diagonal planes inside. For FCC specimen, the planes with the greatest stress distribution are again diagonal, but distributed only on the outer faces. Therefore, corresponding trends are obtained for the specific and volumetric energy absorption values, as well as for the stress distribution, which turns out to be exactly the same. This allows us to fully validate the results obtained from the models implemented in the thesis, which will be carried forward for structural optimization (Chapter 5) and in the experimental campaign (Chapter 6).

### 3.3 Samples with (10,10,15) cells along (x,y,z)

Analogous to the previous study, also in these analyses each of the specimens is composed of elementary cells of size 3x3x3 mm and has 10 cells along X and Y axes and 15 cells along Z axis. Based on these assumptions, the total dimensions for each topologies are 30x30x45 mm. Element size is again equal to 1.5 mm and the material used is AlSi10Mg for the same reasons.

#### 3.3.1 Boundary conditions and loads

For each of the six specimens, a 'fixed' constraint for the bottom surface has been inserted and an 'imposed displacement' of -3 mm along the z direction has been applied to the upper surface. Compared to the previous analysis, only the imposed displacement conditions is changed to have the same level of deformation. This ensures a more truthful final comparison of the specimens, which are only found to have different dimensions along the z-axis, under the same all other conditions.

#### 3.3.2 Results

Based on the equations and data extrapolation methodologies explained for the 30x30x30 mm specimens, the results shown in the Table 3.3 are obtained.

	Eng. strain $\mu\epsilon$	Eng. stress [MPa]	Force Reaction Z [N]	EA [mJ]	SEA [mJ/g]	VEA [mJ/mm <sup>3</sup> ]
BCC	66666.667	1.2736	1146.30	3438.90	382.8060	0.0849
BCCZ	66666.667	7.4920	6742.80	20228.40	1917.0204	0.4995
FCC	66666.667	3.3458	3011.30	9033.90	1119.6643	0.2231
FCCZ	66666.667	9.5286	8575.80	25727.40	2669.5651	0.6352
FBCC	66666.667	6.8506	6165.60	18496.80	1084.7290	0.4567
FBCCZ	66666.667	13.0255	11723	35169	1888.6740	0.8684

Table 3.3: General results from bilinear static analyses for the 30x30x45 mm samples.

The stress-strain curves of the six specimens, are shown in the Figure 3.41 and the values, for each single load sub-step are calculated on the base of the same formula, but considering L equal to 45 mm:

$$\sigma_i = \frac{F_{Ri}}{A} = [MPa] \quad (3.6)$$

$$\epsilon_i = \frac{F_{Ri}}{L} = [-] \quad (3.7)$$

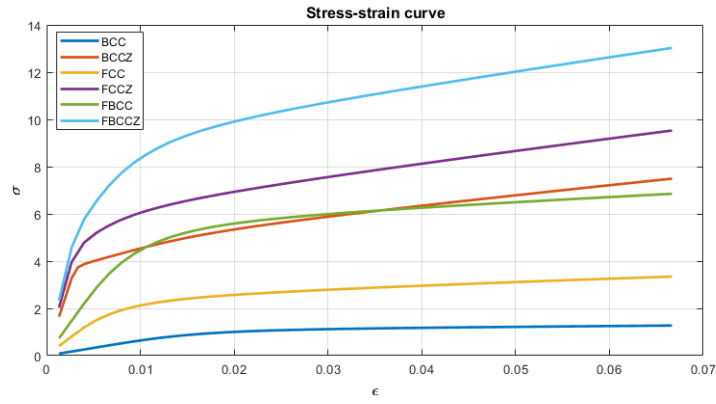


Figure 3.21: Stress-strain curve for the six samples of dimension 30x30x45 mm.

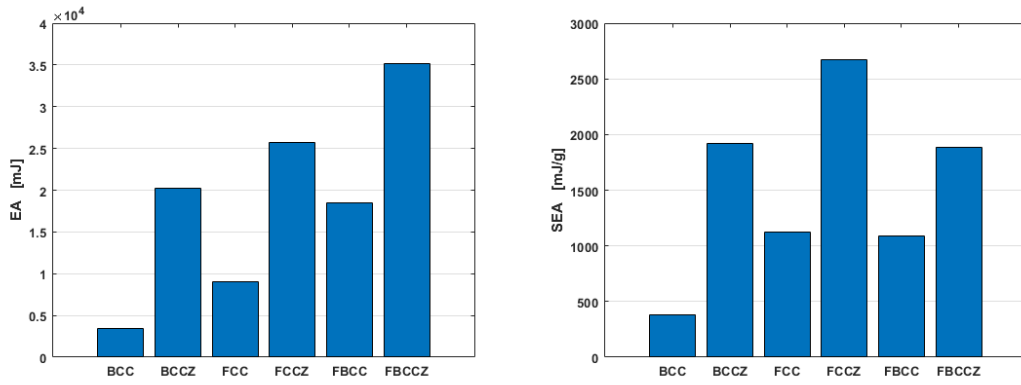


Figure 3.22: EA and SEA of dimension 30x30x45 mm.

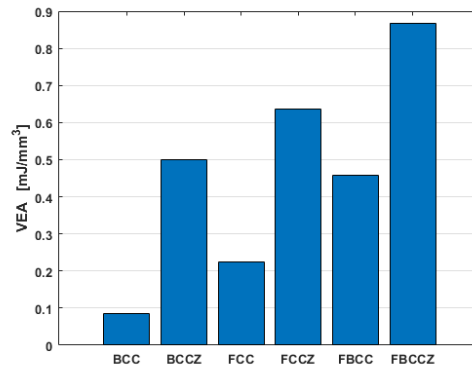


Figure 3.23: VEA for the six samples of dimension 30x30x45 mm.



### 3.3.3 Stress field

The extrapolation of the stress field is of primary interest, so the previous approach is followed, by entering a manual output via the command 'User define output' and obtaining the 'equivalent' Von-Mises stress:

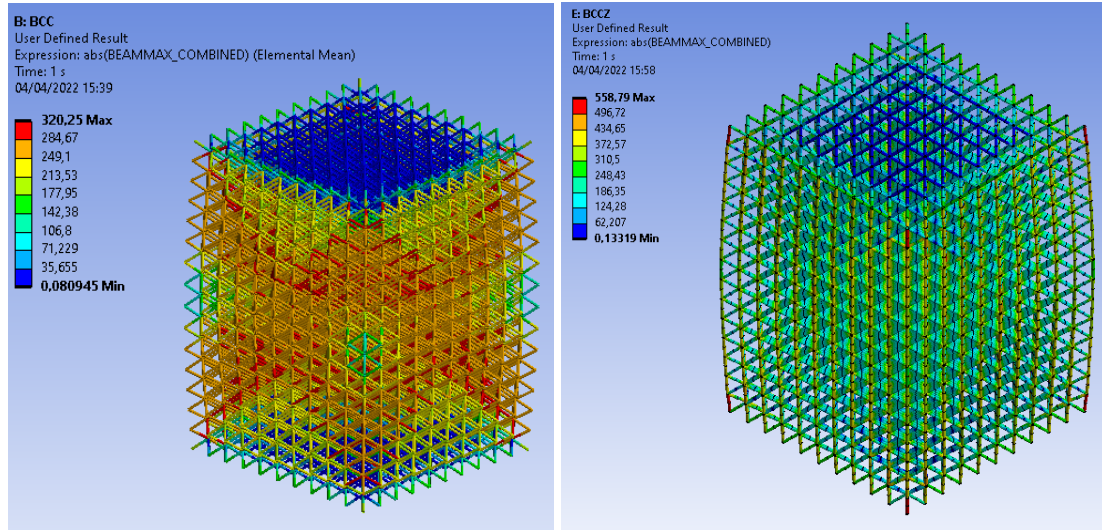


Figure 3.24: Stress field for BCC and BCCZ samples with 10x10x15 configuration.

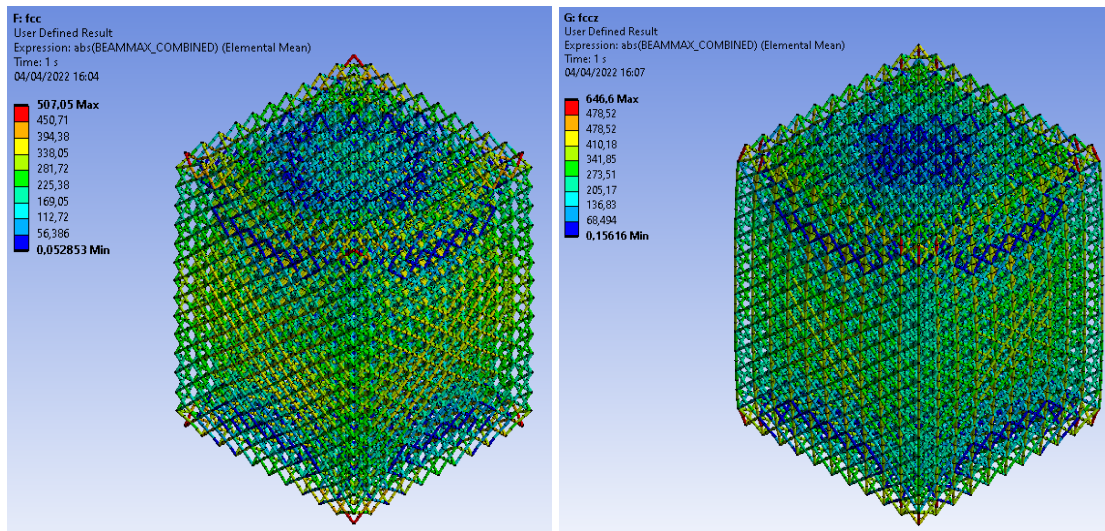


Figure 3.25: Stress field for FCC and FCCZ samples with 10x10x15 configuration.

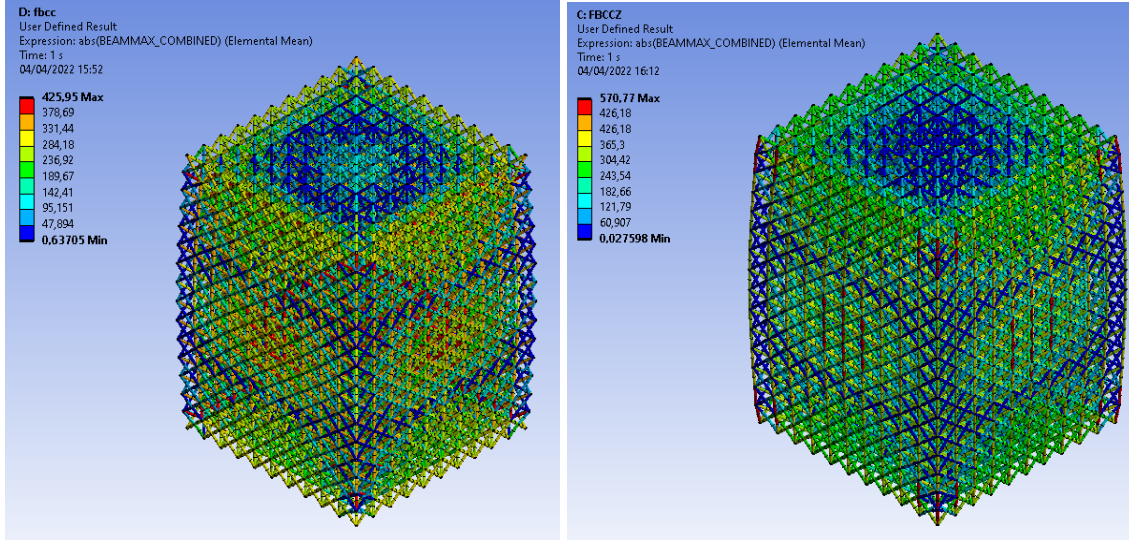


Figure 3.26: Stress field for FBCC and FBCCZ samples with 10x10x15 configuration.

The stress fields are similar, but with a reduction of the edge effects, due to the larger dimensions of the structure. This allows to have results whose reliability is greater, as in the outermost areas such effects occur with reduced intensity.

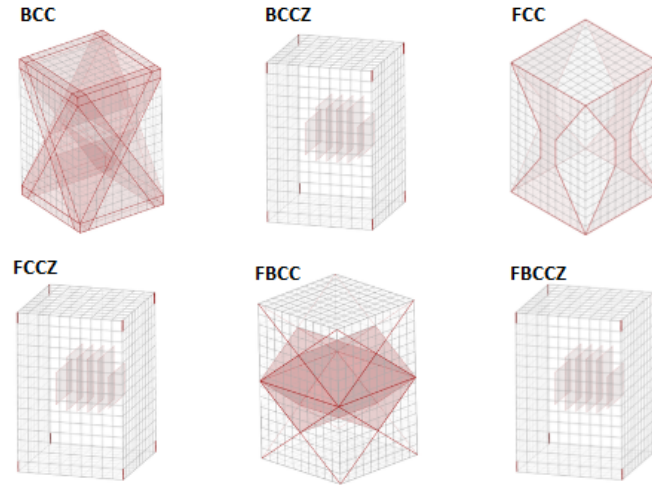


Figure 3.27: Qualitative schematizations of the stress fields for the six 10x10x15 samples.

### 3.4 Samples with (10,10,20) cells along (x,y,z)

In this case each of the specimens is composed of elementary cells of size 3x3x3 mm and has 10 cells along X and Y axes (length and width) and 20 cells along Z axis (height). Based on these assumptions, the total dimensions for each topologies are 30x30x60 mm. The mesh size is equal to 1.5 mm and the material adopted is the same as that used in the previous sections.

### 3.4.1 Boundary conditions and loads

It is selected, for each of the six samples, the same boundary conditions and imposed displacement. For the bottom side, a 'fixed' constraint is chosen, while an 'imposed displacement' of -4 mm along the z direction has been applied to the upper surface to ensure the same deformation as the other two cases with dimensions of 30 mm and 45 mm along the z-axis.

### 3.4.2 Results

For the sake of brevity, as all calculation procedures and methodologies are the same, the results are given directly in the Table 3.4. The mechanical behaviour is quite similar to that of the first two cases and it is summarised by comparing the stress-strain curves. As far as the energy values are concerned, EA, SEA and VEA are elucidated, with trends confirming the results provided.

	Eng. strain $\mu\epsilon$	Eng. stress [MPa]	Force Reaction Z [N]	EA [mJ]	SEA [mJ/g]	VEA [mJ/mm <sup>3</sup> ]
<b>BCC</b>	66666.6	1.2168	1095.1	4380.4	365.7	0.081119
<b>BCCZ</b>	66666.6	7.3259	6593.3	26373	1874.4	0.48839
<b>FCC</b>	66666.6	2.4304	2187.4	8749.6	813.31	0.16203
<b>FCCZ</b>	66666.6	8.7191	7847.2	31389	2442.7	0.58127
<b>FBCC</b>	66666.6	6.4626	5816.3	23265	1023.3	0.43084
<b>FBCCZ</b>	66666.6	12.5689	11312	45248	1822.5	0.83793

Table 3.4: General results from bilinear static analyses for the 30x30x60 mm samples.

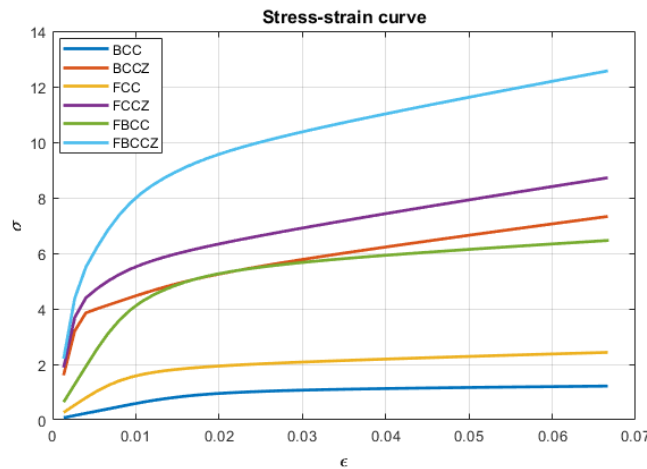


Figure 3.28: Stress-strain curve for the six samples of dimensions 30x30x60 mm.

The calculation of the absorbed energy is related to the force reaction obtained in the output and the imposed displacement of 4 mm (absolute value). Introducing these input, EA, SEA and VEA are calculated:

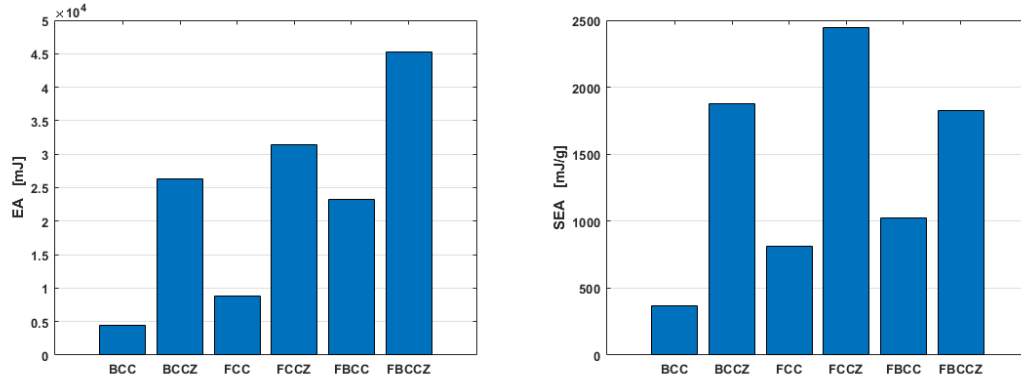


Figure 3.29: EA and SEA for the six samples of dimensions 30x30x60 mm.

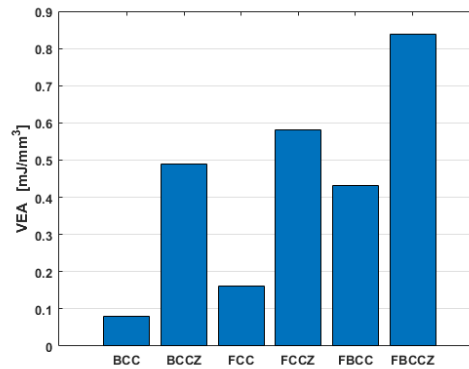


Figure 3.30: VEA for the six samples of dimensions 30x30x60 mm.

### 3.4.3 Stress field

Regarding the 'Von-Mises stress' plot, reference is made to Figures [3.31](#), [3.32](#) and [3.33](#), in which it is define configurations with diagonal multi-planes, schematized in [3.34](#).



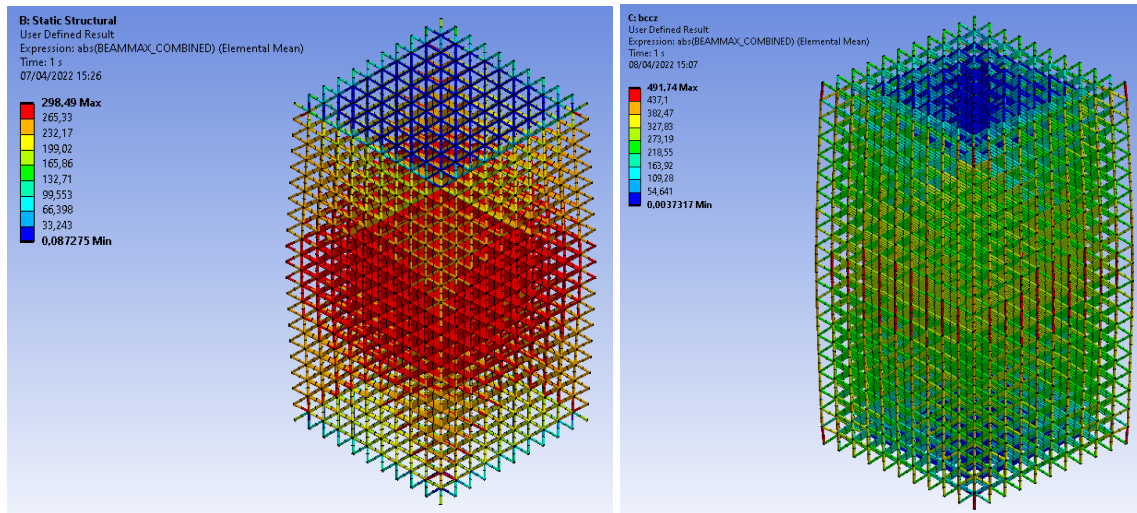


Figure 3.31: Stress field for BCC and BCCZ samples with 10x10x20 configuration.

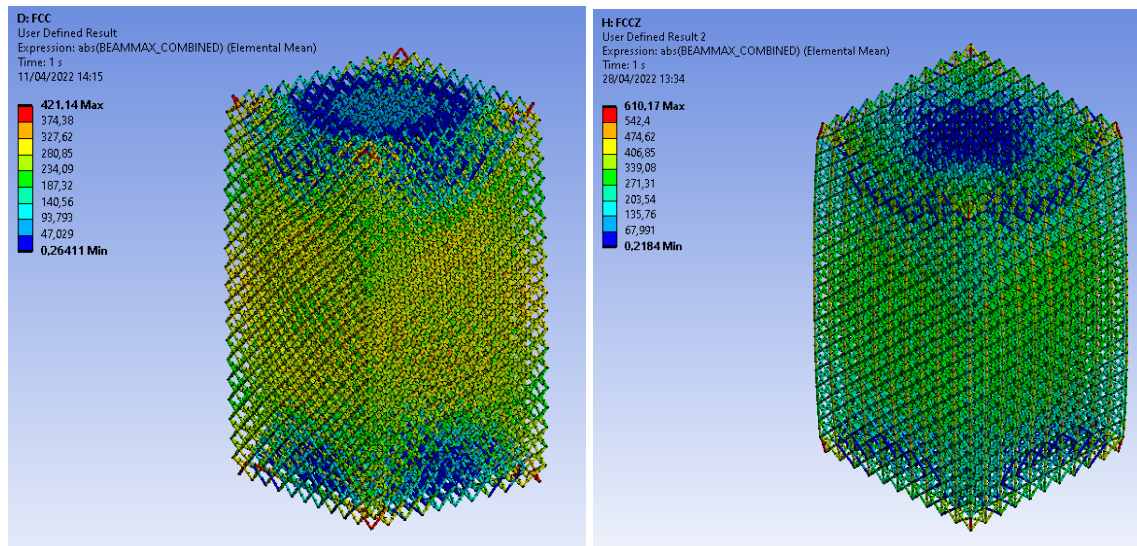


Figure 3.32: Stress field for FCC and FCCZ samples with 10x10x20 configuration.

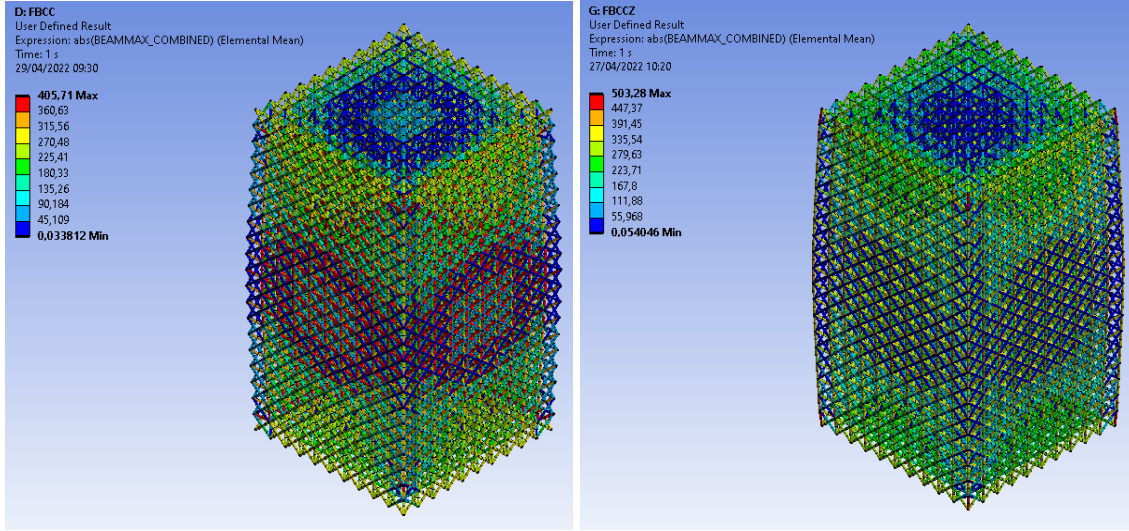


Figure 3.33: Stress field for FBCC and FBCCZ samples with 10x10x20 configuration.

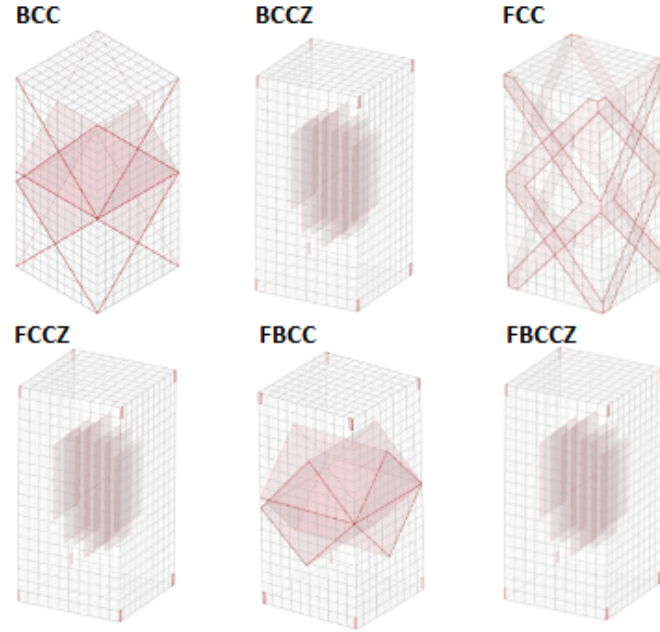


Figure 3.34: Qualitative schematizations of the stress fields for the six 10x10x20 samples.

The stress field obtained are similar to those analyzed in the other two cases, for the specimens having as number of cells a value equal to 10x10x10 and 1010x15. For the 10x10x20 configuration, a reduction of the size effects (due to the larger dimensions of the structure) is clear from the stress field, leading to an higher level of accuracy.

### 3.5 Middle region evaluation

A comparison of the three configurations (for the six specimens) shows that, by introducing struts along z (BCCZ, FCCZ, FBCCZ), a 'side 3D area' is delineated. The middle volume indicates a concentration of stresses along the vertical struts. This zone varies in extent according to the size of the specimens. As expressed in the Table 3.5, this region follows proportionally the dimensions of the specimens, assuming a length  $L_z$  equal to 12 mm, 21 mm and 30 mm for the dimensions of 10 mm, 15 mm and 20 mm in the case of BCCZ and FBCCZ cell selections, while, considering FCCZ, the values are 9 mm, 18 mm and 27 mm.

	$L_x[mm]$	$L_y[mm]$	$L_z[mm]$	$V[mm^3]$
<b>BCCZ - 10x10x10</b>	24	24	12	6912
<b>FCCZ - 10x10x10</b>	18	18	9	2916
<b>FBCCZ - 10x10x10</b>	24	24	12	6912
<b>BCCZ - 10x10x15</b>	24	24	21	12096
<b>FCCZ - 10x10x15</b>	18	18	18	5832
<b>FBCCZ - 10x10x15</b>	24	24	21	12096
<b>BCCZ - 10x10x20</b>	24	24	30	17280
<b>FCCZ - 10x10x20</b>	18	18	27	8748
<b>FBCCZ - 10x10x20</b>	24	24	30	17280

Table 3.5: Dimension along (x,y,z) of the middle stress band.

With reference to the data in the Table 3.5 and in the Figures 3.12, 3.27 and 3.34, in which there is a clear pattern of the internal stress field for the specimens with z-struts, it can be seen that as the dimensions along the vertical axis increase, the zone with the highest concentration of central stress tends to extend. This is expected as the two parameters are closely related, for greater height of the specimens the internal area under stress expands, but not proportionally, as the edge effects, described in the next sections, show a decrease.

### 3.6 Effect of variable imposed displacement

In this subsection an analysis on a sample with BCC topologies is carried out. It is composed of elementary cells of size 3x3x3 mm and has 10 cells along X and Y axes (length and width) and 20 cells along Z axis (height). Based on these assumptions, the total dimensions for each topologies are 30x30x60 mm. The mesh size is set to 1.5 mm and AlSi10Mg is chosen as mate-

rial. The real difference is due to the different load applied, using an 'imposed displacement' of -2 mm along the z direction (different from the starting value of -4 mm), while a 'fixed' constraint for the bottom surface has been inserted as boundary conditions. Using force and sample section area, as well as displacement and edge length, it is possible to evaluate physical and mechanical properties:

	Eng. strain	Eng. stress	Force Reaction Z	EA	SEA	VEA
	$\mu\epsilon$	[MPa]	[N]	[mJ]	[mJ/g]	[mJ/mm <sup>3</sup> ]
BCC	33333.3	1.0923	983.05	1966.1	164.1426	0.0364

For the stress field point of view, the preferential distribution is very similar to the configuration BCC 10x10x20 (cells) with an imposed displacement of -4 mm on the upper surface. A close relationship exists between BCC specimens with dimensions 10x10x10 and 10x10x20 applying both the same level of displacement and deformation (case with imposed displacement of -4 mm). It is of interest to correlate the stress fields and values in terms of mechanical and energy performance. Indicating with:

- CASE 1 for the specimen BCC 10x10x10 and displacement equal to -2 mm;
- CASE 2 for the specimen BCC 10x10x20 and displacement equal to -2 mm;
- CASE 3 for the specimen BCC 10x10x20 and displacement equal to -4 mm.

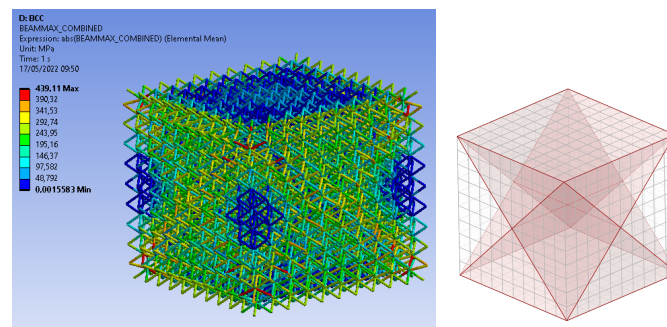


Figure 3.35: Case 1, Von Mises Stress and corresponding qualitative schematization.



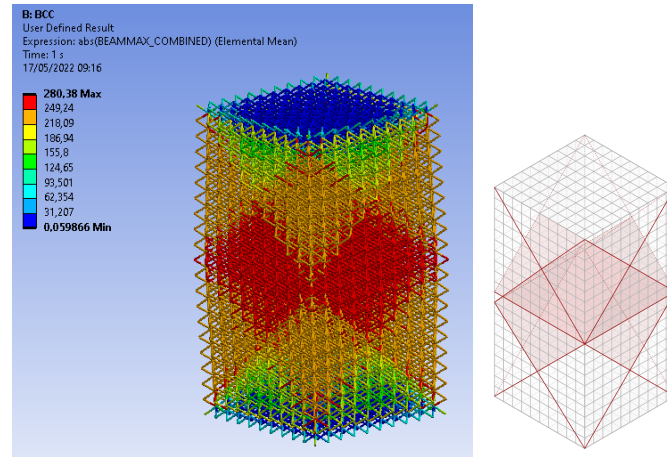


Figure 3.36: Case 2, Von Mises Stress and corresponding qualitative schematization.

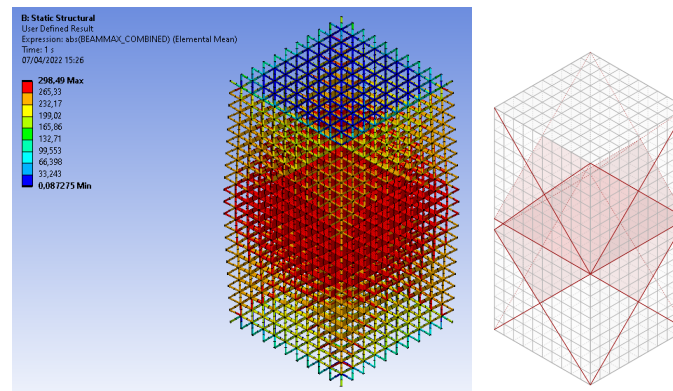


Figure 3.37: Case 3, Von Mises Stress and corresponding qualitative schematization.

From the point of view of mechanical properties, the stress-strain curve has an obvious reduction in stress values, moving down compared to the Case 1. For Case 2, considering an imposed displacement equal to -2 mm, the final strain value is lower than Case 3, as can be appreciated by the trend depicted in the Figure [3.38](#):

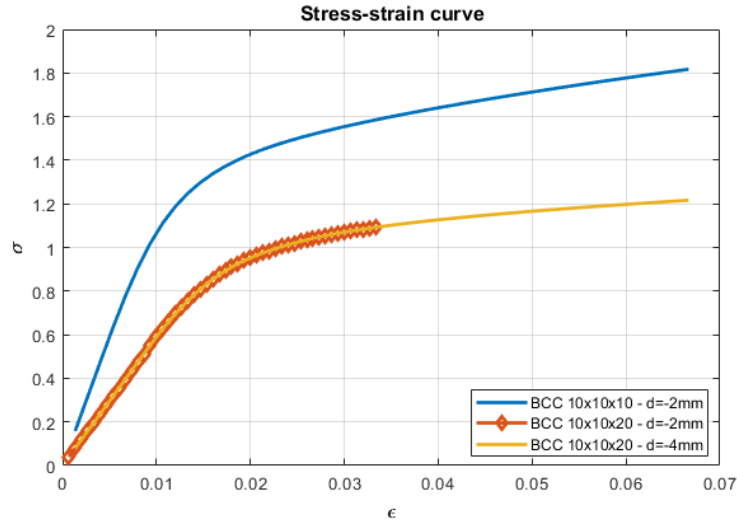


Figure 3.38: Comparison of the stress-strain curves for the case 1, 2 and 3.

This decrease is strictly related to the output values obtained for Force Reaction, which are lower for the BCC 10x10x20 specimens, as it is clear in the Figure 3.38. Instead, from SEA and VEA point of view, for the correlations with the Force Reaction, the configuration of the Case 2 shows a reduction of 39.9% and 69.9% in comparison with the 10x10x10 cells (with the same BCs and imposed displacement).

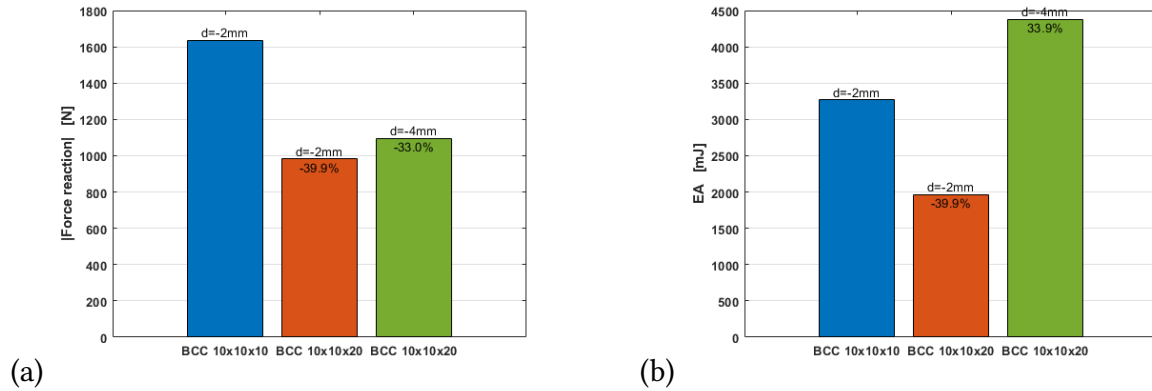


Figure 3.39: Comparison of (a) Force Reaction and (b) EA, for the Case 1, 2 and 3.

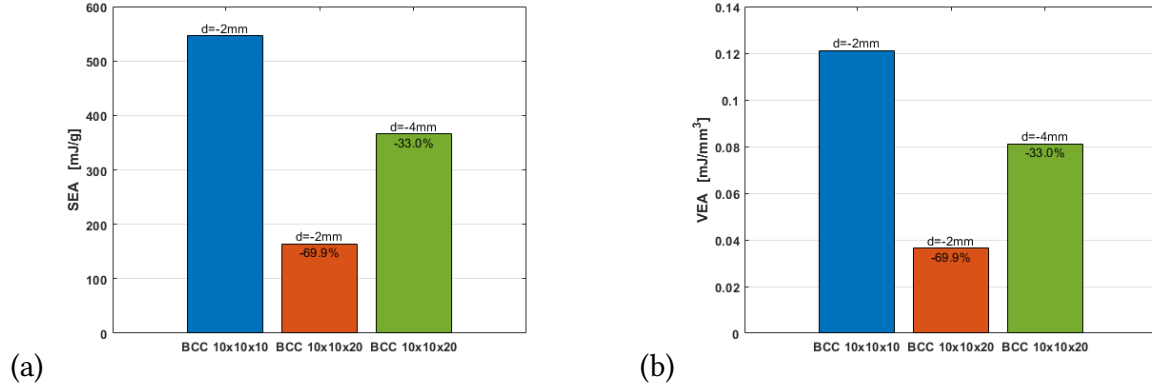


Figure 3.40: Comparison of (a) SEA and (b) VEA, for the Case 1, 2 and 3.

### 3.7 Size effects

When the material properties of lattice structures are tested, small samples may have different apparent material properties than large ones. This difference is known in the literature as a size effect [54]. The study confirms that the variability of effect sizes diminish with increasing sample size. The samples exceed more than about 20 cell layers, the edge effect decreases quickly to be neglected ([55]). The edge effects of the equivalent specific strength also obey these rules. The reduction of the equivalent specific stiffness and strength is mainly derived from the mass enhancement of struts. When the dimensions of the samples increase, a sort of reduction of local concentrations of strain and stress is shown, which is strongly related to the topology. From the analysis done in the previous chapter, cellular materials can be divided into bending dominated and stretching dominated topologies. Stretching dominated cellular materials tend to be stiffer than bending dominated ones and, considering these classifications, it is possible to examine the size-effects for the six proposed configurations, relating the specimens of size 10x10x10, 10x10x15 and 10x10x20. As the specimen size increases, a stress variation will be seen. The distribution is the same but for the BCC, FCC and FBCC configurations, there is external zones with different stress peaks. For BCC there are present diagonal lines on the external surface and an area of concentration of stress are elucidated. For FCC the peaks of stress are concentrated along the four diagonal planes and the effects of the size is not really relevant. It's possible to see differences only in the corner zone with a more defined area for the maximum values for the bigger samples. The same is shown for FBCC, which represents a mix of all six topologies, presenting at the same time all the different load-paths. Looking

at this representation it can be seen that the edge effects, in terms of stress distribution, are reduced as the specimen size increases. A similar argument is proposed for specimens fitted with z-struts. The latter have stress concentrations at the outer edges (vertices) and along the vertical struts. As the size of the specimen increases, the concentration along vertical struts is reduced only for the middle and not along the whole height. A comparison of the mechanical and energy characteristics shows that, as the size increases, and the same level of deformation is imposed, the output stress and force reaction are lower. The shape of the stress-strain curves is similar for the entire range of specimen sizes, although the actual values of stiffness and strength is varied for the different specimen sizes. By imposing a displacement for the 10x10x10 specimen of 2 mm (compression), for the 10x10x15 of 3 mm and 10x10x20 of 4 mm and evaluating EA, by the product of constraint reaction and displacement, an increasing trend with size is obtained, while for SEA and VEA the values are progressively decreasing.

### **3.8 Sensitivity analysis for accuracy study**

On the basis of the bilinear simulations carried out, it can be seen that for each of the six configurations there are peak stress values at the corners. This tends to skew the results and influence the accuracy. From the sensitivity analysis, an element size of 1.5 mm is chosen, implying 2 elements per strut. This provides valid outputs, but this veracity does not include the stress-field. As a proof of the above, it is possible to conduct a bilinear sensitivity analysis again on a BCC specimen of size 10x10x10 and evaluate the outputs and stress field accordingly. Assuming the same material, boundary conditions and loads, a comparison in terms of stress-strain curves is shown. The trend is the same, with slight deviations for the plastic section where it can be seen that, assuming a less dense mesh, the stresses are overestimated (higher curve):

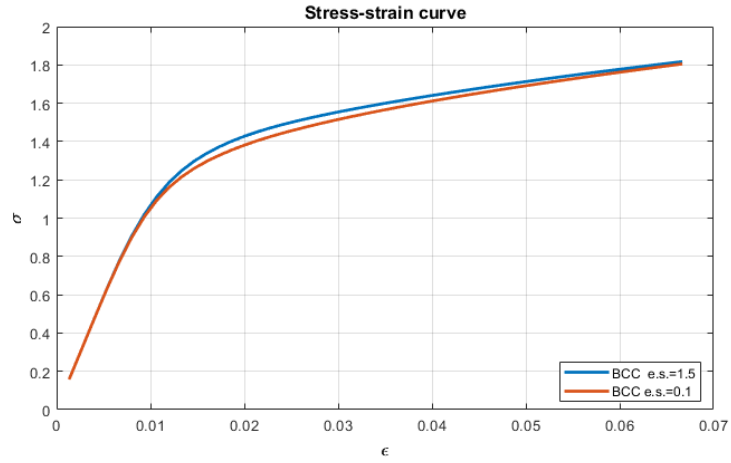


Figure 3.41: Stress-strain curve, varying mesh size.

The percentage variations in energy terms are small (0.7%), so the previous results are reliable even with a rougher mesh.

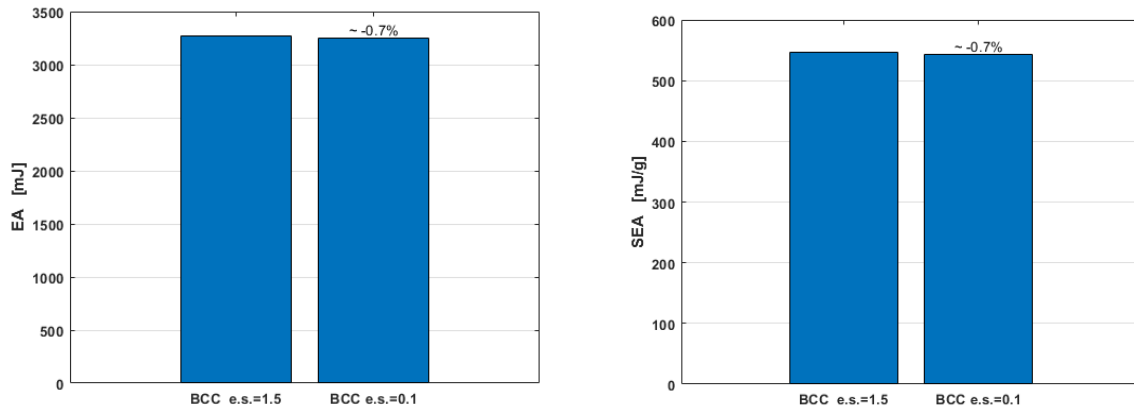


Figure 3.42: EA and SEA, varying mesh size.

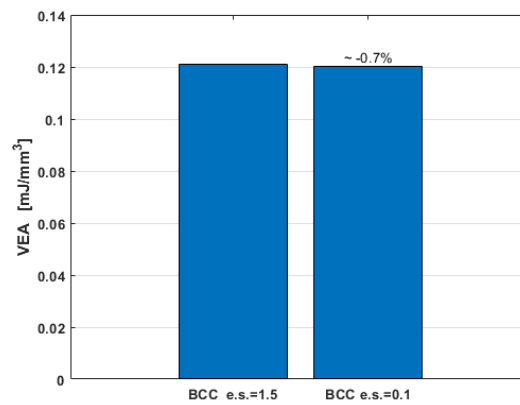


Figure 3.43: VEA, varying mesh size.

The largest variation affect the stress field. The peaks recorded, in the case where only two elements have been entered for each strut, show larger areas with  $\sigma$  major. This is solved by selecting a value of 0.1 mm as element size. This choice triples the computational times, but solves the problem described above. A direct comparison of such distributions is shown in the Figure 3.44, in which the stress field obtained, with the two different element sizes selected, can be appreciated. The configuration of the preferential paths is the same, but it can be seen, in relation to the image 3.44 (a), that the 'size effects' are considerably reduced by choosing smaller sizes, thus increasing accuracy.

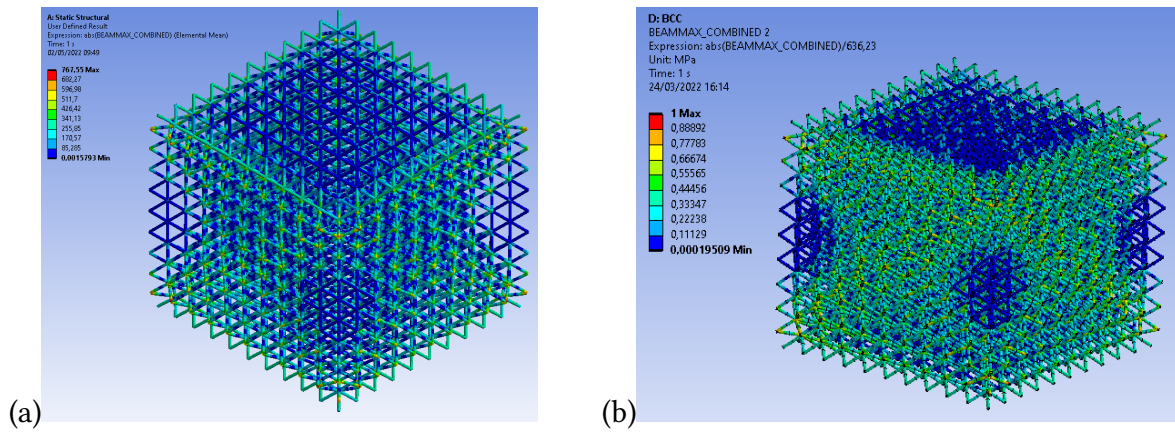


Figure 3.44: BCC stress field for a mesh size of (a) 0.1 mm and (b) 1.5 mm.

Although the accuracy increases and problems with staggered stress concentrations are resolved, the results in terms of mechanical and energetic properties tend to coincide. This leads to a design choice of a less fine mesh (1.5 mm), in order to achieve sustainable calculation times and fully reliable numerical outputs.

### 3.9 Computational time for the three sample sizes

The introduction of a beam model has allowed great time-savings in terms of analysis costs. They are reduced in comparison to their counterparts discretized with 3D elements. In this section, further comparisons will be made in terms of computational costs, but in this case based on the dimensions of the specimens, which vary with the first case with (30,30,30) mm along (x,y,z), the second with (30,30,45) mm and the third with (30,30,60) mm. The computational costs in time are related to a computer in the department's offices of the Konstruktiver Leichtbau und Bauweisen (KLuB - TU Darmstadt), whose technical specifications are given in the Table 3.6.

Category	Hardware/Software
Operating system (OS)	Windows 10 64-Bit system
Central processing unit (CPU)	Intel(R) Core(TM) i7 CPU 70 @ 2.93GHz
Random-access memory (RAM)	20,0GB DDR3
Graphics processing unit (GPU)	NVIDIA GeForce GT 610

*Table 3.6: Computer technical specifications used for the analyses.*

	10x10x10 cells	10x10x15 cells	10x10x20 cells
<b>BCC</b>	2h 11m	3h 28m	6h 38m
<b>BCCZ</b>	2h 42m	3h 44m	7h 12m
<b>FCC</b>	2h 07m	3h 21m	6h 54m
<b>FCCZ</b>	3h 49m	5h 7m	7h 47m
<b>FBCC</b>	6h 31m	6h 48m	9h 13m
<b>FBCCZ</b>	7h 16m	7h 52m	11h 22m

*Table 3.7: Time costs for all the static analyses done.*

As expected, increasing the size of the specimens along the z-direction, the number of struts and consequently the number of beam elements to be inserted during the meshing process are always greater. In this respect, there are increasing, but still small time ranges, as can be seen in Table 3.7. From the analyses conducted and the comparison of computational costs in time, it is clear that the 10x10x10 configuration of specimens appears to be the best for future analysis. It has small dimensions, which expand the edge effects, but lends itself well to faster analyses, so it provides for the possibility of conducting a larger multi-facet studies.

## Chapter 4

# Topological optimization of the samples

Each of the six specimens considered in the previous Chapter, on which bilinear analyses are carried out, present very different characteristics and mechanical performances. The primary purpose of this section is to recreate a clear database of the performance achieved and attempt to increase it through an optimization process. On the basis of past works [56], it is clear how recreating a specimen, by gradually varying the relative density of certain struts, can be a valid option to lead to homogenization of the stress field and consequently better energy characteristics. Every elementary structure play an important role in mitigating the brittle failure, promoting progressive damage. This has led to enhanced energy absorption characteristics.

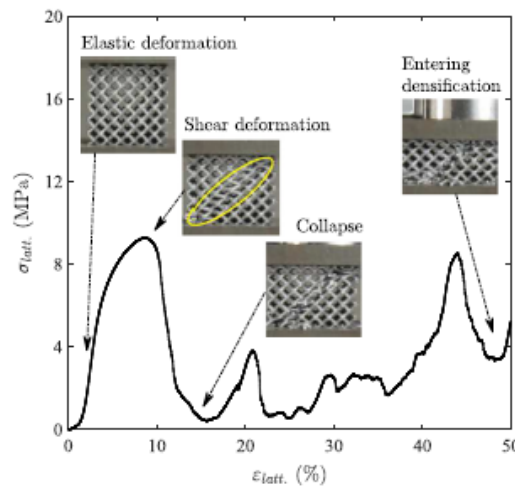


Figure 4.1: Stress-strain curve of graded lattice structures, [13].

In contrast to the uniformly dense lattice structures, those with graded density show novel deformation behaviour, as can be seen in [57] and [13]. Beginning with the layers of lowest relative density, the graded lattices tend to collapse in a layer-by-layer sequence (Figure 4.2)



and the sequential layer collapse can be seen in the trends of the stress-strain curve. The sequential layer collapse continue up to the densification of the final layer, at which point the stress rise drastically, as will later be confirmed by the experimental campaign (Chapter 6). Another way to increase a the level of EA, recreating a sort of 'breaking-path', is the adoption of a multi-morphological design. Different types of cells can be used in the same sample to achieve multi-morphology designs as well: the concept is very similar to graded structures, but there is the possibility to gather different properties and different behaviours. [58] is an example, where optimization process has been used as well. In [14], using four kinds of unit cells (BCC, FCC, BFCC, and BFVC), three sorts of patterns (horizontal, vertical, and circular) are constructed.

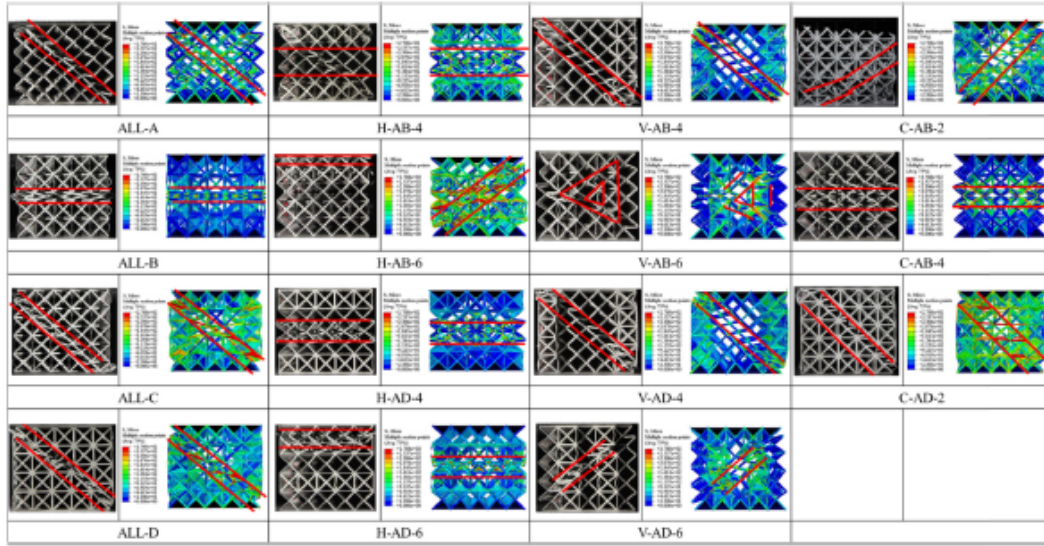


Figure 4.2: Comparison of deformation modes, [14].

The topological arrangement of different unit cells plays a prominent role in determining energy absorption performance, leading to an improvement in this parameter.

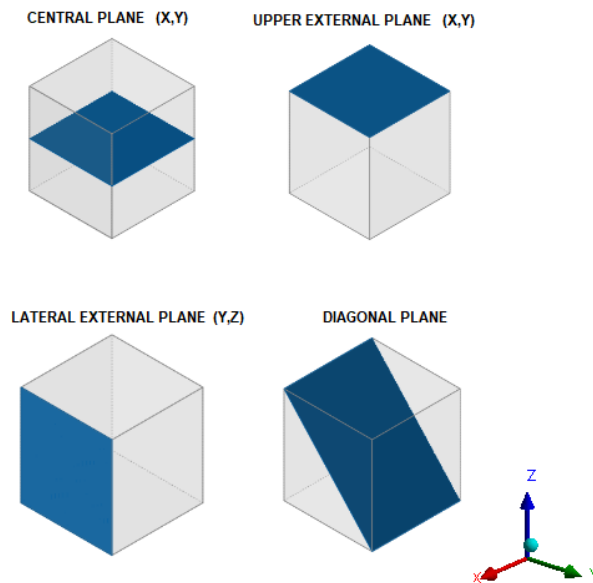
## 4.1 Data extraction in table format

Based on the literature work previously mentioned, it has been decided to increase the properties of the smaller specimens (10 cells per side) by systematically varying the thicknesses of the struts. First of all, in order to manage and increase both the mechanical and energetic efficiency of the specimens, it is necessary to reconstitute a sort of 3D database of the stress values, for each single cell. After performing the static bilinear analysis in Ansys Mechanical,

it is possible to extrapolate the files '.out', generated by the software. In these files there is the identification of each element and the values of the requested outputs. These values have been imported into Matlab, so it has been possible to recalculate, known the ID of the element and its precise geometric position (x,y,z), the maximum value of the stress for each cell of the entire sample 10x10x10. A complete 3D database is created for all six configurations, but only the most representative zones are extracted as 2D planes, in the form of grids, in order to represent as clear as possible the stress distribution. Therefore it has been chosen to represent, according to schemes [4.3](#), the following 2D layers (planes) of the samples:

- Central plane;
- Upper external plane;
- Lateral external plane;
- Diagonal plane.

The proposed schematizations are shown in the Figures below, indicating the planes selected for investigation (as representative of global behaviour):



*Figure 4.3: Characteristic planes for the representation of mechanical and energetic properties within samples (extraction of 2D databases from the global 3D one).*

Implementing the Matlab code, it is thus possible to have a visual display of the stress field and introduce an appropriate colour scale to delineate the areas of high concentration, as can be

seen in the Appendix [A.1]. The specimens have the same struts diameter for each cell, which generates an inhomogeneous stress field and the failure mechanisms described in the previous chapter. According to the outputs provided by Ansys Mechanical, the tabular schematizations representing 2D planes can be used to create the same grids, but whose representations concern dimensional quantities, mechanical and energy properties.

In the following paragraphs, simple formulations are set out to determine the same 3D databases, from which extract 2D tables, for thicknesses, SEA and VEA.

## 4.2 Optimization of diameters

Lattice structures consist of a large number of struts arranged in spatial patterns with selected unit cell design. The cells' optimal diameter has been the focus of numerous studies. Michell [59] developed a criterion for a minimum mass for the struts, according to which all structural members must be strained by the same amount. The required deformation leads to the fact that members are arranged in a frame that is aligned with principal stress directions. A limitation of this work is that its implementation is restricted to simple geometries. In the years since, other computational methods have been developed, including size and topology optimization approaches. Size optimisation can be used to parametrically control the individual diameters of each struts in any lattice configuration and under external loads. In contrast, topology optimization methods are generally concerned with achieving binary solid-void solutions. With topology optimisation the less stressed elements are assigned an artificially softer material through penalty methods. In this way, holes in the structure can be approximated as regions of low density below a defined threshold, and an optimal material layout can be determined. Various topology optimisation approaches have been developed over recent years [17], [60], [61] and [62] including density-based and bio-inspired methods or using a combined methodology to identify principal stress directions and to optimize diameters with the established isostatic stress lines [63].

## 4.3 Optimization processes

### 4.3.1 First process

In the context of this discussion a process is proposed for an optimization of the structural properties, starting from the internal stress field of each specimen. The main purpose of the optimization is to uniform the stress field for each of the topologies: this will allow to obtain, through the increase of the diameters for the cells with higher stress concentration, a consequent improvements of the mechanical properties and energy absorption. The process takes as input the generated 3D databases of the stress. As primary hypothesis, it is imposed that the final deformation, so also the output strain levels, is the same:

$$\delta = \delta_0 \leftrightarrow \varepsilon = \varepsilon_0 \quad (4.1)$$

This imposition arises from the type of constraint and load conditions imposed, since on the upper surface of each specimen a displacement equal to -2 mm along Z was inserted. From beam theory, the displacement is defined as:

$$\delta = \frac{C_1 \cdot F \cdot l^3}{12 \cdot E_s \cdot I} \quad (4.2)$$

The force reaction that is obtained, relative to that given imposed displacement, can be rewritten as a function of stress:

$$F = \frac{\sigma_{VM} \cdot t^2 \cdot \pi}{4} \quad (4.3)$$

$$F_0 = \frac{\sigma_{VM_0} \cdot t_0^2 \cdot \pi}{4} \quad (4.4)$$

This definition is central and the input, in the form of a 3D database, can be introduced into the cycle. The primary unknown quantity to be determined is the thickness  $t$ , which will be the focus of the optimization and redistribution of the stress field. It is necessary to define the relationship between the forces obtained pre and post-optimization:

$$F = F_0 \cdot \left( \frac{\rho_R}{\rho_{R0}} \right) \quad (4.5)$$

This formula needs the introduction of the relative density ratio, strictly dependent on the inverse of the aspect ratio (AR) and on the topology of the specimen (parameters A and B), as described in [11] it is defined as:

$$\rho_R = A \cdot \left( \frac{t}{l} \right)^2 + B \cdot \left( \frac{t}{l} \right)^3 \quad (4.6)$$

In order to obtain the parameters A and B, the MATLAB's function "lsqnonlin" has been used and the relative values are represented in the table below:

	A	B
<b>BCC</b>	5.4424	-4.9020
<b>BCCZ</b>	6.2274	-6.1502
<b>FCC</b>	4.4434	-3.9141
<b>FCCZ</b>	5.2295	-5.44177
<b>FBCC</b>	9.8981	-12.8319
<b>FBCCZ</b>	10.6694	-14.3042

Table 4.1: A and B values for relative density based on topology.

Starting with an initial diameter of:

$$t_0 = D_0 = 0.37mm \quad (4.7)$$

With an aspect ratio equivalent to:

$$AR_0 = \frac{L_0}{t_0} = \frac{3mm}{0.37mm} = 8.1 \quad (4.8)$$

Substituting the above equations, the ideal diameter for the struts (in which the voltage peaks are present) is calculated:

$$t = \sqrt{\left(\frac{\sigma_{VM}}{\sigma_{VM0}}\right) \cdot t_0^2 \cdot \left(\frac{\rho_R}{\rho_{R0}}\right)} \quad (4.9)$$

Since  $\sigma_{VM0}$  will always be smaller than  $\sigma_{VM}$ , as it will be purposely chosen as a threshold and will take on smaller values in order to cancel out stress peaks, and having defined the relative density via the parameters A and B (listed in the previous paragraphs), it follows that the two ratios (stress and density) are always multiplicative factors greater than one. This implies that downstream of the optimization process  $t$  (final) will always be greater than  $t_0$ , so there will only be thicknesses greater than 0.37 (diameter). Note the section A of the specimens, which remains the same, by means of the relationship between the forces the vector F is obtained, on which the stress field depends. Through integration, the definition of the volumetric and specific energy absorption is given by:

$$\sigma = \frac{F}{A} \quad (4.10)$$

$$VEA = \int \sigma d\varepsilon \quad (4.11)$$

$$SEA = \frac{VEA \cdot V}{m} = \frac{VEA}{\rho \cdot \rho_r} \quad (4.12)$$

Likewise it is possible to calculate the specific energy absorption from the definition of EA:

$$EA = VEA \cdot V \quad (4.13)$$

$$SEA = \frac{EA}{m} \quad (4.14)$$

Note the relation between the forces and substituting the relative density and the expression in which the Von-Mises stresses appear, the thickness is calculated.

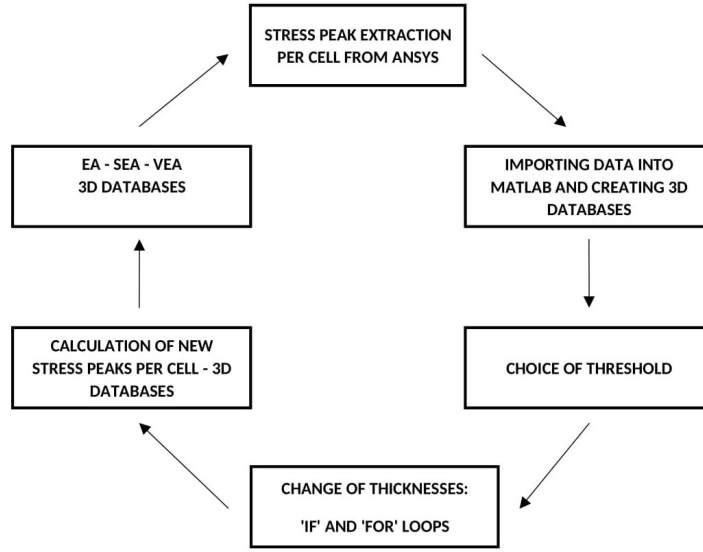


Figure 4.4: Workflow of the process in Matlab.

What is done in Matlab is to implement a cycle 'if' and a cycle 'for' consecutively. If the stress for a given cell exceeds a threshold value the code changes the thickness, from  $t_0$  to  $t$ , using the relation found. To determine an optimum thickness, it is necessary to introduce controls on the critical aspect ratios, which determine the maximum diameters in relation to the lengths of each strut. For this process no limit has been inserted inside the process, in order to make the homogenization of the stress field more performing, so this initial approach is purely theoretical. At each cycle the relative density is recalculated so that different values of VEA and SEA will be recorded and the whole process is well defined in the workflow shown below:

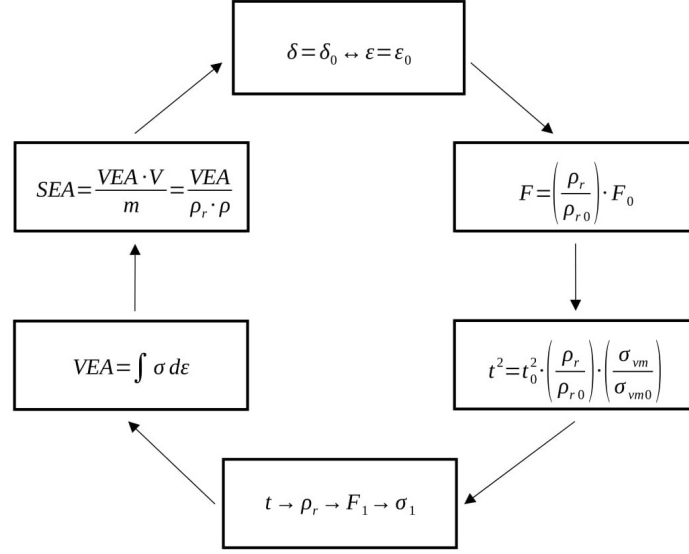


Figure 4.5: Workflow of the process in Matlab - implemented formulas.

### 4.3.2 Second process

Another structural optimisation approach can be performed, taking into account a different formulation for the determination of the thicknesses, which is widely discussed in [48] and it's assumed the load equilibrium that leads to a straightforward relationship between the stress state and strut thicknesses:

$$F = F_0 \quad (4.15)$$

$$t = \sqrt{\left(\frac{\sigma_{VM}}{\sigma_{VM0}}\right) \cdot t_0^2} \quad (4.16)$$

In both cases, the implemented Matlab codes generate a new assignment of thicknesses, which are larger than the starting diameter. The methods could therefore be advantageous to design graded density distribution of lattices in additive manufacturing, leading to advanced properties related to structural strength and energy. The collapse of structure always started from least dense layer to the denser layers, in contrast, samples with uniform density showed abrupt shear failure with diagonal cracking across the whole structure. Furthermore, density graded lattices showed a better energy absorption behavior. This consideration will be established in the next sections and find a perfect correspondence in literature [64].

## 4.4 Implementation of optimization processes: results

Once the maximum stress value per cell was obtained, the average within the specimen (consisting of 1000 cells) was calculated and three different cases are examined:

- threshold at 25% above the average;
- threshold at the minimum value;
- threshold at the average.

Whenever the stress (of an individual cell) exceeds the 'threshold' value, its thickness is changed so that the post-optimization stress value (relative to that same cell) will be exactly at the value selected as the marker. On the basis of this consideration, the three thresholds were chosen as limit values in the case of the 25% and minimum and an intermediate one in the case of choosing the mean value. The first two represent extreme cases in that hardly any cell will exceed 25% of the mean value, so only a few thicknesses will be changed. While for the second every one will be replaced, as all cells have an internal stress value greater than the minimum, so there will be a large increase in mass. The third corresponds to a mid-case, in which there is a trade-off between an increase in weight and an improvement in mechanical and energy performance. Similarly to the stress distribution, there is a reallocation of the value (both for SEA and for VEA). For each of the six configurations, the new values (per cell) of SEA and VEA have been extracted, but in the next sections they will only be reported for certain cases and configurations.

### 4.4.1 Threshold equal to 25% above the mean value

Once the process has been carried out, the diameters assigned to each cell can be extracted for each of the ten specimen planes. In this discussion, a threshold for stress greater than 25% of the mean value is considered. The analysis is carried out for both optimization processes (Process 1 and Process 2). The representations refer to a reference system (for the extraction of the 2D planes) shown in [4.6](#):



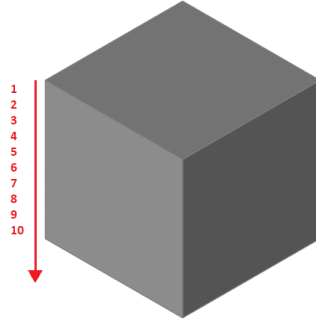


Figure 4.6: Planes numbering system.

Similarly to the stress distribution, there is a recalculation of thicknesses, whereby diameters are only increased for cells with peak stresses. For the assumed threshold, the range of variation of the diameters is affected by a reduced number of cells and there are different minimum and maximum peak values for the two processes:

	t (min) - [mm]	t (max) - [mm]
<b>BCC - Process 1</b>	0.3700	0.9084
<b>BCC - Process 2</b>	0.3700	0.4091
<b>BCCZ - Process 1</b>	0.3700	0.9248
<b>BCCZ- Process 2</b>	0.3700	0.4157
<b>FCC- Process 1</b>	0.3700	0.7184
<b>FCC- Process 2</b>	0.3700	0.3932
<b>FCCZ - Process 1</b>	0.3700	0.8446
<b>FCCZ - Process 2</b>	0.3700	0.4028
<b>FBCC - Process 1</b>	0.3700	0.5873
<b>FBCC - Process 2</b>	0.3700	0.3840
<b>FBCCZ - Process 1</b>	0.3700	0.4138
<b>FBCCZ - Process 2</b>	0.3700	0.3727

Table 4.2: Maximum and minimum thicknesses for a threshold of 25%.

As expected, this variation generates a different stress field, which is more uniform and well distributed, generating higher levels of VEA and SEA. In the tables 4.3, 4.4 and 4.5, it is possible to see the variations in terms of mass (indicative of the major diameters), SEA and VEA in the three different cases:

- 1 indicates the values for uniform specimens (same diameter for each strut);
- 2 indicates the values for the graded samples, for which the first optimization process

has been implemented;

- 3 indicates the values for the graded samples, for which the second optimization process has been implemented [48].

	m1 [g]	m2 [g]	m3 [g]
<b>BCC</b>	5.9889	6.3532	6.0138
<b>BCCZ</b>	7.0349	7.5410	7.0738
<b>FCC</b>	5.3789	5.5954	5.3929
<b>FCCZ</b>	6.4249	6.4908	6.4295
<b>FBCC</b>	11.3680	11.4313	11.3720
<b>FBCCZ</b>	12.4140	12.4291	12.4149

Table 4.3: Masses for the uniform, graded by process 1 and 2 samples, with a threshold equal to the 25%.

	SEA 1 [mJ/g]	SEA 2 [mJ/g]	SEA 3 [mJ/g]
<b>BCC</b>	113.9907	123.2936	122.1065
<b>BCCZ</b>	477.0255	521.3782	510.4012
<b>FCC</b>	356.1905	374.0446	381.4079
<b>FCCZ</b>	663.8578	674.0782	717.1365
<b>FBCC</b>	258.3844	259.9165	269.9143
<b>FBCCZ</b>	438.7231	439.1802	442.7915

Table 4.4: SEA for the uniform, graded by process 1 and 2 samples, with a threshold equal to the 25%.

	VEA 1 [mJ/mm <sup>3</sup> ]	VEA 2 [mJ/mm <sup>3</sup> ]	VEA 3 [mJ/mm <sup>3</sup> ]
<b>BCC</b>	0.0253	0.0290	0.0272
<b>BCCZ</b>	0.1243	0.1456	0.1337
<b>FCC</b>	0.0710	0.0775	0.0762
<b>FCCZ</b>	0.1580	0.1620	0.1723
<b>FBCC</b>	0.1088	0.1100	0.1137
<b>FBCCZ</b>	0.2017	0.2022	0.2036

Table 4.5: VEA for the uniform, graded by process 1 and 2 samples, with a threshold equal to the 25%.

The percentage gain in terms of energy is higher for the second formulation (index 2 - Process 1), while obtaining values very similar to the optimization implemented with the third case

(Process 2). This is clear through an analysis of the following Tables, where the percentages of interest and explanatory of the levels of SEA and VEA obtained:

	SEA - Process 1	SEA - Process 2	VEA - Process 1	VEA - Process 2
<b>BCC</b>	+8.1611%	+7.1197%	+14.6250%	+7.5099%
<b>BCCZ</b>	+9.2978%	+7.0102%	+17.1360%	+7.6109%
<b>FCC</b>	+5.0125%	+7.0798%	+9.1549%	+7.3239%
<b>FCCZ</b>	+1.5395%	+8.0490%	+ 2.5316%	+9.1041%
<b>FBCC</b>	+0.5929%	+4.4623%	+1.1029%	+ 4.5037%
<b>FBCCZ</b>	+0.1041%	+0.9273%	+0.2478%	0.9419%

*Table 4.6: Percentages of increments of SEA e VEA, threshold equal to the 25%.*

Mass	Process 1	Process 2
<b>BCC</b>	+6.0829%	+0.4157%
<b>BCCZ</b>	+ 7.1941%	+0.5529%
<b>FCC</b>	+4.0250%	+0.2602%
<b>FCCZ</b>	+1.0257%	+ 0.0715%
<b>FBCC</b>	+0.5568%	+0.0351%
<b>FBCCZ</b>	+0.1216%	+0.0072%

*Table 4.7: Percentages of increments of the mass, threshold equal to the 25%.*

The Process 1 provides the highest percentages of increase for BCCZ topologies, while Process 2 for FCCZ topologies. The reallocation of the thicknesses results closely connected to the levels of stress recorded, for which it is advantageous in topologies in which the field of stress presents high peaks or strong inhomogeneities. For the BCCZ configurations there are high increases in the VEA levels and moderate ones for SEA. The optimization process leads to remarkable improvements also for the FCC and FCCZ specimens, but only in terms of VEA, since for SEA, the mass increases due to the larger diameters, generate higher percentages for Process 1. Both the approach are not convenient for FBCC and FBCCZ topologies, as both SEA and VEA percentages are very close to 0%. Analysing the results separately, the highest values are obtained for the BCCZ specimen for Process 1, which shows an increase of 9.29% for SEA and 17.14% for VEA, with an increase in mass of 6.08%. For Process 2, the best result refers to the FCCZ specimen, which presents +8.05% for SEA and +9.10% for VEA, showing an increase in mass of only 0.07% compared to the uniform specimen.

#### 4.4.2 Threshold equal to the minimum stress value

The threshold selected in the previous paragraph does not make the optimization process of considerable interest, as it turns out to be too strict a limit and the variations will be marginal. On the basis of these considerations, the threshold is changed from a too stringent limit to a minimum one. In this case a threshold value equal to the absolute minimum recorded (for the stress) is set, so each stress value (for each of the cells) falls within the optimization process. This is equivalent to optimizing the thickness of each individual cell. The analysis was carried out for both optimisation processes (Process 1 and Process 2). According to a reference system (for the extraction of the 2D planes) starting from the surface at the bottom as the previous one, for each of the six configurations, the diameters are extrapolated in 2D databases, whose minimum and maximum values are:

	<b>t (min) - [mm]</b>	<b>t (max) - [mm]</b>
<b>BCC - Process 1</b>	1.0144	2.9928
<b>BCC - Process 2</b>	0.4183	1.0952
<b>BCCZ - Process 1</b>	0.5038	2.2981
<b>BCCZ- Process 2</b>	0.3796	0.7027
<b>FCC- Process 1</b>	1.4051	2.6686
<b>FCC- Process 2</b>	0.4558	0.7509
<b>FCCZ - Process 1</b>	0.3713	1.6115
<b>FCCZ - Process 2</b>	0.3701	0.5202
<b>FBCC - Process 1</b>	1.1296	1.7025
<b>FBCC - Process 2</b>	0.4540	0.6597
<b>FBCCZ - Process 1</b>	0.4872	1.4390
<b>FBCCZ - Process 2</b>	0.3822	0.5658

*Table 4.8: Maximum and minimum thicknesses for the lower threshold.*

The variation of the diameters of the struts (for each cell) generates a more uniform stress field, but at the same time gains in mass (indicative of the major diameters). Of considerable interest is to examine the trends of relative densities, SEA and VEA in the three different cases.

	m1 [g]	m2 [g]	m3 [g]
<b>BCC</b>	5.9889	43.6817	14.1184
<b>BCCZ</b>	7.0349	34.0324	10.5565
<b>FCC</b>	5.3789	33.2399	9.1180
<b>FCCZ</b>	6.4249	16.9395	7.4089
<b>FBCC</b>	11.3680	45.3133	17.4813
<b>FBCCZ</b>	12.4140	40.2337	16.8180

Table 4.9: Masses for the uniform, graded by process 1 and 2 samples, with the minimum threshold.

	SEA 1 [mJ/g]	SEA 2 [mJ/g]	SEA 3 [mJ/g]
<b>BCC</b>	113.9907	152.0814	271.2301
<b>BCCZ</b>	477.0255	1017.6157	723.6071
<b>FCC</b>	356.1905	761.7490	607.7912
<b>FCCZ</b>	663.8578	1329.9017	768.8196
<b>FBCC</b>	258.3844	437.4180	398.4133
<b>FBCCZ</b>	438.7231	772.8880	896.6283

Table 4.10: SEA for the uniform, graded by process 1 and 2 samples, with the minimum threshold.

	VEA 1 [mJ/mm <sup>3</sup> ]	VEA 2 [mJ/mm <sup>3</sup> ]	VEA 3 [mJ/mm <sup>3</sup> ]
<b>BCC</b>	0.0253	0.2460	0.1420
<b>BCCZ</b>	0.1243	1.2826	0.2829
<b>FCC</b>	0.0710	0.9378	0.2053
<b>FCCZ</b>	0.1580	0.8344	0.2110
<b>FBCC</b>	0.1088	1.1517	0.3715
<b>FBCCZ</b>	0.2017	0.7341	0.2572

Table 4.11: VEA for the uniform, graded by process 1 and 2 samples, with the minimum threshold.

Analogous to previous results, the percentage gain in terms of energy is higher for Process 1 (index 2), while obtaining values quite different to the optimization implemented with the second iterative method (index 3). The percentage deviations between process 1 and process 2 are justified by the fact that for the first one, the ratio of relative densities (actual divided by initial) appears in the diameter optimization formula, which is a positive multiplicative term, greater than one, leading to much greater thicknesses. This induces considerable increases in mass and higher VEA values as the model will have a higher stress resistance (higher force reaction).

The percentages are summarized in the Tables below:

	SEA - Process 1	SEA - Process 2	VEA - Process 1	VEA - Process 2
<b>BCC</b>	+33.4109%	+137.9445%	+872.3353%	+461.2638%
<b>BCCZ</b>	+113.3232%	+51.6935%	+931.8607%	+127.5973%
<b>FCC</b>	+113.8633%	+70.6903%	+1220.8014%	+189.1504%
<b>FCCZ</b>	+100.3232%	+ 15.8098%	+428.10558%	+33.5483%
<b>FBCC</b>	+69.2844%	+54.1908%	+958.5538%	+241.4554%
<b>FBCCZ</b>	+76.1600%	+104.3787%	+263.9604%	+27.5110%

*Table 4.12: Percentages of increments of SEA and VEA, minimum threshold.*

Mass	Process 1	Process 2
<b>BCC</b>	+ 629.3709%	+135.7422%
<b>BCCZ</b>	+ 383.7646%	+50.0554%
<b>FCC</b>	+517.9633%	+ 69.5183%
<b>FCCZ</b>	+163.6575%	+15.3158%
<b>FBCC</b>	+298.6037%	+53.7732%
<b>FBCCZ</b>	+224.0970%	+35.4764%

*Table 4.13: Percentages of increments of the mass, minimum threshold.*

This case is the inverse extreme of the previous one, the mass has increased considerably due to the strong variations of the diameters. There are high percentages of growth in terms of VEA, due to the homogenization of the stress field. Analysing the results separately, the highest values are obtained for the BCCZ and FCC specimens for Process 1, which shows an increase of 113.32% and 113.86% for SEA, while for VEA the best candidates are FCC and FBCC. Regarding Process 2, the best results are obtained for the BCC and FBCCZ specimens, which presents 137.94% and 104.37% for SEA. The percentages obtained are beyond manufacturing practicability, as the treatment is purely theoretical. It has been deliberately chosen not to include a control within the cycle, so unfeasible diameters have been considered in terms of maximum Aspect Ratio. Looking at the table containing the maximum thicknesses and taking into account that each struts has a length of 3 mm, the realisation would give in output an almost homogenised cell (full solid). Producing these samples would imply a homogenised case, which explains the high percentages of increments.

#### 4.4.3 Threshold equal to the average

The previously envisaged solution does not take into account limiting and critical values for the aspect ratio. Given the maximum diameters obtained and shown in the tables above, it can be seen that the maximum diameter exceeds the critical values. Assuming a length of 3 mm for each strut, the diameters selected are not feasible. In this section the threshold has been reset to a value equal to the average. Once the process has been carried out, the diameters assigned to each cell can be extracted for each of the ten specimen planes. Similarly to the stress distribution, there is a reallocation of thicknesses, whereby there are only increased for cells with peak stresses. For each of the six configurations, the diameters are shown in the tables below.:

	<b>t (min) - [mm]</b>	<b>t (max) - [mm]</b>
<b>BCC - Process 1</b>	0.3700	1.3929
<b>BCC - Process 2</b>	0.3700	0.4573
<b>BCCZ - Process 1</b>	0.3700	1.3474
<b>BCCZ - Process 2</b>	0.3700	0.4648
<b>FCC - Process 1</b>	0.3700	1.2559
<b>FCC - Process 2</b>	0.3700	0.4397
<b>FCCZ - Process 1</b>	0.3700	1.1869
<b>FCCZ - Process 2</b>	0.3700	0.4504
<b>FBCC - Process 1</b>	0.3700	0.8702
<b>FBCC - Process 2</b>	0.3700	0.4293
<b>FBCCZ - Process 1</b>	0.3700	0.7651
<b>FBCCZ - Process 2</b>	0.3700	0.4167

*Table 4.14: Maximum and minimum thicknesses for a threshold equal to the average value of the stress.*

For this discussion, it has been decided not to report the 3D database for the reassigned thicknesses, as it will be shown in Chapter 5 (where all checks on maximum thicknesses will be placed). Downstream of the variation of thicknesses, the stress field obtained was more homogeneous. The new stress redistribution corresponds for both Process 1 and Process 2, as the logic behind the optimization codes is the same, what varies is only the calculation of the thicknesses (which affects the post-optimization energy values). Starting from the same uniform structure (same stress field) and imposing the same threshold, the code automatically replaces the thicknesses and results in a stress equal to the threshold (if within each individual

strut the stress value is greater). This implies an equality of the stress field, even downstream of the new distribution of diameters, which although almost comparable, are an obvious approximation induced by the code in calculating the stress per elementary cell. In terms of physical, mechanical and energy characteristics, reference is made to the tables below. The mass, having increased the diameters, will be greater, but the volume of the whole specimen will remain unchanged.

	<b>m1 [g]</b>	<b>m2 [g]</b>	<b>m3 [g]</b>
<b>BCC</b>	5.9889	10.3848	6.3072
<b>BCCZ</b>	7.0349	10.8773	7.34994
<b>FCC</b>	5.3789	8.6783	5.6071
<b>FCCZ</b>	6.4249	7.976	6.5531
<b>FBCC</b>	11.3680	13.6584	11.6061
<b>FBCCZ</b>	12.4140	15.2681	12.7188

*Table 4.15: Masses for the uniform, graded by process 1 and 2 samples, with a threshold equal to the average value of the stress.*

	<b>SEA 1 [mJ/g]</b>	<b>SEA 2 [mJ/g]</b>	<b>SEA 3 [mJ/g]</b>
<b>BCC</b>	113.9907	193.0640	126.2600
<b>BCCZ</b>	477.0255	738.8722	537.3131
<b>FCC</b>	356.1905	571.4881	386.1972
<b>FCCZ</b>	663.8578	839.6639	728.5729
<b>FBCC</b>	258.3844	305.2790	272.0931
<b>FBCCZ</b>	438.7231	523.3687	459.6881

*Table 4.16: SEA for the uniform, graded by process 1 and 2 samples, with a threshold equal to the average value of the stress.*



	VEA 1 [ $mJ/mm^3$ ]	VEA 2 [ $mJ/mm^3$ ]	VEA 3 [ $mJ/mm^3$ ]
<b>BCC</b>	0.0253	0.0743	0.0295
<b>BCCZ</b>	0.1243	0.2977	0.1463
<b>FCC</b>	0.0710	0.1837	0.0802
<b>FCCZ</b>	0.1580	0.2480	0.1768
<b>FBCC</b>	0.1088	0.1544	0.1170
<b>FBCCZ</b>	0.2017	0.2960	0.2165

Table 4.17: VEA for the uniform, graded by process 1 and 2 samples, with a threshold equal to the average value of the stress.

In purely energetic terms, there are increases for both processes. Process 1 shows the highest percentages in both specific and volumetric terms:

	SEA - Process 1	SEA - Process 2	VEA - Process 1	VEA - Process 2
<b>BCC</b>	+69.3681%	+10.7634%	+193.6863%	+16.6016%
<b>BCCZ</b>	+54.8927%	+12.6380%	+139.5017%	+17.6993%
<b>FCC</b>	+60.4451%	+8.4246%	+158.7342%	+12.9587%
<b>FCCZ</b>	+26.4821%	+9.74814%	+ 57.093%	+11.9894%
<b>FBCC</b>	+18.1490%	+5.3050%	+ 41.9122%	+7.536%
<b>FBCCZ</b>	+19.2949%	+4.7780%	+46.7531%	+7.3378%

Table 4.18: Percentages of increments of SEA e VEA, threshold equal to the average value of the stress.

Mass	Process 1	Process 2
<b>BCC</b>	+73.4014%	+5.3148%
<b>BCCZ</b>	+54.6192%	+4.4782%
<b>FCC</b>	+61.3497%	+4.2425%
<b>FCCZ</b>	+24.1426%	+1.9954%
<b>FBCC</b>	+20.1484%	+2.0945%
<b>FBCCZ</b>	+22.9912%	+2.4553%

Table 4.19: Percentages of increments of the mass, threshold equal to the average value of the stress.

The BCC and FCC configurations are the most promising for Process 1. For Optimization Process 2, BCCZ sample leads to an excellent energy value, without changing the final weight of

the structure too much.

This suggests that for future, more in-depth analyses, these four configurations are of interest. In wishing to carry out an eventual experimental campaign (Chapter 6), however, it is necessary to overcome the assumed approximations, which reside in printability limitations, but at the same time in constraints regarding the definition of lattice structures themselves. So the next Chapter proceeds in considering these aspects.

## 4.5 Energy extraction in table format

The 2D visualization, performed above for the stresses (pre-process) and for the new diameters assigned to each cell, can also be carried out for the energy values (SEA and VEA), in a similar way. In this case, known the new stress values (assigned at the end of the process of optimization), can be calculated the values of the energy absorption through a different formula (using in matlab the function 'trapz'). Once the value of the stress for each of the cells is known, the force can easily be derived (the value of the cross-section A is known):

$$F = \sigma \cdot A \quad (4.17)$$

Once the value of the force, for each cell, has been obtained, introducing the displacement d equal to 2 mm, it is possible to obtain the value of the energy absorption, from which SEA and VEA (known mass m and volume V) are derived:

$$EA = F \cdot d \quad (4.18)$$

$$SEA = \frac{EA}{m} \quad (4.19)$$

$$VEA = \frac{EA}{V} \quad (4.20)$$

It is necessary to use this formula because, at the end of the process, a new stress value is obtained for each of the cells (the final maximum value to be reassigned) and not a vector containing the 'load history' to be integrated.

## Chapter 5

### Limit imposed for 3D printing (SLM)

Selective laser melting (SLM) is an AM process that enables the manufacture of space filling lattice structures with great load bearing efficiency and personalisable stiffness. However, to commercialise SLM lattice structures it is necessary to define the manufacturability of lattice samples, because the minimum thickness is limited by the parameters and machine settings, while the dimensional accuracy is controlled by the powder size and scan strategy. In this specific case, a minimum print thickness of 0.33 mm is recommended. By implementing a process in which it is only possible to obtain thicknesses greater than the initial diameter of 0.37 mm so the minimum limits are automatically respected. Based on the work of Ashby and Gibson, a clear definition of lattice structure is given. It is distinguished from a solid (filled with material) by the presence of struts oriented at different angles, which must comply with precise dimensions. From the definition, an upper limit is established, which requires that any internal thickness does not exceed a limit equal to 30% of the density. In accordance with this imposition, a different upper limit is configured for each of the six topologies:

	<b>t (max) - [mm]</b>
<b>BCC</b>	0.8900
<b>BCCZ</b>	1.0100
<b>FCC</b>	1.1400
<b>FCCZ</b>	0.9600
<b>FBCC</b>	0.7700
<b>FBCCZ</b>	0.7500

*Table 5.1: Upper limit of diameters of each unit cell - control to insert for the optimization processes.*

By imposing this limit, the Matlab code was modified with a check ('if' loop) and, for the three imposed threshold cases, the new results are researched.

## 5.1 Results for the three cases

### 5.1.1 Threshold equal to 25% above the mean value

For the first threshold case of 25% of the mean value, maximum diameters were found (Table 5.2). Of interest are the new increases for both SEA and VEA, which establish different optimum configurations.

	t (min) - [mm]	t (max) - [mm]
<b>BCC - Process 1</b>	0.3700	0.8900
<b>BCC - Process 2</b>	0.3700	0.4091
<b>BCCZ - Process 1</b>	0.3700	0.9248
<b>BCCZ - Process 2</b>	0.3700	0.4158
<b>FCC - Process 1</b>	0.3700	0.7184
<b>FCC - Process 2</b>	0.3700	0.3933
<b>FCCZ - Process 1</b>	0.3700	0.8446
<b>FCCZ - Process 2</b>	0.3700	0.4028
<b>FBCC - Process 1</b>	0.3700	0.5873
<b>FBCC - Process 2</b>	0.3700	0.3840
<b>FBCCZ - Process 1</b>	0.3700	0.4138
<b>FBCCZ - Process 2</b>	0.3700	0.3727

*Table 5.2: Maximum and minimum thicknesses for a threshold of 25%, with the upper limit.*

For both Processes, all percentage increase values are shown in the tables below, which are representative and summarized for each of the six configurations analyzed.

	<b>m1 [g]</b>	<b>m2 [g]</b>	<b>m3 [g]</b>
<b>BCC</b>	5.9889	6.3508	6.0138
<b>BCCZ</b>	7.0349	7.5357	7.0738
<b>FCC</b>	5.3789	5.5954	5.3929
<b>FCCZ</b>	6.4249	6.4908	6.4295
<b>FBCC</b>	11.3680	11.4313	11.3720
<b>FBCCZ</b>	12.4140	12.4291	12.4149

*Table 5.3: Masses for the uniform, graded by process 1 and 2 samples, with a threshold equal to the 25% considering the upper limit.*

	<b>SEA 1 [mJ/g]</b>	<b>SEA 2 [mJ/g]</b>	<b>SEA 3 [mJ/g]</b>
<b>BCC</b>	113.9907	123.2007	122.1065
<b>BCCZ</b>	477.0255	520.7101	510.4012
<b>FCC</b>	356.1905	374.0446	381.4079
<b>FCCZ</b>	663.8578	674.0782	717.1365
<b>FBCC</b>	258.3844	259.9165	269.9143
<b>FBCCZ</b>	438.7231	439.1802	442.7915

*Table 5.4: SEA for the uniform, graded by process 1 and 2 samples, with a threshold equal to the 25% considering the upper limit.*

	<b>VEA 1 [mJ/mm<sup>3</sup>]</b>	<b>VEA 2 [mJ/mm<sup>3</sup>]</b>	<b>VEA 3 [mJ/mm<sup>3</sup>]</b>
<b>BCC</b>	0.0253	0.0290	0.0272
<b>BCCZ</b>	0.1243	0.1453	0.1337
<b>FCC</b>	0.0710	0.0775	0.0762
<b>FCCZ</b>	0.1580	0.1620	0.1723
<b>FBCC</b>	0.1088	0.1100	0.1137
<b>FBCCZ</b>	0.2017	0.2022	0.2036

*Table 5.5: VEA for the uniform, graded by process 1 and 2 samples, with a threshold equal to the 25% considering the upper limit.*

	SEA - Process 1	SEA - Process 2	VEA - Process 1	VEA - Process 2
<b>BCC</b>	+8.0796%	+7.1197%	+14.6250%	+7.5099%
<b>BCCZ</b>	+9.1577%	+7.0102%	+16.8950%	+7.5623%
<b>FCC</b>	+5.0125%	+7.0798%	+9.1549%	+7.3239%
<b>FCCZ</b>	+1.5395%	+8.0490%	+2.5316%	+9.0506%
<b>FBCC</b>	+0.5929%	+4.4623%	+1.1029%	+4.5030%
<b>FBCCZ</b>	+0.1041%	+0.9273%	+0.2478%	+0.9419%

*Table 5.6: Percentages of increments of SEA and VEA, threshold equal to the 25% and upper limit imposed.*

Mass	Process 1	Process 2
<b>BCC</b>	+6.0428%	+0.4157%
<b>BCCZ</b>	+7.1188%	+0.5529%
<b>FCC</b>	+4.0250%	+0.2602%
<b>FCCZ</b>	+1.0257%	+0.0715%
<b>FBCC</b>	+0.5568%	+0.0351%
<b>FBCCZ</b>	+0.1216%	+0.0072%

*Table 5.7: Percentages of increments of the mass, threshold equal to the 25% and upper limit imposed.*

Similarly, such a low threshold does not generate much variation and improvement. The BCCZ configuration turns out to be the best for Process 1 (for both SEA and VEA), while for Process 2 the FCCZ sample shows an increase of +8.05% for SEA and +9.05% for VEA, being the best selection, also in terms of mass savings.

### 5.1.2 Threshold equal to the minimum stress value

After the imposition of the control within the Matlab code, in the case of a minimum threshold that tends to vary all diameters, generating a uniform stress field, the following maxima and minima for the diameters are obtained:

	<b>t (min) - [mm]</b>	<b>t (max) - [mm]</b>
<b>BCC - Process 1</b>	0.8900	0.8900
<b>BCC - Process 2</b>	0.4183	0.8900
<b>BCCZ - Process 1</b>	0.5038	1.0100
<b>BCCZ - Process 2</b>	0.3796	0.7027
<b>FCC - Process 1</b>	1.1400	1.1400
<b>FCC - Process 2</b>	0.4558	0.7509
<b>FCCZ - Process 1</b>	0.3713	0.9600
<b>FCCZ - Process 2</b>	0.3701	0.5202
<b>FBCC - Process 1</b>	0.7700	0.7700
<b>FBCC - Process 2</b>	0.4740	0.6597
<b>FBCCZ - Process 1</b>	0.4872	0.7500
<b>FBCCZ - Process 2</b>	0.3822	0.5658

*Table 5.8: Maximum and minimum thicknesses for the minimum threshold selected, with the upper limit.*

The mass and energy increments are delineated in the tables below (for each of the six configurations). Each cell has a higher stress than the threshold and all diameters have been increased. This generates a large improvement in mass, which is not reasonable for most light-weight structure applications. In this case, it can be seen, from the summary tables, that, for Process 1, the best choice is BCC configuration, while for Process 2, FCC has the highest increase values in terms of energy.

	<b>m1 [g]</b>	<b>m2 [g]</b>	<b>m3 [g]</b>
<b>BCC</b>	5.9889	17.3380	13.3980
<b>BCCZ</b>	7.0349	16.6610	10.5560
<b>FCC</b>	5.3789	12.8780	9.1180
<b>FCCZ</b>	6.4249	14.7592	7.4089
<b>FBCC</b>	11.3611	27.2173	17.4310
<b>FBCCZ</b>	12.4142	29.2270	16.8110

*Table 5.9: Masses for the uniform, graded by process 1 and 2 samples, with the minimum threshold, considering the upper limit.*

	SEA 1 [mJ/g]	SEA 2 [mJ/g]	SEA 3 [mJ/g]
<b>BCC</b>	113.9907	225.6610	257.2903
<b>BCCZ</b>	477.0255	918.1324	723.6136
<b>FCC</b>	356.1905	708.8409	607.7911
<b>FCCZ</b>	663.8578	1238.0025	768.8019
<b>FBCC</b>	258.3844	454.6209	398.4210
<b>FBCCZ</b>	438.7230	755.6420	596.6204

Table 5.10: SEA for the uniform, graded by process 1 and 2 samples, with the minimum threshold, considering the upper limit.

	VEA 1 [mJ/mm <sup>3</sup> ]	VEA 2 [mJ/mm <sup>3</sup> ]	VEA 3 [mJ/mm <sup>3</sup> ]
<b>BCC</b>	0.0253	0.1198	0.1277
<b>BCCZ</b>	0.1243	0.5666	0.2829
<b>FCC</b>	0.0710	0.3381	0.2053
<b>FCCZ</b>	0.1580	0.6744	0.2116
<b>FBCC</b>	0.1088	0.4583	0.2572
<b>FBCCZ</b>	0.2017	0.8179	0.3715

Table 5.11: VEA for the uniform, graded by process 1 and 2 samples, with the minimum threshold, considering the upper limit.

	SEA - Process 1	SEA - Process 2	VEA - Process 1	VEA - Process 2
<b>BCC</b>	+97.9656%	+125.7209%	+373.5205%	+404.7419%
<b>BCCZ</b>	+92.4692%	+51.6923%	+355.8356%	+127.5933%
<b>FCC</b>	+99.0058%	+70.6327%	+376.2092%	+189.152%
<b>FCCZ</b>	+86.4743%	+15.8018%	+326.5852%	+33.5443%
<b>FBCC</b>	+75.9475%	+54.1981%	+321.2357%	+136.4180%
<b>FBCCZ</b>	+72.2363%	+35.9917%	+305.5611%	+84.1840%

Table 5.12: Percentages of increments of SEA and VEA for the minimum threshold and the upper limit imposed.



Mass	Process 1	Process 2
BCC	+189.5018%	+123.7203%
BCCZ	+136.8446%	+50.0593%
FCC	+139.5922%	+69.5148%
FCCZ	+129.7104%	+15.3152%
FBCC	+139.3735%	+53.3374%
FBCCZ	+135.4321%	+35.4180%

Table 5.13: Percentages of increments of the mass for the minimum threshold and the upper limit imposed.

### 5.1.3 Threshold equal to the mean value

For the last case, optimization and analysis were again carried out using the automatic code. This produced results parallel to those previously seen in the case of an absent upper bound.

	t (min) - [mm]	t (max) - [mm]
BCC - Process 1	0.3700	0.8900
BCC - Process 2	0.3700	0.4573
BCCZ - Process 1	0.3700	1.0100
BCCZ - Process 2	0.3700	0.4648
FCC - Process 1	0.3700	1.1400
FCC - Process 2	0.3700	0.4397
FCCZ - Process 1	0.3700	0.9600
FCCZ - Process 2	0.3700	0.4504
FBCC - Process 1	0.3700	0.7700
FBCC - Process 2	0.3700	0.4293
FBCCZ - Process 1	0.3700	0.7500
FBCCZ - Process 2	0.3700	0.4167

Table 5.14: Maximum and minimum thicknesses for a threshold equal to the average value of the stress, with the upper limit.

For this section, it was chosen to show the 3D database for the new thicknesses, as it falls in the intermediate case of the first threshold (25%) and the second one (minimum value selected as stress control into the if-loop), but only for two of the configurations (BCC1 and BCCZ1), which will be discussed in more detail in the following chapters. In the following paragraphs, the BCC and BCCZ configurations (considering a threshold equal to the mean value) will be

analyzed in detail, as they are the most performing. They will be validated using software and experimentally. Therefore, Appendix [B] shows the new redistribution of thicknesses, based on the limits imposed and considering both Process 1 and 2, for these two configurations. In term of new redistribution of stress, for the same two configurations the results show variations comparing with the previous one, without the upper limit imposed. The new redistribution is highlighted in the Appendix [A], where the 2D grids (extrapolated from the 3D databases) are proposed.

	<b>m1 [g]</b>	<b>m2 [g]</b>	<b>m3 [g]</b>
<b>BCC</b>	5.9889	14.9407	6.3072
<b>BCCZ</b>	7.0349	14.045	7.3499
<b>FCC</b>	5.3789	8.3916	5.6071
<b>FCCZ</b>	6.4249	7.9350	6.5531
<b>FBCC</b>	11.3680	13.6580	11.606
<b>FBCCZ</b>	12.4141	15.2682	12.7194

*Table 5.15: Masses for the uniform, graded by process 1 and 2 samples, with a threshold equal to the average value of the stress, with the upper limit.*

	<b>SEA 1 [mJ/g]</b>	<b>SEA 2 [mJ/g]</b>	<b>SEA 3 [mJ/g]</b>
<b>BCC</b>	113.9907	184.7710	126.2604
<b>BCCZ</b>	477.0255	708.6019	537.3134
<b>FCC</b>	356.1905	549.8301	386.2468
<b>FCCZ</b>	663.8578	833.8903	728.5745
<b>FBCC</b>	258.3844	305.2855	272.0971
<b>FBCCZ</b>	438.7231	523.3746	459.6918

*Table 5.16: SEA for the uniform, graded by process 1 and 2 samples, with a threshold equal to the average value of the stress, with the upper limit.*

	VEA 1 [ $mJ/mm^3$ ]	VEA 2 [ $mJ/mm^3$ ]	VEA 3 [ $mJ/mm^3$ ]
<b>BCC</b>	0.0253	0.0681	0.0295
<b>BCCZ</b>	0.1243	0.2741	0.1463
<b>FCC</b>	0.0712	0.1709	0.0802
<b>FCCZ</b>	0.1580	0.2451	0.1768
<b>FBCC</b>	0.1088	0.1544	0.1170
<b>FBCCZ</b>	0.2017	0.2960	0.2165

Table 5.17: VEA for the uniform, graded by process 1 and 2 samples, with a threshold equal to the average value of the stress, with the upper limit.

	SEA - Process 1	SEA - Process 2	VEA - Process 1	VEA - Process 2
<b>BCC</b>	+62.0911%	+10.7631%	+168.7713%	+16.6012%
<b>BCCZ</b>	+48.5460%	+12.6380%	+120.5102%	+17.6990%
<b>FCC</b>	+54.3633%	+8.4243%	+140.7094%	+12.9581%
<b>FCCZ</b>	+25.6130%	+9.7483%	+55.1275%	+11.8992%
<b>FBCC</b>	+18.1493%	+5.3055%	+41.9122%	+7.5368%
<b>FBCCZ</b>	+19.2940%	+4.7786%	+46.7538%	+7.3376%

Table 5.18: Percentages of increments of SEA and VEA, threshold equal to the average value of the stress, with the upper limit.

Mass	Process 1	Process 2
<b>BCC</b>	+149.4451%	+5.3148%
<b>BCCZ</b>	+99.6409%	+4.4777%
<b>FCC</b>	+56.0105%	+4.2425%
<b>FCCZ</b>	+23.5041%	+1.9954%
<b>FBCC</b>	+20.1481%	+2.0945%
<b>FBCCZ</b>	+22.9912%	+2.4553%

Table 5.19: Percentages of increments of the mass, threshold equal to the average value of the stress, with the upper limit.

By imposing a stress threshold exactly equal to the mean value, it falls into the case where good increases in energy are obtained, but without considerable increases in mass. So it can be seen as a compromise between the two previously discussed. In this case, the best configurations are BCC and BCCZ, for Process 1 and 2 respectively. For the BCC topology, there is a value

of +62.09% for SEA and +168.77% for VEA, leading to a final weight increase of +149.44%. As for the second process, BCCZ is the best with an increment for VEA of +17.69% with a minimum mass increase of +4.48%. For the two configurations of interest, the values per cell of the specific energy absorption is shown for both process 1 (Appendix [C.1]) and 2 (Appendix [C.2]), while in term of VEA, the results of the 2D databases are related to Appendices [D.1] and [D.2]. It is only shown for one half of the specimen (five planes), as they are all symmetrical.

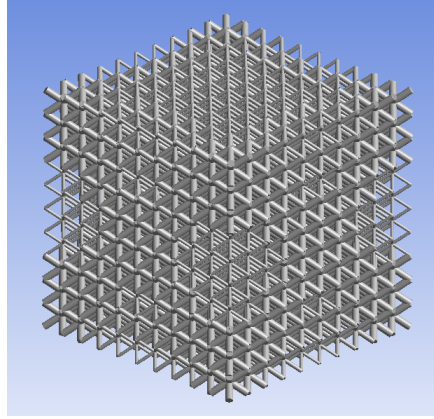
## 5.2 Verification of the Matlab optimization approaches

Through the introduction of an upper limit, the diameters of the struts were modified for the different topologies in order to guarantee conformity for lattice structures. The results obtained through optimization and static analysis using the Matlab code require a validation via Ansys. This is crucial to prove the consistency of the achieved output. In this section, BCC and BCCZ topologies are validated. The choice is based on the best results obtained in terms of specific energy absorption, as it also takes into account the additional costs in terms of increasing the mass of specimens. BCC topology was chosen as sample because it presents the highest values for Process 1, and BCCZ for Process 2. For the sake of completeness, analyses in Ansys Workbench were carried out for both optimization processes:

- BCC topology optimized through Process 1;
- BCC topology optimized through Process 2;
- BCCZ topology optimized through Process 1;
- BCCZ topology optimized through Process 2.

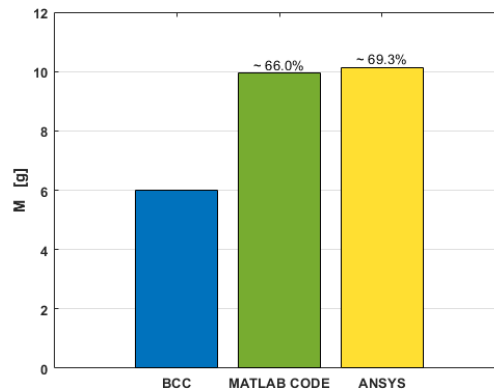
### 5.2.1 Validation for BCC sample graded by Process 1

In relation to the data obtained in the previous paragraph, having selected a threshold (for variation of the thicknesses a stress value) greater than the average, it is of interest to validate the results and the percentages of increase in terms of energy for the most convenient topology BCC. The optimization proposes a set of diameters to be reassigned to the numerical model, for which an analysis performed with Ansys is proposed (for the configuration 10x10x10 cells), with topology concerning single cells of BCC type. The graded geometry obtained by Ansys Workbench is shown in the Figure [5.1](#).



*Figure 5.1: Geometry of the graded sample post optimization - BCC1.*

The comparison is made between the uniform BCC test specimen (10X10X10), the results obtained from the operating process via Matlab code and via a bilinear simulation in Ansys. In the bilinear simulation all the diameters obtained in output from the optimization process have been inserted, keeping boundary conditions and loads unchanged.



*Figure 5.2: Comparison of the masses - BCC1.*

The values obtained with the numerical analysis generate a new redistribution of internal stresses, which will be less inhomogeneous than the starting specimen.

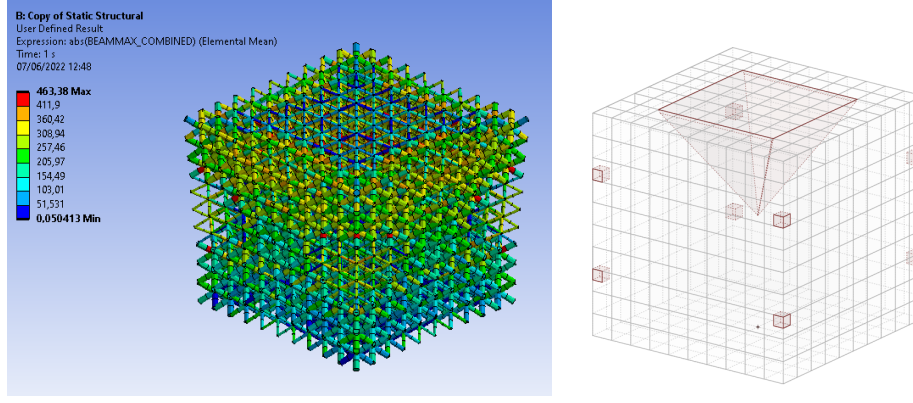


Figure 5.3: Stress field of the graded sample post optimization - BCC1.

In order to obtain the percentages of increase and to be able to make a comparison with the values obtained by means of the Matlab code, an overlaid comparison is necessary, in an histogram form, is proposed. It highlights the increase in maximum voltages obtained in the case of the graded configuration, which translates into different values in terms of energy absorption:

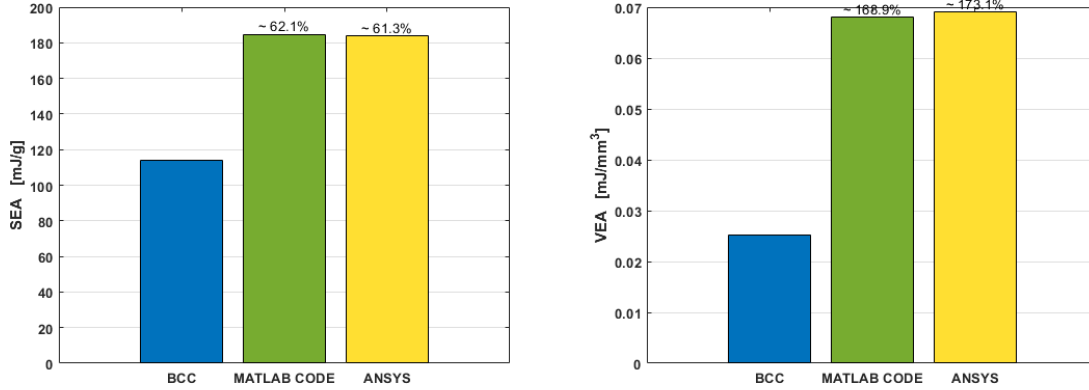
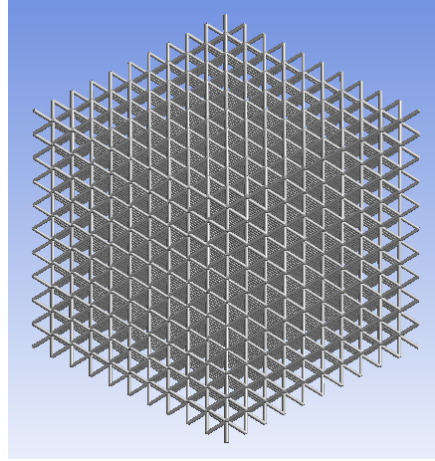


Figure 5.4: Comparison of SEA and VEA - BCC1.

From the proposed histograms, the increase percentages for SEA and VEA are completely comparable, which validates the process of recalculating the energy absorption performed automatically using the Matlab code. As can be seen, for BCC1 configuration, the deviation (in absolute value) among the SEA values calculated via Matlab and Ansys is equal to 0.8%, while for VEA it's possible to appreciate a percentage of absolute difference of 4.2%. Considering the computational costs in time provided by the Matlab code shown in the Section 5.5 (compared to Ansys), this results are fully satisfactory, as the deviations are minimal, but completely acceptable considering the enormous advantage in analysis time.

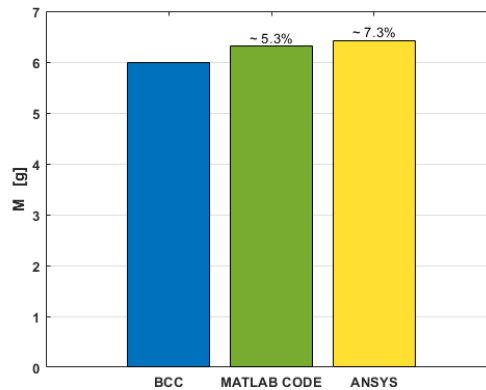
### 5.2.2 Validation for BCC sample graded by Process 2

Whatever is done in the previous section for Process 1 is also performed for Process 2. So the geometry is recreated in the Ansys environment and the analysis is carried out, obtaining the stress field and the specific and volumetric energy absorption levels.



*Figure 5.5: Geometry of the graded sample post optimization - BCC2.*

In this case, a further confrontation is made between the uniform BCC sample (10X10X10), the results obtained from the operating process via Matlab code and via a bilinear simulation in Ansys. In the bilinear simulation all the thicknesses have been inserted, keeping the same boundary conditions and imposed displacement (equal to -2 mm along z-axis).



*Figure 5.6: Comparison of the masses - BCC2.*

As in the previous analysis, the optimized geometry of the sample leads to a new redistribution of the stresses, which show a different internal path:

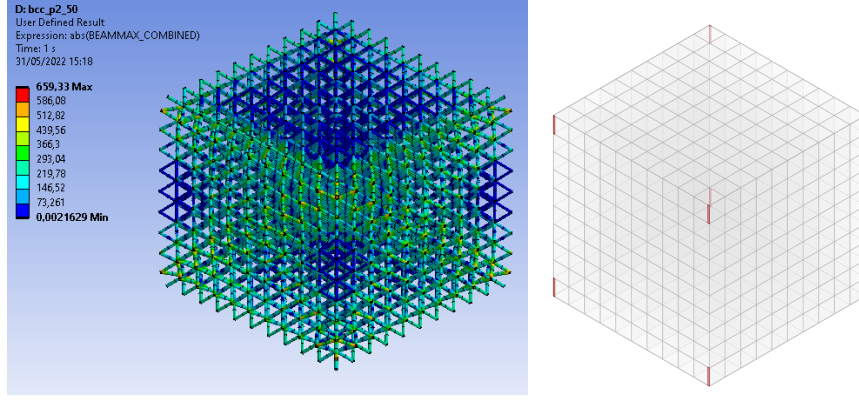


Figure 5.7: Stress field of the graded sample post optimization - BCC2.

The homogenization of the stress field is attained, whereby peaks are at points in the corners, which are also justified by marginal edge effects. The plots 5.8 show the improvements in term of SEA and VEA:

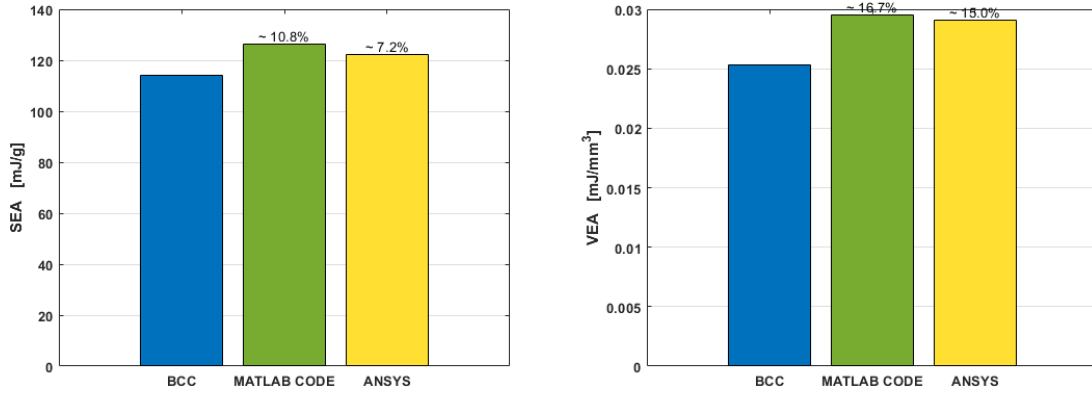


Figure 5.8: Comparison of SEA and VEA - BCC2.

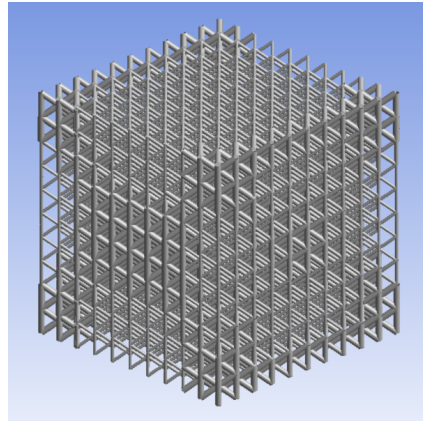
In this case, for specific absorption energy values, the outputs (Matlab - Ansys) differ by 3.6%, and for volumetric values by 6.7%. These percentages are higher than those recorded in the case of the comparison of the BCC1 specimens, meaning that, without the inclusion of the z-struts, the code better predicts the energy properties for the implementation of Process 1 instead of the second one.

### 5.2.3 Validation for BCCZ sample graded by Process 1

The validations performed for the BCC configuration are repeated in the same way for the BCCZ. In this case, an analysis is proposed in terms of mechanical behaviour (stress-strain

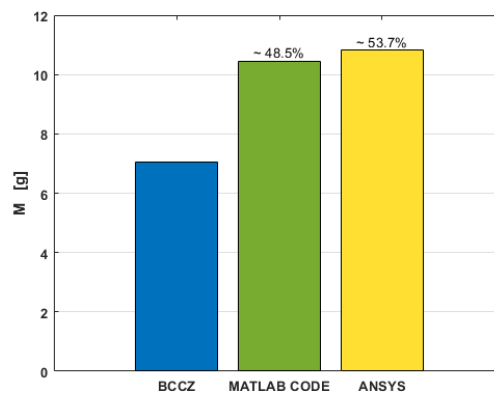


curves), stress field and energy performance. Within the software, the new diameters are noted and the geometry is recreated:



*Figure 5.9: Geometry of the graded sample post optimization - BCCZ1.*

The comparison is made between the uniform BCCZ configuration (10X10X10), the results obtained from the operating process 1 via Matlab code and via a bilinear simulation in Ansys, for which the following percentage changes are recorded:



*Figure 5.10: Comparison of the masses - BCCZ1.*

The values obtained with the numerical analysis generate a new redistribution of internal stresses, which sees a concentration only in the vertical struts belonging to the upper surface:

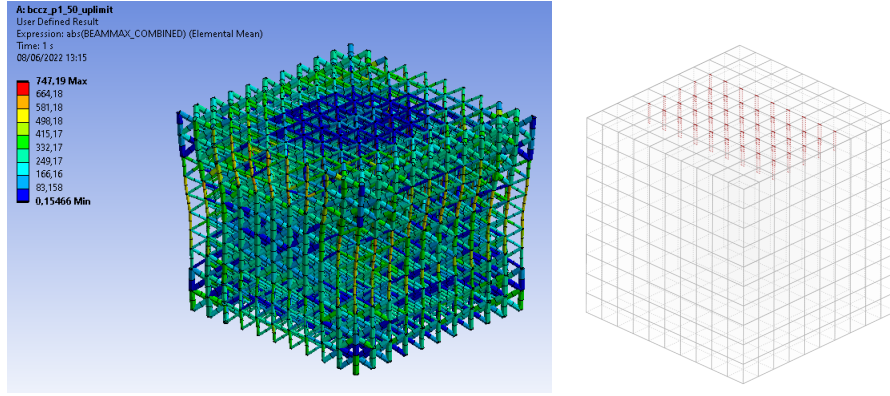


Figure 5.11: Stress field of the graded sample post optimization - BCCZ1.

This qualitative schematization refers to the extrapolation of stress peaks in the sample, obtained in Ansys showing only the struts with stresses above a threshold, whereby it is clearly evident that the peaks are only clustered in the central zone.

In term of SEA and VEA, The overlaid columns highlight the improvement in the case of the graded configuration, which translates into different values:

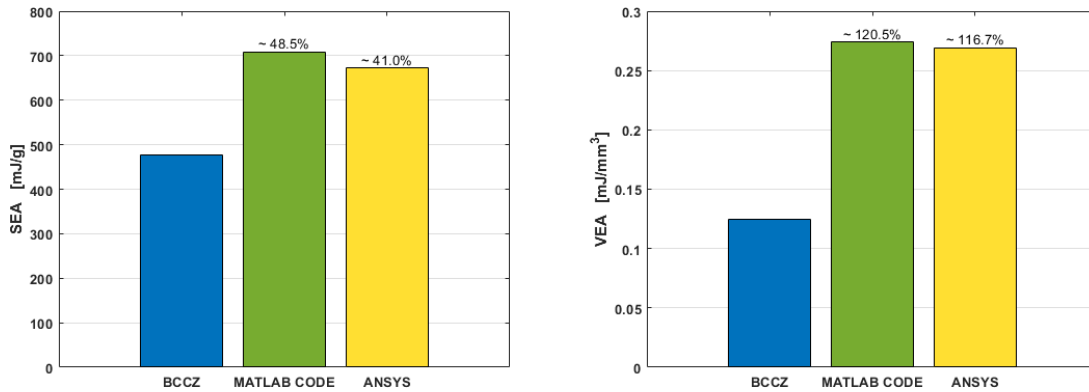


Figure 5.12: Comparison of SEA and VEA - BCCZ1.

The percentages are scarcely different, again confirming the validity of the results achieved by the automatic code. Regarding the BCCZ specimens, subjected to optimization Process 1, the largest deviation is for SEA, suggesting that probable erroneous approximations were made in the recalculation of the masses involved, as this parameter is defined from the value of the energy absorption, dividing the latter by the mass.

#### 5.2.4 Validation for BCCZ sample graded by Process 2

When Process 2 is implemented, only a few diameters are subject to optimization, so the geometry shows only slight variations, compared to the uniform BCCZ sample. It is shown in Figure 5.13 and analyzed according to the same standards, BCs and imposed displacement, as previously applied.

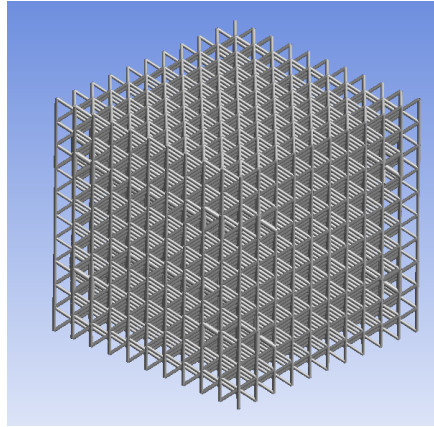


Figure 5.13: Geometry of the graded sample post optimization.

The confrontation is carried out comparing the uniform BCCZ data, the results obtained from the operating process 2 and through a bilinear simulation in Ansys, so there are only 0.7% differences in mass.

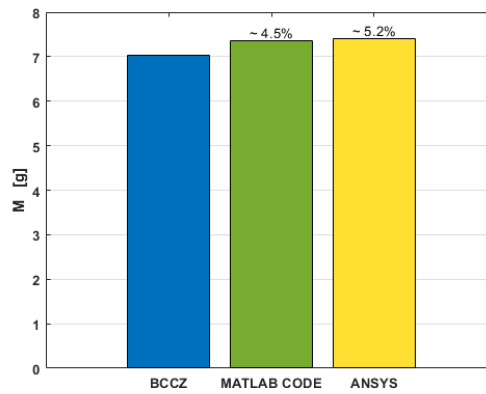


Figure 5.14: Comparison of the masses - BCCZ2.

There are small percentage deviations due to the connection zones between intersecting struts. The values obtained with the numerical analysis generate a new redistribution of internal stresses, which will be less inhomogeneous than the starting specimen, with a concentration only in the upper external layer of cells, with a better mechanical behaviour 5.15

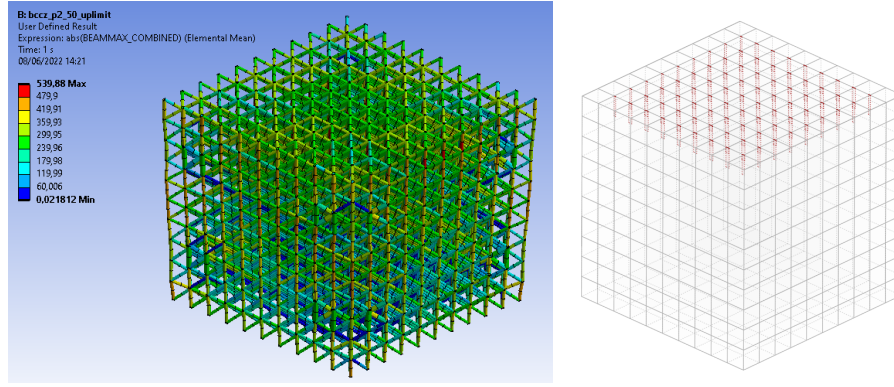


Figure 5.15: Stress field of the graded sample post optimization - BCCZ2.

In terms of SEA and VEA, similar increases are obtained, proving the effectiveness of the process implemented in Matlab for the BCCZ2 configuration.

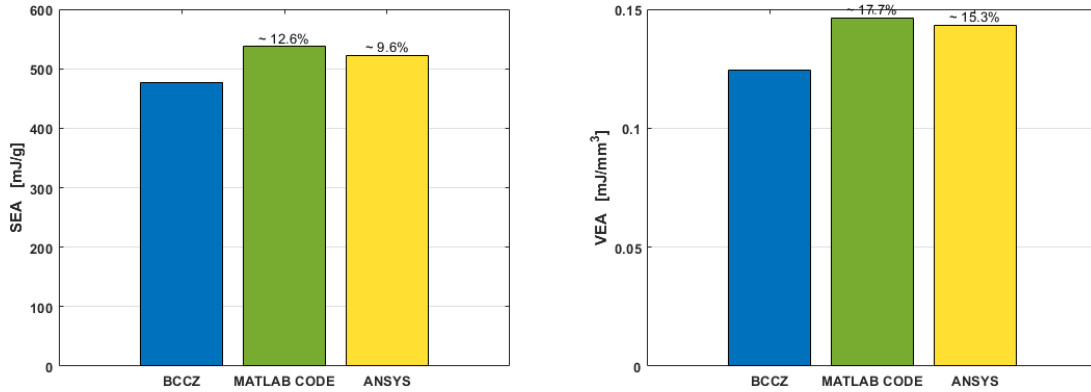


Figure 5.16: Comparison of SEA and VEA - BCCZ2.

In term of specific absorption energy values, the outputs (Matlab - Ansys) differ by 3.0%, and for volumetric values by 2.4%. These percentages are lower than those recorded in the case of the comparison of the BCCZ1 specimens, so that, with the inclusion of the z-struts, the code better predicts the energy properties for the implementation of Process 2 instead of the first one. In relation to the computational costs in time provided by the Matlab code shown in the Section 5.5 (compared to Ansys) , this results are fully validated, thus ensuring minimal deviations and great benefits in analysis time.

### 5.3 Comparison of the computational costs

The results obtained through the implementation of the Matlab code led not only to the search for the optimum thicknesses to increase the specific and volumetric energy absorption levels, but also allowed for the automatic recalculation of the internal stresses and energy performances for each individual RVE that makes up the specimen with dimensions of 30 mm per side. This was validated by creating the geometries in Ansys Workbench and performing the analyses. The results are fully comparable, making the code reliable for both optimization and static analysis. Among the benefits of the latter is certainly the saving in terms of computational time, which can be appreciated by viewing the Table 5.21. Analysis times range from three to seven hours, down to orders of magnitude of a minute for analysis by code.

Category	Hardware/Software
Operating system (OS)	Windows 10 64-Bit system
Central processing unit (CPU)	Intel(R) Core(TM) i7 CPU 70 @ 2.93GHz
Random-access memory (RAM)	20,0GB DDR3
Graphics processing unit (GPU)	NVIDIA GeForce GT 610

Table 5.20: Computer technical specifications used for the analyses.

The computational times refer again to a computer in the department's offices of the Konstruktiver Leichtbau und Bauweisen (KLuB - TU Darmstadt), whose technical specifications are given in the Table 5.20.

10x10x10	Ansys computational cost	Matlab computational cost
BCCZ	3h 11m	0h 3m
FCC	3h 23m	0h 3m
FCCZ	3h 07m	0h 3m
FBCC	6h 38m	0h 3m
FBCCZ	7h 54m	0h 4m

Table 5.21: Computational cost in time for the Ansys and Matlab code static analyses.

This is of particular interest, since as shown in Section 5.4, the deviations in output are minimal, but the computational cost is considerable. This leaves room for future analyses, even on other configurations, which can be carried out relatively in a rapid manner.

# Chapter 6

## Experimental tests

Based on the results obtained in the previous chapters, it has been decided to validate the better performers models analyzed using Ansys and automatically via Matlab code, experimentally as well. The BCC and BCCZ specimens, graduated through Process 1 and 2, showed strong adaptability to the optimization methods, generating substantial increases as far as SEA is concerned. In order to validate these results, a campaign of static compression tests was carried out to obtain the stress-strain curves of each specimen as output and, once the mechanical properties are known, to calculate the energetic ones. By comparing the values of the energy absorption (main output of interest), the model and the results obtained will be validated. The phases carried out during the experimental activity were:

- realization of the 'CAD' and '.stl' files;
- production of the specimens in AlSi10Mg through SLM technique;
- detachment, marking and grinding;
- cleaning by immersion in ultrasonic water;
- drying in oven at 80° for 16h;
- density measurement;
- heat treatment at 350° for 2h;
- execution of axial compression test.

The six specimens tested, in order to make a comparison with the numerical results, are schematized in the table [6.1](#):

BASE CELL UNIT	CONFIGURATION	DIMENSION [mm]
BCC	UNIFORM (same diameter)	30x30x30
BCC	GRADED BY PROCESS 1	30x30x30
BCC	GRADED BY PROCESS 2	30x30x30
BCCZ	UNIFORM (same diameter)	30x30x30
BCCZ	GRADED BY PROCESS 1	30x30x30
BCCZ	GRADED BY PROCESS 2	30x30x30

Table 6.1: Sample typologies selected for the experimental tests.

As regards the geometric configuration of the specimens, this is clearly represented in Chapter 5, whereby a diameter of 0.37 mm (the same for each struts) is given for the uniform specimens BCC and BCCZ, while for the configurations BCC1, BCC2, BCCZ1 and BCCZ2, the '.stl' files were produced on the basis of the 3D databases in Appendix [B], whereby the maximum and minimum diameters are specified again in the Table 6.2:

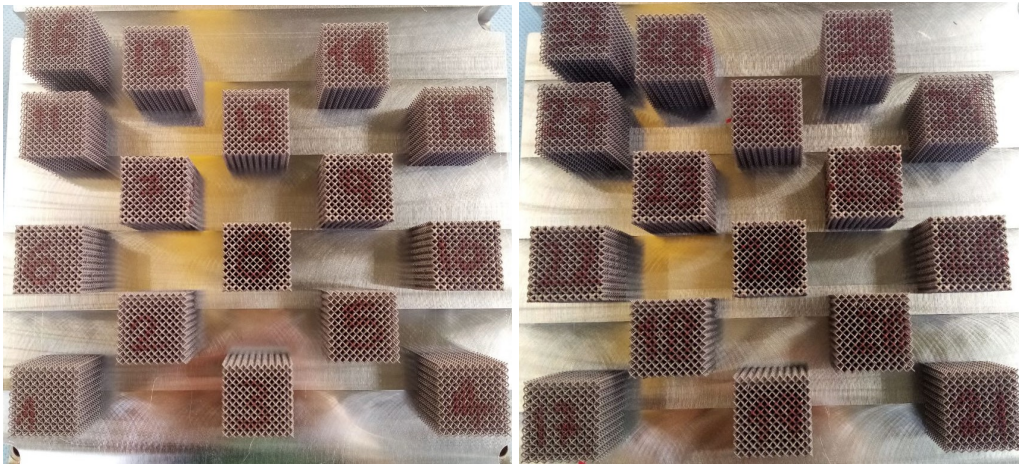
	t (min) - [mm]	t (max) - [mm]
BCC - Process 1	0.3700	0.8900
BCC - Process 2	0.3700	0.4573
BCCZ - Process 1	0.3700	1.0100
BCCZ- Process 2	0.3700	0.4648
FCC- Process 1	0.3700	1.1400
FCC- Process 2	0.3700	0.4397
FCCZ - Process 1	0.3700	0.9600
FCCZ - Process 2	0.3700	0.4504
FBCC - Process 1	0.3700	0.7700
FBCC - Process 2	0.3700	0.4293
FBCCZ - Process 1	0.3700	0.7500
FBCCZ - Process 2	0.3700	0.4167

Table 6.2: Maximum and minimum thicknesses for a threshold equal to the mean value (Case 3 with the upper limit), implemented to realise '.stl' files.

As required by current regulation [65] for each of the configurations, a minimum of five specimens were printed using EOS M290 (Selective Laser Melting printer), provided in the workshops of the Konstruktiver Leichtbau und Bauweisen (KLuB - TU Darmstadt) and shown in the Figure 6.3 (b). The uniform BCC and BCCZ configurations have an additional sixth specimen printed for the two platforms, as shown in the Figure 6.1, which includes the numbering



chosen to ensure their recognition during the experimental campaign.



*Figure 6.1: Numbering of test specimens on the platforms.*

After the marking phase, they were separated from the printing platform and manually grinded, until a final height of 30 mm was obtained.

## 6.1 Experimental Setup

Different preparation steps were carried out to make the density measurement and experimental results as reliable as possible. After the initial phases described, to remove the powder residue, each sample was immersed in distilled water in a special machinery that removed the print residue using ultrasound [6.2](#) (b). The specimens were then dried by a short annealing in an oven at a temperature of  $80^{\circ}$  for 16 hours. Air bubbles entrapped in the water surrounding the specimens had to be removed as they would make the result inaccurate, whereby all 32 specimens were incorporated into a vacuum desiccator [6.2](#) (a) for a time of about ten minutes. For the weight-in-air measurement, the machine shown in Figure [6.3](#) was used, therefore the weight was obtained by placing each specimen inside the chamber and closing the outer glass walls. For the purpose of estimate the mass of the specimens in water (data required to implement Archimedes' density formula), a wire with a hook was used to immerse the test articles into the tank filled with water (Figure [6.3](#)).



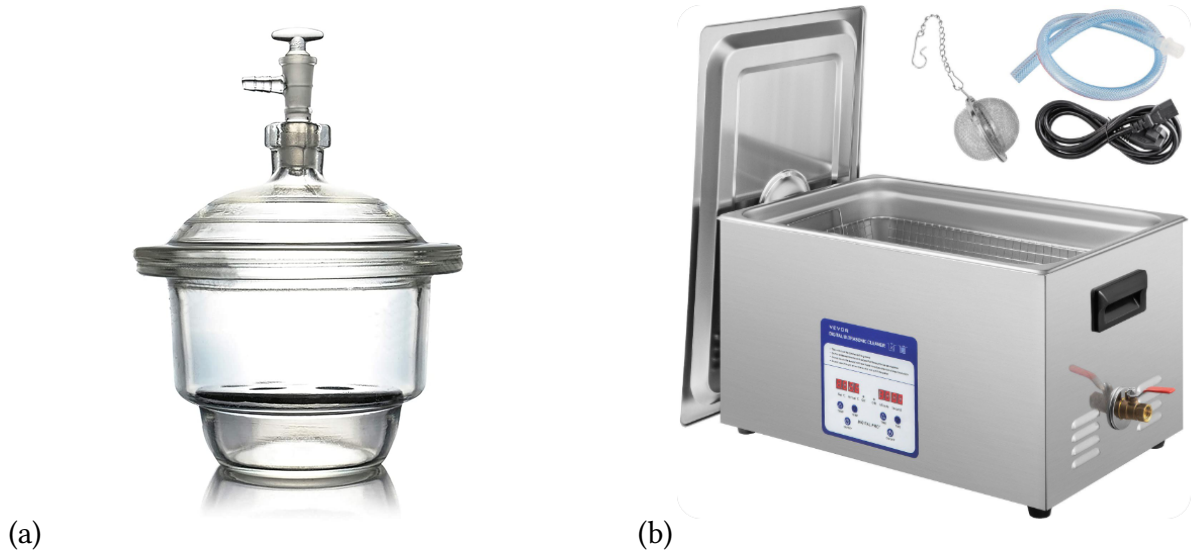


Figure 6.2: (a) Vacuum Desiccator with tube and stopcock. (b) Ultrasonic Cleaner.

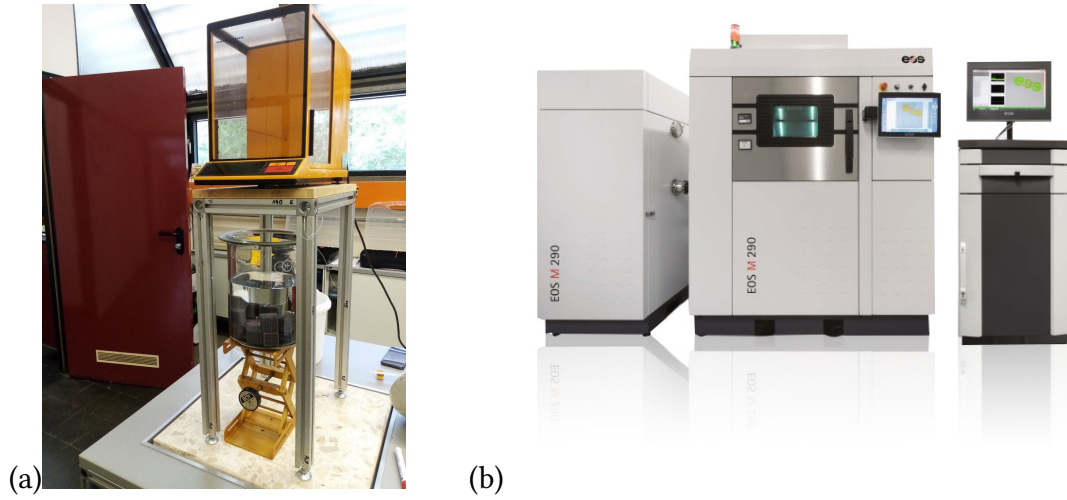


Figure 6.3: (a) Experimental apparatus for density measurement and (b) SLM Printer EOS M 290.

Before each measurement of the mass, the temperature of the water was recorded, as the density is temperature-dependent. After all the measurements, the specimens were taken out of the containers and put into the oven to dry out as a preparation for the pre-processing phase. In order to obtain experimental results as comparable as possible to the numerical model implemented via Ansys, it was decided to carry out heat treatment according to a temperature cycle defined by the [6.4](#) realizing an annealing in oven at  $350^{\circ}$  for 2h , as extensively described in [\[66\]](#).

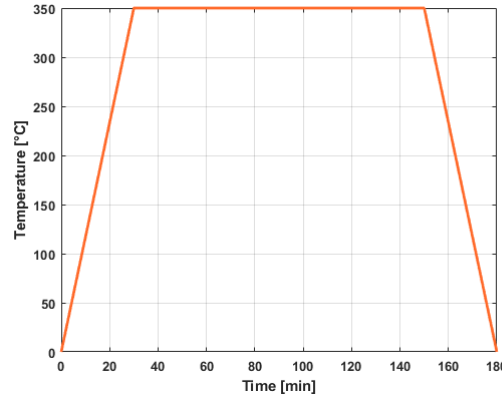


Figure 6.4: Temperature cycle for the heat treatment.

After this heat treatment, it was possible to perform static tests on the 32 specimens made, through the compression testing machine shown in [6.6](#). It is a universal testing machine configured to determine material's strength and deformation behavior under compressive load. It consists of a load cell, compression test tools, electronics, and a drive system. It is controlled by testing software used to define machine and safety settings and store test parameters specified by standards such as ASTM and ISO. Measuring the force until a specified load or distance has been reached, or until the specimen cracks or breaks, permit to predict how the samples will perform when implemented for its intended purpose.

### 6.1.1 Density measurement

Archimedes' principle states that an object floating or fully immersed in a fluid is buoyed up by a force equal to the weight of the fluid displaced by the object. The buoyant force on an object immersed in a liquid can also be determined by weighting an object in air and then in water. The apparent loss of weight of the object is equal to the buoyant force of the water. Constructing the free body diagram and imposing balance, it is possible to obtain the equations containing the unknown density, which include force  $F$ , mass  $m$  and volume  $V$ :

$$F_A = \rho \cdot V \cdot g \quad (6.1)$$

$$F_W = \rho_W \cdot V \cdot g \quad (6.2)$$

In which subscripts 'A' and 'W' indicate the measurement condition in air and in distilled water. The following formula was then implemented to obtain the density measurement:

$$\rho = \frac{m_A \cdot \rho_W}{m_A - m_W} \quad (6.3)$$

All the data collected and measured have been summarised in the Table 6.3, which shows the value of the mass in air, in water and the final density, obtained according to the formula given and the standards [67].

	$M_a$ [g]	$M_w$ [g]	$\rho$ [g/cm <sup>3</sup> ]
<b>BCC - UNIFORM (same thickness for each strut)</b>	5.9492	3.7054	2.6455
<b>BCC - GRADED BY PROCESS 1</b>	15.0691	9.3862	2.6458
<b>BCC - GRADED BY PROCESS 2</b>	6.4577	4.0210	2.6443
<b>BCCZ - UNIFORM (same thickness for each strut)</b>	6.6740	4.1508	2.6391
<b>BCCZ - GRADED BY PROCESS 1</b>	14.5613	9.0773	2.6493
<b>BCCZ - GRADED BY PROCESS 2</b>	7.0814	4.4243	2.6592

Table 6.3: Mass in air, mass in water and density.

The material is AlSi10Mg, widely used for applications in the additive manufacturing field. To assess the goodness and accuracy of the measurements, it is worthwhile to compare the density values obtained for each individual test specimen. The standard deviation, represented by means of a large zoom in the Figure 6.5, shows that the discrepancies are minimal, so the data are acquired and validated.

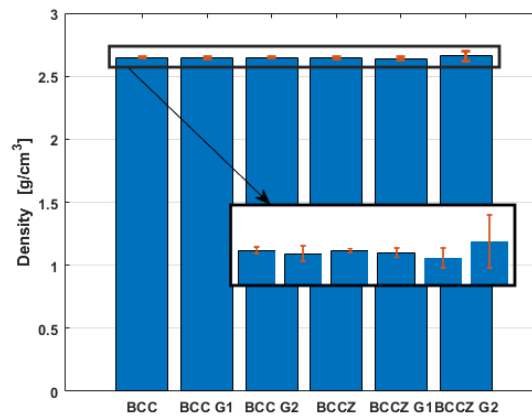
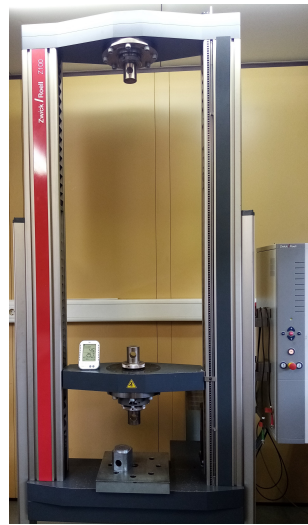


Figure 6.5: Density values of the samples.

As can be seen from the Figure, the densities of the specimens are completely comparable, with negligible deviations, which validates and enhances the success of the scanning strategy, which led to an optimal realization of the final product.

### 6.1.2 Static compression testing

The cubic lattice structure specimens were subjected to compression tests in order to investigate the absorbing capabilities of the investigated cell geometries. A ZwickRoell Z100 compression testing machines [6.6] was utilized to compress the test specimens, executed on the basis of the current DIN 50134 standard [65]. Based on the standard, a minimum of five specimens per configuration were printed and tested in a temperature environment of approximately 23°. Lattices were compressed between two parallel aluminum plates and an hydraulic heads were operated by a controlled displacement value and logged output data for concurrent force and displacement.



*Figure 6.6: ZwickRoell compression testing machines.*

On this machine, the top plate moves upward to compress the specimen against the fixed bottom base. The compression rate was selected manually corresponding to a total displacement of 2 mm. This rate was selected to provide a quasi-static load relatively free of inertial effects and to ensure a perfect correspondence with the analyses done via Ansys. All lattice specimens were compressed in the build direction (z), normal to each build layer of the part.

## 6.2 Data processing

Through the static compression tests carried out in the laboratory through the apparatus shown in Figure [6.6], fundamental data were extrapolated to interpret the performance and behaviour of the different configurations of interest. In this section, the samples subject to optimization of the struts' diameters are indicated with the letter 'G'. An additional number '1'

or '2' indicates the optimization process chosen. In the absence of such indications, reference will be made to the configuration with the same thickness for each strut. Among the parameters and graphs to be extrapolated, it is first necessary to derive the stress-strain curves. In this case, the choice was made to obtain graphs for each of the specimens and for an averaged value for each category. Once the curves were obtained, it was possible to calculate:

- Young modulus;
- Yield stress and strain;
- Plateau stress and strain;
- Densification stress and strain;
- Energy absorption;
- Specific energy absorption;
- Volumetric energy absorption.

### 6.3 Stress-strain curves

From the experimental tests performed in the laboratory, it was possible to extract the stress-strain curves. From the Force (Newton) and displacement (mm) values, acquired via the sensor system, were obtained:

$$\sigma = \frac{F}{A} \quad (6.4)$$

$$\epsilon = \frac{d}{l} \quad (6.5)$$

By implementing these equations, it was possible to acquire a data set for each of the six tested configurations. Using a Matlab code, these were combined to obtain the stress-strain curves. A total of 32 curves were extrapolated (one for each test specimen), sub-divided into 6 macro groups:

- BCC, which indicates the group of uniform BCC specimens numbered 1 to 5 (plus the specimen 16);
- BCC G1, which indicates the group of graded (by Process 1) BCC specimens numbered 6 to 10;

- BCC G2, which indicates the group of graded (by Process 2) BCC specimens numbered 11 to 15;
- BCCZ, which indicates the group of uniform BCCZ specimens numbered 17 to 21 (plus the specimen 32);
- BCCZ G1, which indicates the group of graded (by Process 1) BCCZ specimens numbered 22 to 26;
- BCCZ G2, which indicates the group of graded (by Process 2) BCCZ specimens numbered 27 to 31.

For each of the configurations, it was also decided to use both the full range of deformations and a reduced range up to an  $\epsilon$  of 0.067, in order to be able to make a comparison with the numerical analyses carried out in the previous chapters. The representation of all curves, for each specimen, up to a value of  $\epsilon$  of 0.5 is shown in the Figures 6.8 and 6.10, while the illustrations up to an  $\epsilon$  of 0.067 is referred to the Figures 6.7 and 6.9. For the purpose of to visualize more distinctly the trends assumed by each individual configuration, representations of all the curves (32) have also been shown, grouped by typology.

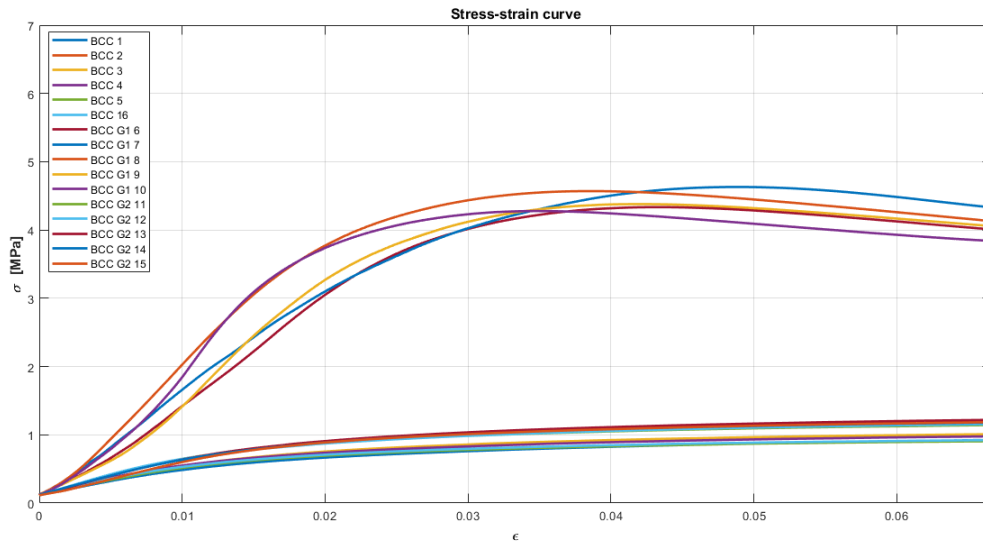


Figure 6.7: Stress-strain curves of all BCC samples until a strain equal to numerical analysis.

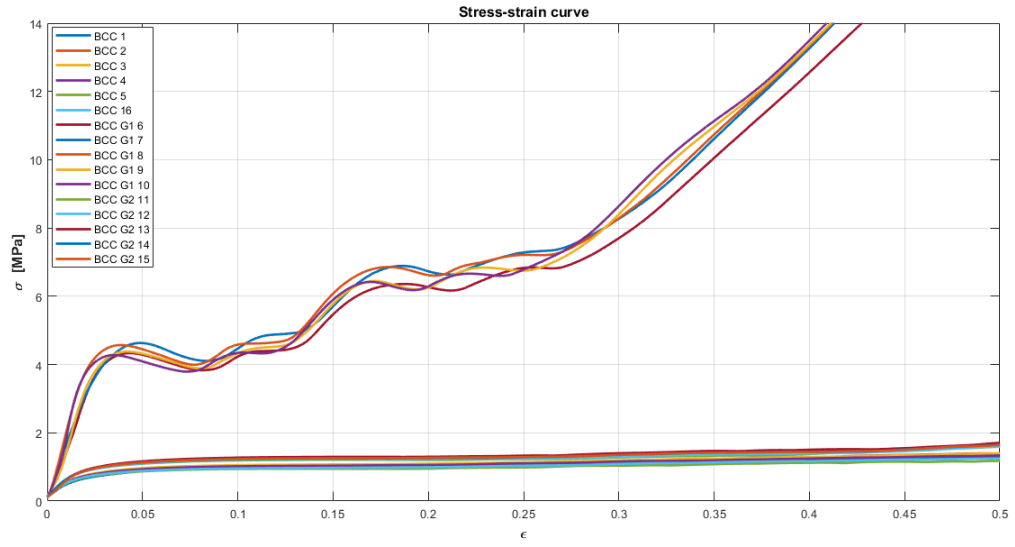


Figure 6.8: Stress-strain curves of all BCC samples until a strain equal to 0.5.

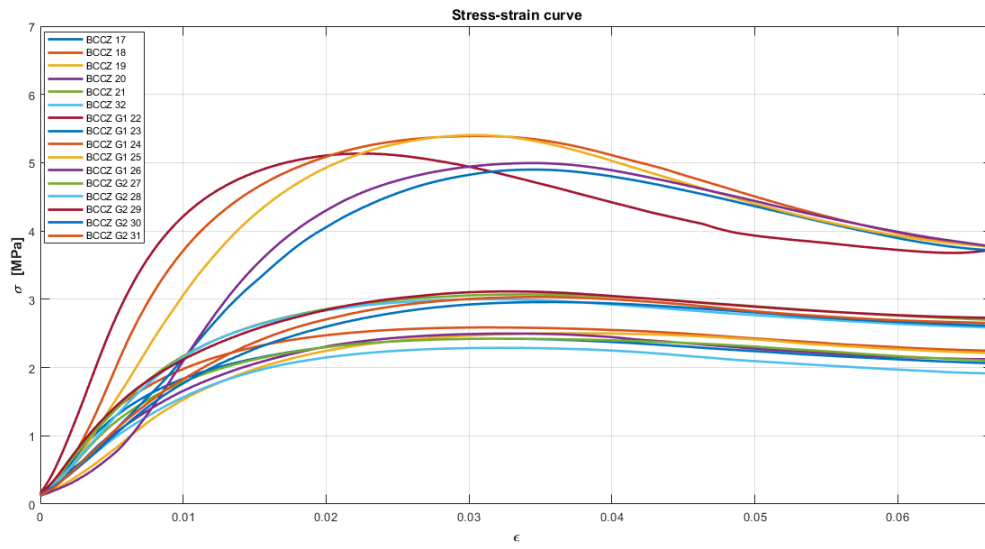


Figure 6.9: Stress-strain curves of all BCCZ samples until a strain equal to numerical analysis.

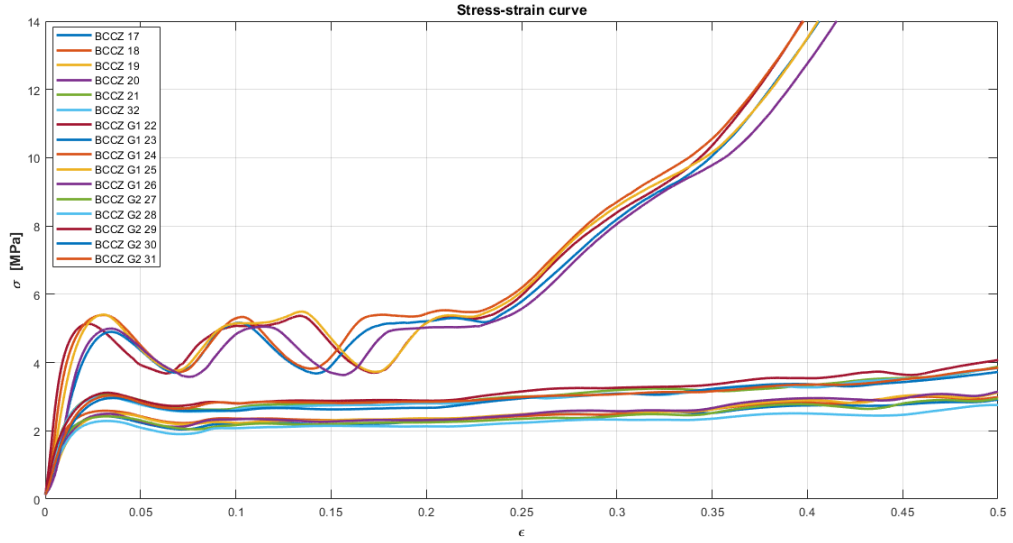


Figure 6.10: Stress-strain curves of all BCCZ samples until a strain equal to 0.5.

### 6.3.1 Average representation of stress-strain curves

A further Matlab code was implemented to more clearly depict the behaviour of each configuration. For all six cases, an averaged value was calculated for the stress and strain vectors to identify a single representative curve.

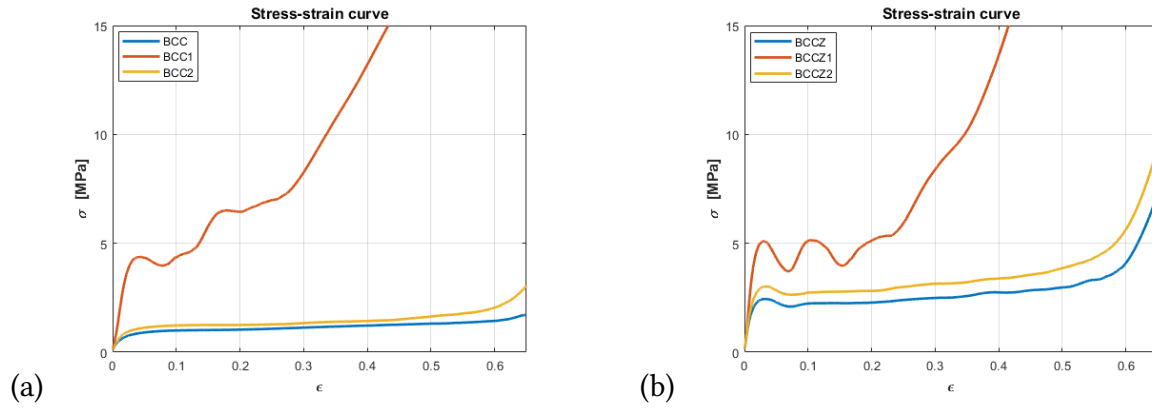


Figure 6.11: Average representation of stress-strain curves of all (a) BCC samples and (b) BCCZ samples.



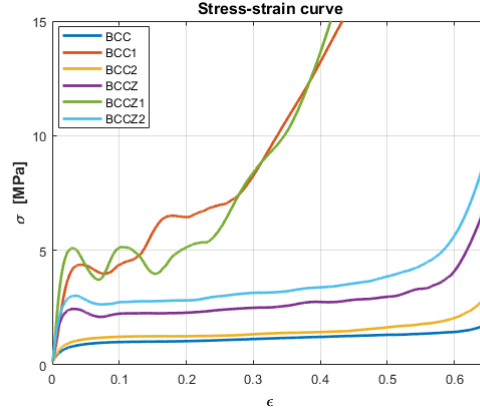


Figure 6.12: Average representation of stress-strain curves of all the samples.

The curves are similar to those of common porous or cellular materials, which exhibit three ideal regimes under uniaxial compression:

- a pre-collapse regime (including the linear elastic stage);
- a plateau regime with approximately constant stress;
- a final densification regime with steeply increasing stress.

The linear elastic regime is characterized by elastic modulus, the plateau regime by plateau stress and the densification regime starts from a densification strain, where the individual cell strut comes into contact with each other, and exhibits dramatically increasing strength. With the purpose of identifying each zone, the corresponding values in terms of stress and strain will be calculated in the following sections. Visual observation during compression test indicated that the shear failure for uniform strut samples corresponded to the first stress peak in the stress-strain curves. The stress-strain curves of all graded samples started with smaller stress peaks, and the subsequent peaks were increasingly higher, indicating an improvement in the load resistance to further crush the cells with larger strut diameters. The maximum peak was the last stress peak before densification, which started later for graded samples compared to uniform strut samples. The stress values of BCCZ1 and BCCZ2 models were significantly higher than BCC1 and BCC2 configurations, thanks to the vertical struts, reinforced the strength of the structure. The progressive deformation from least to most dense layer (sequential failure examined within the paragraph 6.8.1) can be observed in the stress-strain curves with the multi-peak trends for the graded configuration.

## 6.4 Young modulus

By extracting all the stress-strain curves following the indications of the *DIN50134* standard, it was possible to derive the Young's modulus, an index of the stiffness of the specimens. It is identified as the slope of the linear line defined between two different values of the stress, equal to 20% and 70% of the Plateau stress.

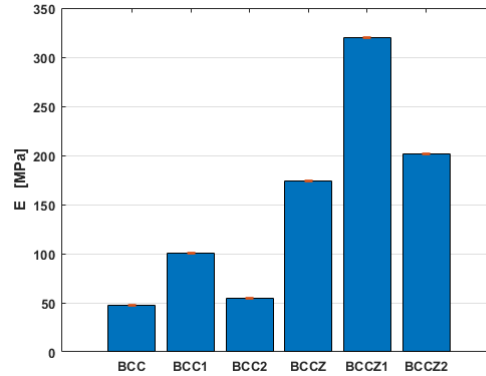


Figure 6.13: Young modulus averaged for the six tested configurations.

In terms of stiffness, the best configuration is BCCZ in general, with the highest values for the configuration subject to optimization by process 1. Also for BCC specimens, there is an increase in Young's modulus and thus mechanical performance by adopting the geometric variations for the diameters (G1 and G2).

## 6.5 Yield point

The yield strength or yield stress corresponds to the point at which the material begins to deform plastically. The yield strength is often used to determine the maximum allowable load in a mechanical component, since it represents the upper limit to forces that can be applied without producing permanent deformation. In some materials, such as aluminium, there is a gradual onset of non-linear behavior, making the precise yield point difficult to determine. In such a case, the offset yield point (or proof stress) is taken as the stress at which 0.2% plastic deformation occurs. Yielding is a gradual failure mode which is normally not catastrophic, unlike ultimate failure. In the context of lattice structures, the standard does not establish a way to univocally calculate the yield point, as it is not a fundamental parameter in determining the behaviour of such structures. In order to derive a theoretical yield point, the convention

adopted for metals is followed, resulting in the values represented into the hystograms below:

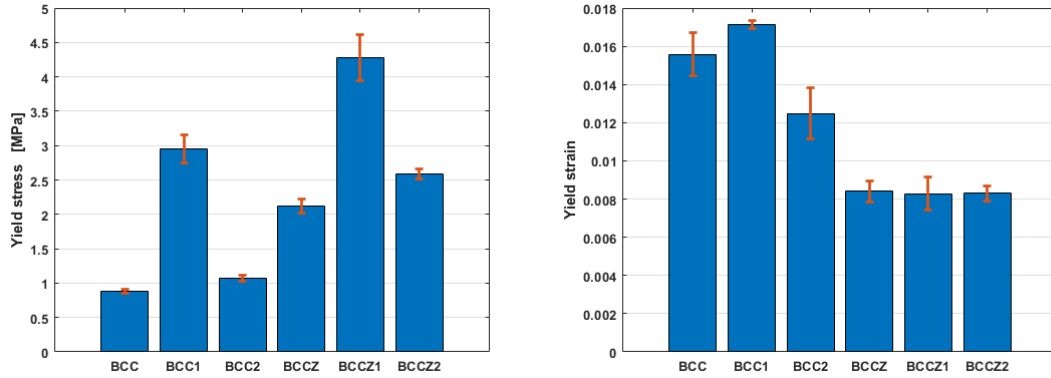


Figure 6.14: Yield stress and strain.

As is visible from the stress-strain curves, the highest values of  $\epsilon_y$  occur for BCC configurations, while the highest  $\sigma_y$  occur for BCC1 and BCCZ1.

## 6.6 Plateau region

The plateau regime is characterized by an approximately constant stress and influence EA levels for each sample. The plateau stress  $\sigma_{PL}$  is calculated as the arithmetical mean of the stress at a strain interval between 20% and 40%:

$$\sigma_{pl} = \frac{1}{\epsilon_2 - \epsilon_1} \int_{\epsilon_1}^{\epsilon_2} \sigma d\epsilon \quad (6.6)$$

where  $\epsilon_1$  and  $\epsilon_2$  equal 0.2 and 0.4, respectively. For each of the six configurations, initial plateau stress and strain values were calculated. A clear comparison is outlined by the histograms below, in which it is also possible to appreciate the standard deviation that each configuration exhibits:

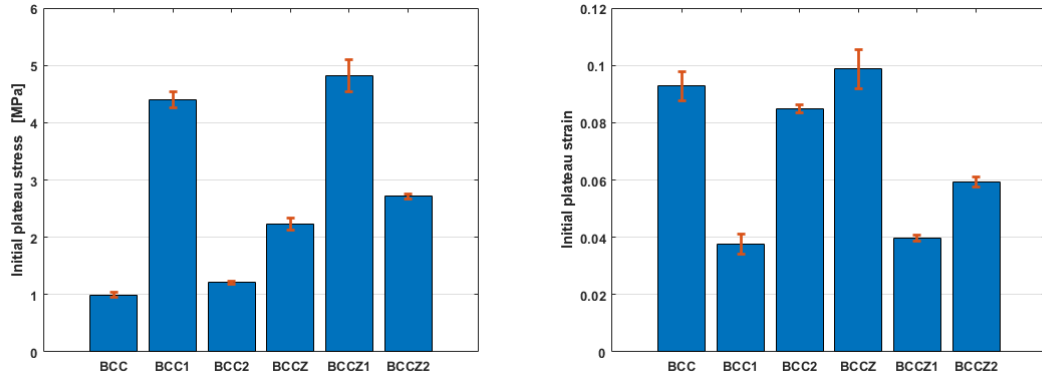


Figure 6.15: Initial plateau stress and strain.

## 6.7 Densification region

The densification strain  $\epsilon_D$  is identified by using the energy absorption efficiency ( $\eta$ ) method:

$$\eta = \frac{1}{\sigma_{pk}} \int_0^{\epsilon} \sigma d\epsilon \quad (6.7)$$

$$\frac{d\eta}{d\epsilon} = 0 \quad (6.8)$$

Peak stress  $\sigma_{pk}$  is the maximum stress registered up to the strain when the integral is estimated.

Using  $\eta$  it is possible to determine the densification strain as the point where the Energy Absorption Parameter reaches its maximum. In order to determine the densification point uniquely, the efficiency curves for each configuration have been depicted in the Figures [6.16](#), [6.17](#) and [6.18](#).

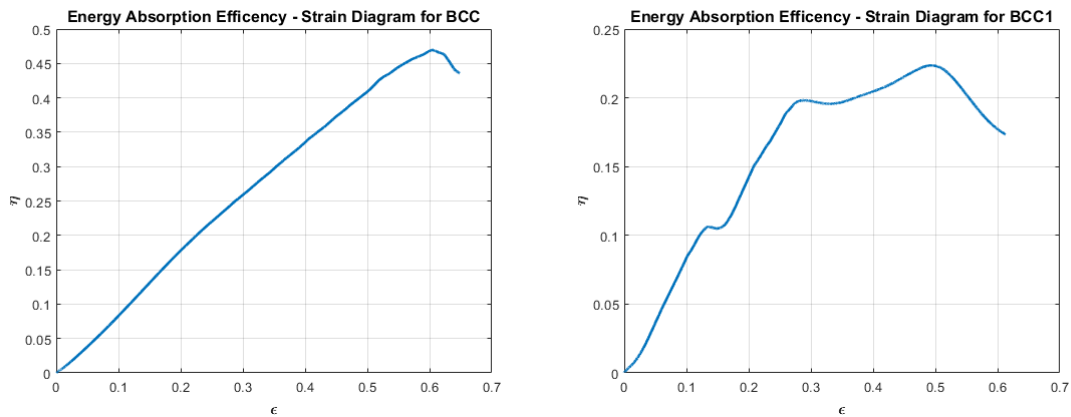


Figure 6.16: The energy absorption efficiency for BCC and BCC1 samples.

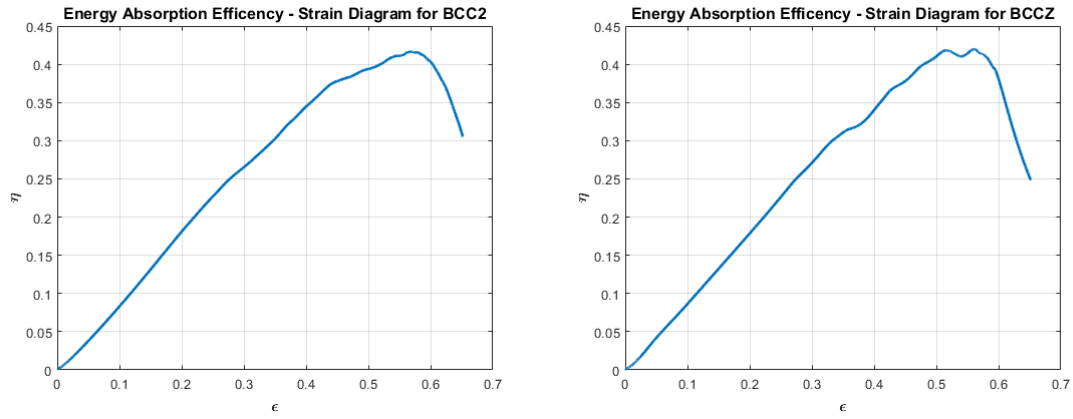


Figure 6.17: The energy absorption efficiency for BCC2 and BCCZ samples.

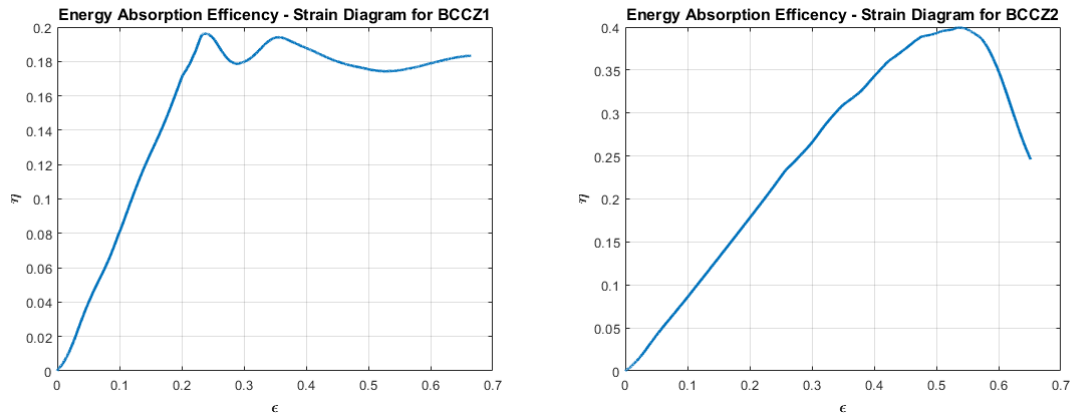


Figure 6.18: The energy absorption efficiency for BCCZ1 and BCCZ2 samples.

A single peak is recorded for the BCC, BCC2, BCCZ and BCCZ2 configurations. Substantial variations in the diameters of each RVE were included within BCC1 and BCCZ1, in which sequential layer-by-layer collapses generate a multi-peak trends. For the latter two cases, the absolute maximum of the curves was assumed, for which the corresponding stress and strain values were calculated, uniquely identifying densification:

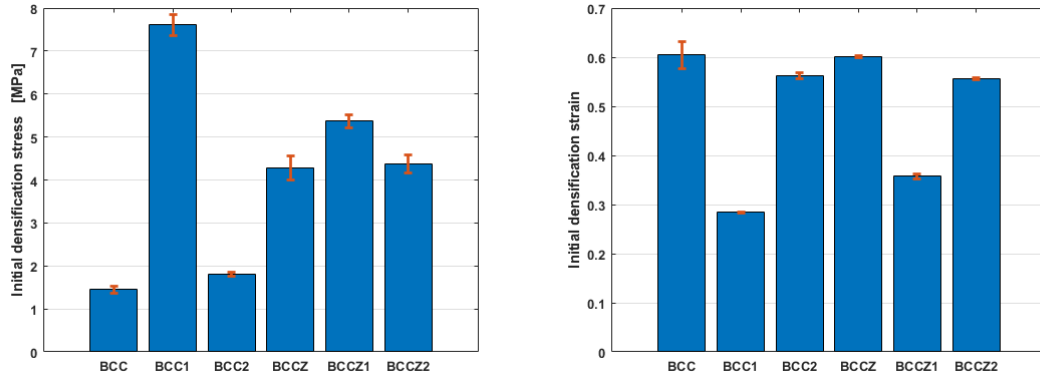


Figure 6.19: Densification stress and strain.

Following the data processing presented in [68], the densification region ( $\epsilon_D$ ) is determined as the value where the energy absorption efficiency  $\eta$  reaches the maximum (at the last peak).

## 6.8 Energy absorption

Once the stress-strain diagram is obtained, the Volumetric Energy Absorption can be simply defined as:

$$VEA = \int_0^{\epsilon} \sigma(\epsilon) d\epsilon \quad (6.9)$$

In which the upper limit of integration corresponds to a  $\epsilon$  equal to 0.067 in order to perform a subsequent comparison again with the values obtained both from the numerical analysis using Ansys and the results obtained from the automatic Matlab code. After extracting VEA, the energy absorption (EA) and the specific one (SEA) are automatically determined, in the first case by multiplying the value obtained by the volume  $V$  and in the second by further dividing by the mass  $m$  of each specimen.

$$EA = VEA \cdot V \quad (6.10)$$

$$SEA = \frac{VEA \cdot V}{m} \quad (6.11)$$

Analysing these histograms shows that in terms of SEA, the best performing configuration is the BCCZ graded by process 1, followed by the BCCZ subject to process 2, with excellent values also for the BCC1 type. In terms of VEA, the highest values are recorded for the specimens (both BCC and BCCZ) made by process 1.

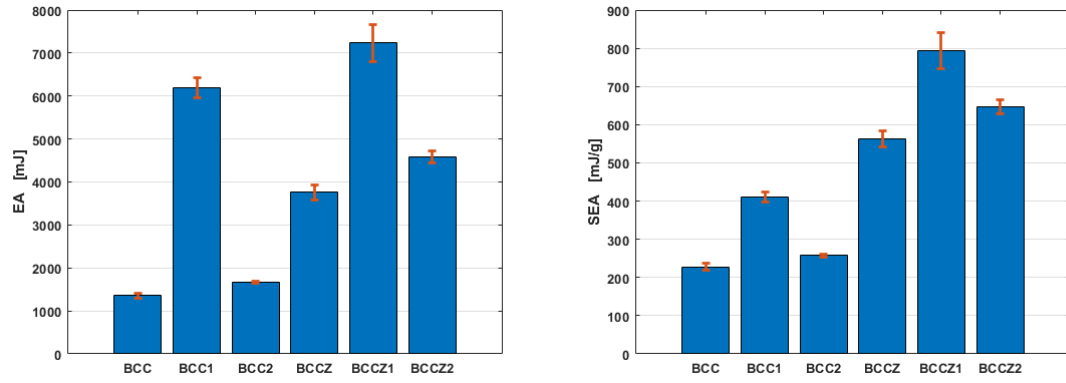


Figure 6.20: Energy absorption and specific energy absorption.

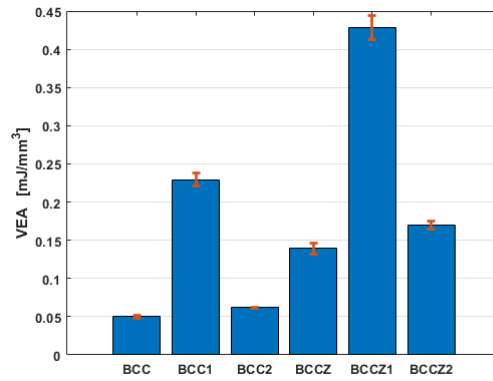


Figure 6.21: Volumetric energy absorption.

The trends are modified as the upper integration extreme changes. Indeed, by setting a  $\epsilon$  equal to the densification point as the value, the specimens showing the highest values, both in terms of SEA and VEA, are the BCCZs optimised by process 2:

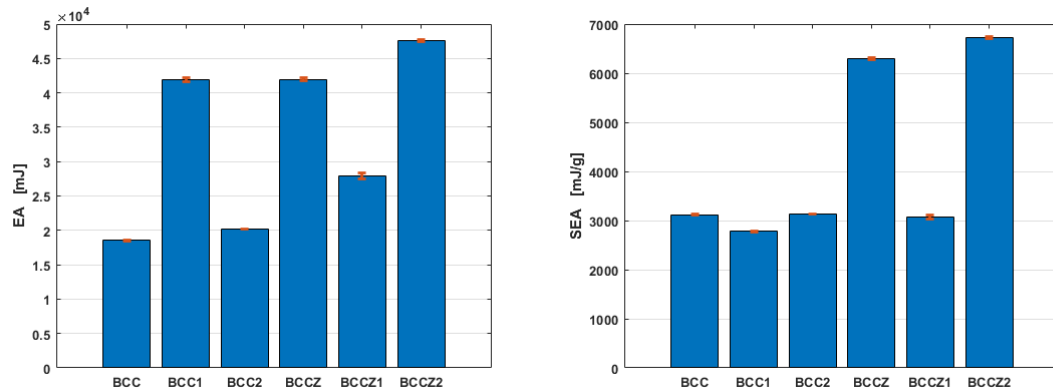


Figure 6.22: Energy absorption and specific energy absorption until the densification point.

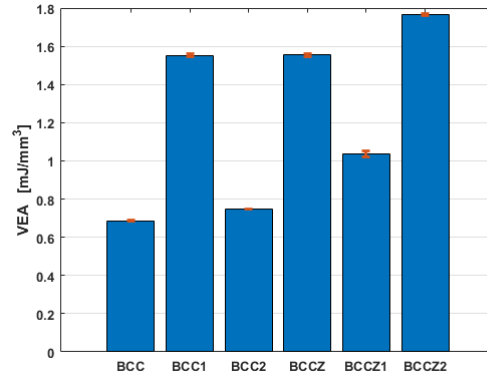


Figure 6.23: Volumetric energy absorption until the densification point.

### 6.8.1 Macro areas of characterization

Once all characteristic points have been calculated and the stress-strain curves of each type of specimen have been extracted, it is possible to partition the graph area into three macro regions, representative of typical behavior of lattice structures. The typical behavior can be summed up in three phases: a linear segment with an initial stress peak, a plateau where most of the energy absorption characteristic lies and finally a rise that represent the densification. On the basis of this classification, stress-strain curves were represented in combination with efficiency. This makes it possible to relate the two parameters and unambiguously identify the regions of interest, clearly delineating the point of densification. Within the Figures 6.24, 6.25 and 6.26, the notation shown in the Table 6.4 was chosen:

LINEAR REGION		Y	Yield point
PLATEAU REGION		P	Initial Plateau point
DENSIFICATION REGION		D	Densification point

Table 6.4: Notations to identify the classification regions.



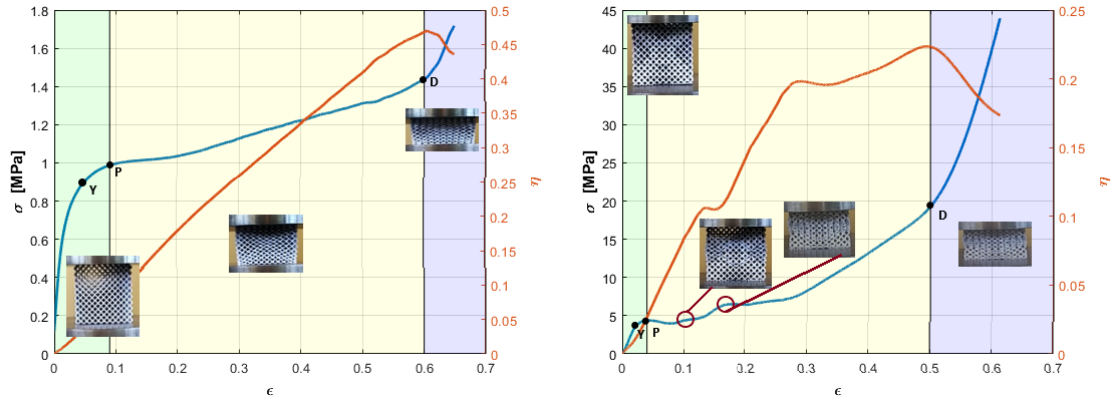


Figure 6.24: Stress-strain curve schematization - BCC and BCC1.

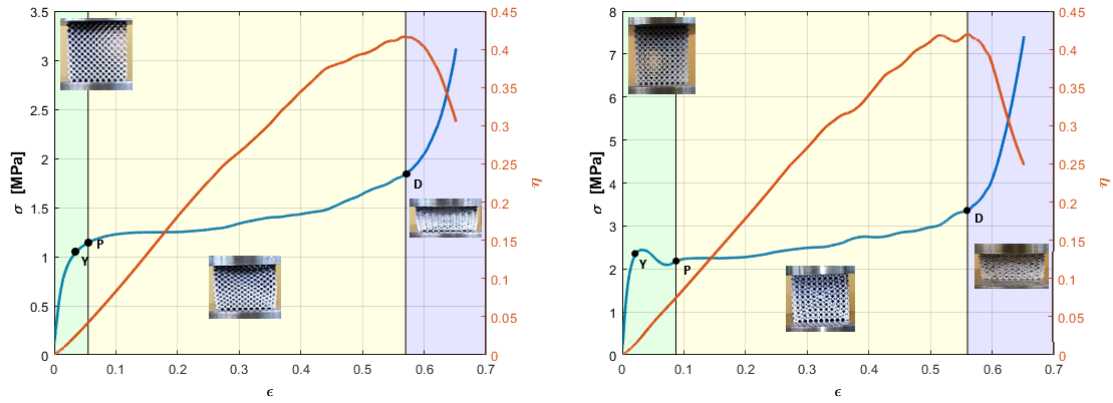


Figure 6.25: Stress-strain curve schematization - BCC2 and BCCZ.

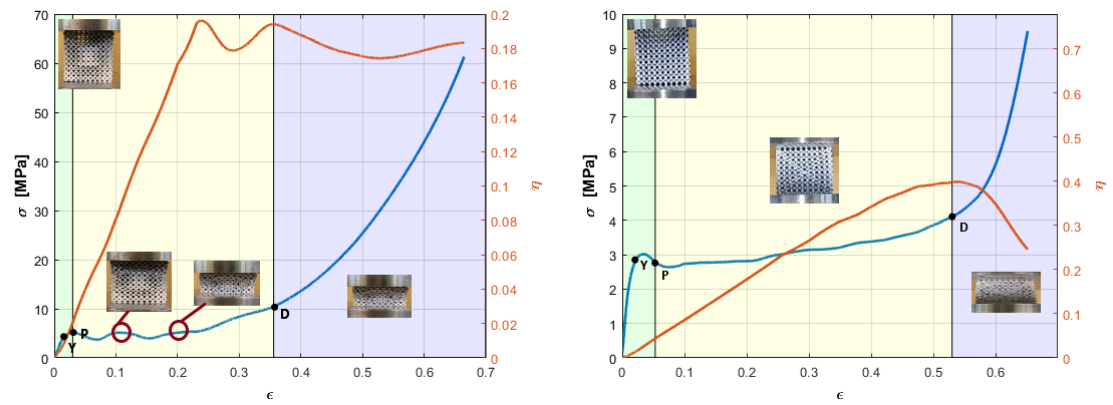







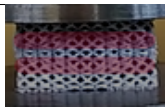





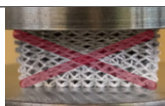


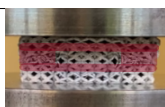


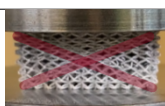
Figure 6.26: Stress-strain curve schematization - BCCZ1 and BCCZ2.

### 6.8.2 Identification of the macro-behavior

Each specimen tested has different failure modes. Regarding uniform configurations, the experimental campaign confirmed the results obtained in the literature in [12]. Selected images of lattice specimens during quasi-static testing are presented in the Table 6.5. For BCC and BCCZ specimens, the failure plane was diagonal on two of the parallel vertical planes.

	FAILURE MODE
<b>BCC - UNIFORM</b>	COLLAPSE ALONG A DIAGONAL PLANE
<b>BCC - GRADED BY PROCESS 1</b>	SEQUENTIAL COLLAPSE LAYER BY LAYER (primary failure along two diagonal centerline semi-planes)
<b>BCC - GRADED BY PROCESS 2</b>	COLLAPSE ALONG A DIAGONAL PLANE
<b>BCCZ - UNIFORM</b>	COLLAPSE ALONG TWO DIAGONAL PLANES
<b>BCCZ - GRADED BY PROCESS 1</b>	SEQUENTIAL COLLAPSE LAYER BY LAYER
<b>BCCZ - GRADED BY PROCESS 2</b>	COLLAPSE ALONG TWO DIAGONAL PLANES

For BCC samples, collapse occurs progressively along a single diagonal plane, while for BCCZs it occurs on the two main diagonal planes. A general observation is extrapolated through the subsidence of different configurations: specimens failed by the emergence of diagonal shear planes, the orientation of which is dependent on topology, but increasing strain rate did not alter this failure mechanism. The reason for the orientation of these shear planes was demonstrated by the numerical models that showed that stress is concentrated in struts connecting diagonally opposite corners of the structure, and when shear planes emerge, they are aligned to these most loaded struts. By implementing the second optimization process, only a few diameters are increased, so the geometries are similar to the uniform case. This implies small increases in mass, but still higher values of energy absorption. In terms of failure modes, however, these show analogous behavior. On the other hand, when the experimental compression tests are performed on the BCC1 and BCCZ1 specimens they change enormously.

	$\epsilon \simeq 0\%$	$\epsilon \simeq 50\%$	$\epsilon \simeq 70\%$
<b>BCC - UNIFORM</b>			
<b>BCC - GRADED BY PROCESS 1</b>			
<b>BCC - GRADED BY PROCESS 2</b>			
<b>BCCZ - UNIFORM</b>			
<b>BCCZ - GRADED BY PROCESS 1</b>			
<b>BCCZ - GRADED BY PROCESS 2</b>			

*Table 6.5: Failure mode of specimens during static compression tests.*

As shown in Table 6.5 for the BCC specimens optimized through Process 1, four diagonal centerline planes are outlined during initial loading. After about the 50% of the loading, sequential layer-by-layer collapse begins. This implies multi-peak stress-strain curves and a less extensive plateau region. The stress values are found to be higher, so the increase in the energy absorption is justified. For BCCZ1 specimens, no preferential diagonal planes of failure are delineated, but collapse occurs directly layer by layer, generating larger increases in stiffness, stress and energy. BCC specimens failed at greater strains than their z-strut counterparts, and behaved in a bending-dominated manner, consistent with previous studies [32] and [31]. This suggests that the inclusion of z-struts increases strength and stiffness. The macro-behavior of the optimized specimens (graded BCC1, BCC2, BCCZ1 and BCCZ2 samples) therefore exhibits failure modes discussed in detail in the introduction to Chapter 4, which is in line with the analyses found in the literature ([57], [13]). This has led to enhanced energy absorption characteristics. In contrast to the uniformly dense lattice structures, those with graded density collapse in a layer-by-layer sequence, which is evident from the trends of the stress-strain curve.

## 6.9 Overall comparative analysis of the results

The ultimate aim of the experimental campaign was to confirm the data obtained through thickness optimization using the Matlab code, which significantly reduced the computational costs of analysis. A further objective was to verify the correctness and true correspondence of the analysis carried out using Ansys software, in which a series of approximations were made from the bilinear model assumed for the material (AlSi10Mg), geometric and numerical, producing a one-dimensional mesh with beam elements that was sufficiently coarse to reduce calculation times. The recreated structures have numerous advantages, including a significant increase in energy absorption values. This introduced an increment in mass, but also established excellent results considering the variations in failure modes. They changed from single-plane or diagonal multi-plane failures to a layer-by-layer collapse. These gains, provided by the models subjected to optimization of the diameters for each component cell of the specimen, were also revealed through the experimental static compression tests. They have been highlighted through the extrapolation of all relevant data in the previous paragraphs, but it is of interest to emphasize and directly compare masses and energy absorption with the values and trends obtained numerically. For the values of the masses of each specimen, it is necessary to refer to the Table [6.6](#). These values are fully comparable, possible variations in experimental data are justifiable by the approximations assumed in the material model in numerical analyses, by errors made during the 3D printing production process and during the post-processing phase. As an example, in the grinding phase, the size of 30 mm was reached by manually sanding the excess printed layers to ensure dimensional correctness and excellent surface finish. These design and construction choices largely explain the minimal deviations shown in Table [6.6](#) and [6.7](#), in which the value of the specific energy absorption is obtained by dividing the EA value by the mass.

	MASS [g]		
	Ansysis analysis	Matlab code	Experimental tests
<b>BCC</b>	5.9889	5.9889	5.9492
<b>BCC1</b>	15.1392	14.9407	15.0691
<b>BCC2</b>	6.7487	6.3072	6.4577
<b>BCCZ</b>	7.0349	7.0349	6.6740
<b>BCCZ1</b>	14.8125	14.045	14.5613
<b>BCCZ2</b>	7.1041	7.3499	7.0814

Table 6.6: Values of specimen mass obtained using Ansysis, Matlab code and experimental tests.

	SEA [mJ/g]		
	Ansysis analysis	Matlab code	Experimental tests
<b>BCC</b>	113.9907	113.9907	227.4227
<b>BCC1</b>	183.8830	184.7700	410.9877
<b>BCC2</b>	121.9846	126.2632	257.9249
<b>BCCZ</b>	477.0255	477.0348	562.7412
<b>BCCZ1</b>	672.4704	708.6015	794.7331
<b>BCCZ2</b>	523.0257	537.3127	646.4311

Table 6.7: SEA obtained using Ansysis, Matlab code and experimental tests.

	VEA [ $mJ/mm^3$ ]		
	Ansysis analysis	Matlab code	Experimental tests
<b>BCC</b>	0.0253	0.0253	0.0501
<b>BCC1</b>	0.0691	0.068	0.2294
<b>BCC2</b>	0.0281	0.0295	0.0617
<b>BCCZ</b>	0.1243	0.1243	0.1391
<b>BCCZ1</b>	0.2694	0.2741	0.2679
<b>BCCZ2</b>	0.1433	0.1463	0.1695

Table 6.8: VEA obtained using Ansysis, Matlab code and experimental tests.

As can be deduced from the Tables [6.6](#), [6.7](#) and [6.8](#), there is an almost perfect match for mass, but larger deviations for volumetric and specific energy absorption values. This is justified, as seen above, by the approximations assumed. It should be noted that the orders of magnitude remain comparable, so the validation of the results obtained in the previous chapters is carried

out. It is further necessary to examine that the trends remain the same for the three cases of analysis conducted. This can be appreciated with reference to the proposed histograms:

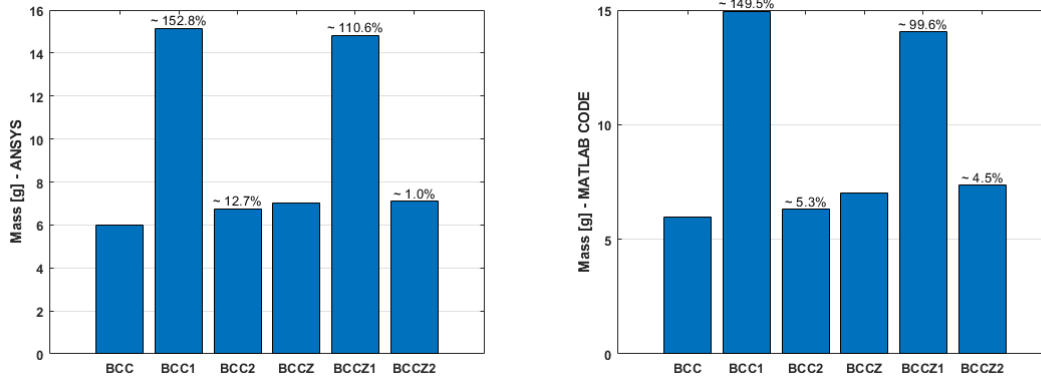


Figure 6.27: Mass values for all the configurations.

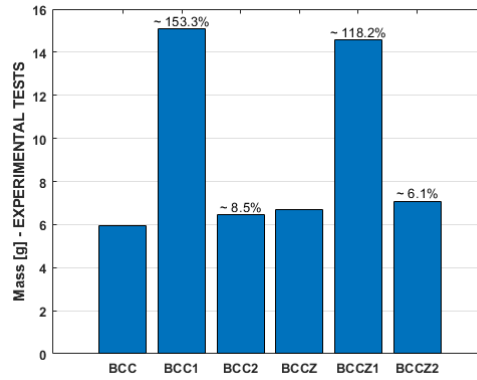


Figure 6.28: Mass values for all the configurations.

The highest increases in mass are recorded for specimens subjected to the optimization with process 1, for both BCC and BCCZ configurations. Process 2 leads to small increments, but still with better energy absorption values. This is evidenced by the trends of SEA and VEA, exactly the same for each analysis conducted. They highlight that the configuration with z-struts (BCCZ) is the best performing in general. This structures exhibit stretch-dominated behaviour and are stronger and stiffer, requiring greater loads to cause yielding and deformation. The deformation of Z-struts lattice samples progresses by buckling of vertical struts progressively along the vertical direction, together with development of plastic hinges near the interconnection regions between struts and nodes. The introduction of vertical struts lead to higher elastic modulus, 0.2% yield strength, steeper stress-strain slope and higher compressive strengths in

plastic deformation regime, with more efficient values of specific energy absorption, as revealed in [69]. Just in terms of SEA trends, the best candidate remains BCCZ1 (optimized by code 1), with excellent values also for process 2, which allows minimal mass increase. There are lower amounts for BCCs, but they follow the same tendencies as BCCZs.

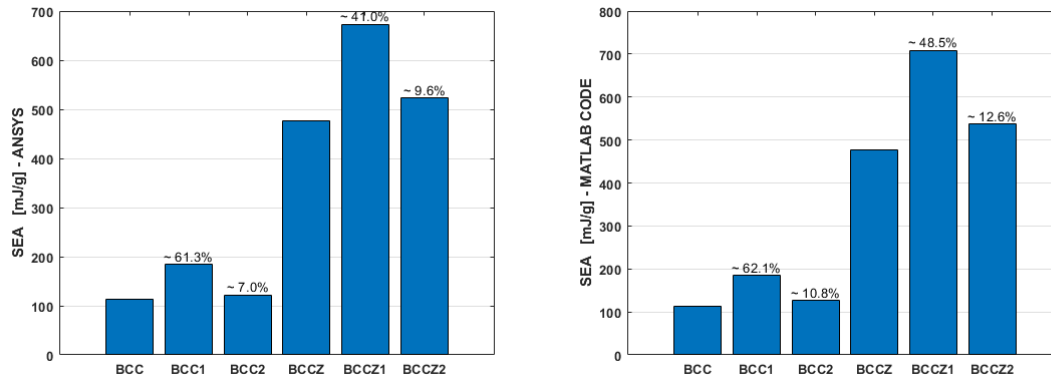


Figure 6.29: SEA values for all the configurations.

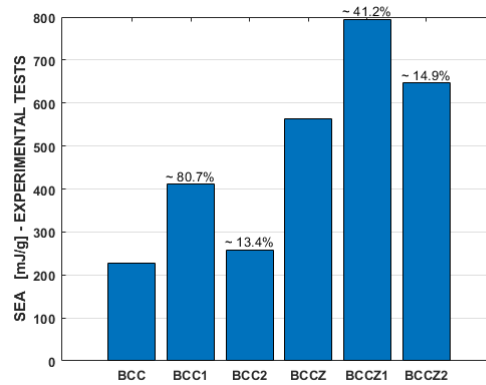


Figure 6.30: SEA values for all the configurations.

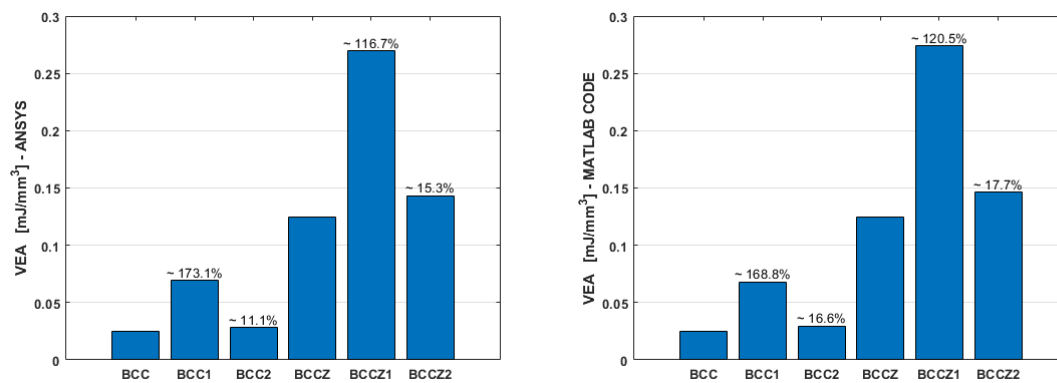


Figure 6.31: VEA values for all the configurations.

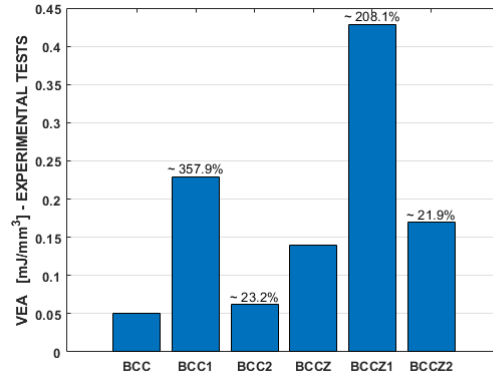


Figure 6.32: VEA values for all the configurations.

The values of volumetric energy absorption VEA, show higher levels for BCC1, obtained from the experimental campaign, with a greater deviation from the other measured data. Not considering the masses involved, BCC1 predicts excellent performance. This underlines how much geometric diversification and optimization affect the performance of lattice structures.

A further macro consideration on the results and comparisons is of a general nature: experimental tests provide a broader correspondence with the values recorded by software for specimens with z-struts (BCCZ). This could be explained by a higher-performance printing process when introducing such additional structural parts, or by the nature and characteristics they exhibit. Showing greater stiffness, they will tend to yield for higher load levels, avoiding drastic deformations as in the case of BCC samples. Therefore, the effects neglected within the analyses via Ansys and through the Matlab code, will not be affected by approximations related to overlooking edge deformation effects, that are not considered for the other configurations. Although there are not exactly matching values, by referring to the trends and percentage shown within the histograms, a perfect correspondence can be appreciated. This amply validates the results obtained in Chapter 5, making it possible to highlight not only how acceptable all the simplified assumptions, adopted for analysis via Ansys, are, but also how the code implemented in Matlab allows to obtain realistic outputs even experimentally, with minimal costs and computational time.



# Chapter 7

## Conclusions

The analyses performed in this thesis demonstrated successfully the potential of structural optimization techniques to accomplish innovative lightweight designs with improved performance. The opening chapters of the thesis highlighted the basic aspects of different specimens, outlining the main differences obtained from the application of a variety of elementary cells and different dimensions. These initial analyses made it possible to recognize the fundamental characteristics, laying the basis for implementing two different optimization processes (seen in Chapters 4 and 5). Lattice structures are destined to appear increasingly frequently in future designs due to the growing field of additive manufacturing (AM) and the constant desire to reduce weight. The successful implementation of lattice structures requires an adequate interpretation of the behaviour of cellular structures, which was done in this first part of the thesis. The analyses and optimization processes presented in the Chapter 5 can be an helpful accessory to quickly designing, analyzing, and improve lattices for compressively loaded components. The results identified new dimensional assignments to increase the energy absorption levels of the configurations of interest. It was validated by the experimental campaign (Chapter 6), which confirmed that the BCC and BCCZ configurations produce strong improvements as the thicknesses of the individual struts changed. With reference to the experimental data, it can be seen that the optimization carried out led to increases of up to 80% and 40% in terms of specific and volumetric absorption energy, for the BCC1 configuration. This requires a significant increase in weight, but lays the foundations for a promising methodology, which, although it involves improvements, generates enormous energy benefits. Of the two processes examined, for the former, the increase in energy absorption was highlighted, at the expense of the addition in weight, while for the latter, the preference was for maintaining the mass

within a reduced range, resulting in lower percentages with regard to energy performance. Consequently, the choice of the best specimen depends on a trade-off between mechanical characteristics, energy and mass increments. This is determined against the specific application, so each candidate examined is the optimum, based on the desired applied context. An advantageous example of possible future application finds in Process 1 the best choice for implementations as sacrificially energy-absorbing layers in protection systems against projectiles or fragments, high energy events (crash or a blast), micrometeoroid and orbital debris (MMODs) for the space field. Regarding the results obtained from the implementation of Process 2, it can be stated that such architectures are most cost-effective where the lightweight aspect is prioritized, thus falling into applications such as bio-medical or aerospace detailing. In comparison to the uniform lattice structure, the optimized lattice samples exhibit superior energetic performance, as calculated by Matlab code, Ansys and finally confirmed by static compression tests. A further goal achieved was not only the search for effective optimization methods, but at the same time an additional benefit lies in the code itself. This, as shown in the Section 5.5, allowed to obtain the outputs (Von-Mises stress, EA, SEA and VEA) in times of the order of a minute, significantly shorter than those of the Ansys software (in the order of hours). This is a great advantage since these properties can be predicted saving on time and computational costs, providing minimal deviations (see Section 5.4).

Future research could be focused on the possibility to introduce a smaller low limit of the struts' thickness, in order to further improve the performance and reduce the weight. An additional limitation to be overcome lies in the handling of the Matlab code, which required input '.out' files from Ansys Workbench, containing the identifications of the geometric entities and stress values. These files were imported into the Matlab environment, but post-optimization, once the diameters had changed, it was not possible to input these directly into Ansys, which had to be modelled manually. This process required very large process times to perform the validations, which could be reduced by allowing the code to communicate more directly with the software, making the process more automated. Furthermore, only two different topologies were implemented within the optimization processes, so the future aim could be the validation of the results obtained for the FCC, FCCZ, FBCC and FBCCZ configurations.

# Bibliography

- [1] W. Tao and M. C. Leu, “Design of lattice structure for additive manufacturing,” in *2016 International Symposium on Flexible Automation (ISFA)*, pp. 325–332, IEEE, 2016.
- [2] M. F. A. L. J. Gibson, *Cellular solids: Structure and Properties*. 2nd edition, Cambridge University Press, Cambridge UK, 1997.
- [3] G. Dong, D. Tessier, and Y. F. Zhao, “Design of shoe soles using lattice structures fabricated by additive manufacturing,” in *Proceedings of the Design Society: International Conference on Engineering Design*, vol. 1, pp. 719–728, Cambridge University Press, 2019.
- [4] T. Maconachie, R. Tino, B. Lozanovski, M. Watson, A. Jones, C. Pandelidi, A. Alghamdi, A. Almalki, D. Downing, M. Brandt, *et al.*, “The compressive behaviour of abs gyroid lattice structures manufactured by fused deposition modelling,” *The International Journal of Advanced Manufacturing Technology*, vol. 107, no. 11, pp. 4449–4467, 2020.
- [5] T. Maconachie, M. Leary, B. Lozanovski, X. Zhang, M. Qian, O. Faruque, and M. Brandt, “Slm lattice structures: Properties, performance, applications and challenges,” *Materials & Design*, vol. 183, p. 108137, 2019.
- [6] M. Helou and S. Kara, “Design, analysis and manufacturing of lattice structures: an overview,” *International Journal of Computer Integrated Manufacturing*, vol. 31, no. 3, pp. 243–261, 2018.
- [7] G. D. Pasquale and A. Tagliaferri, “Modeling and characterization of mechanical and energetic elastoplastic behavior of lattice structures for aircrafts anti-icing systems,” *Proceedings of the Institution of Mechanical Engineers, Part C: Journal of Mechanical Engineering Science*, vol. 235, no. 10, pp. 1828–1839, 2021.
- [8] <http://blog.csiro.au/cancer-patient-receives-3d-printed-ribs-in-world-first-surgery/>.

- [9] K. J. Maloney, K. D. Fink, T. A. Schaedler, J. A. Kolodziejska, A. J. Jacobsen, and C. S. Roper, "Multifunctional heat exchangers derived from three-dimensional micro-lattice structures," *International Journal of Heat and Mass Transfer*, vol. 55, no. 9-10, pp. 2486–2493, 2012.
- [10] A. Coluccia, G. De Pasquale, G. Meyer, and C. Mittelstedt, "Modeling of lattice structures energy absorption under impact loads," in *2021 12th International Conference on Mechanical and Aerospace Engineering (ICMAE)*, pp. 494–499, IEEE, 2021.
- [11] G. Jiang, *Modelling and simulation of lattice structures with different aspect ratios*. <https://webthesis.biblio.polito.it/20071/>, 2021.
- [12] T. Maconachie, M. Leary, P. Tran, J. Harris, Q. Liu, G. Lu, D. Ruan, O. Faruque, and M. Brandt, "The effect of topology on the quasi-static and dynamic behaviour of slm alsi10mg lattice structures," *The International Journal of Advanced Manufacturing Technology*, vol. 118, no. 11, pp. 4085–4104, 2022.
- [13] I. Maskery, N. Aboulkhair, A. Aremu, C. Tuck, I. Ashcroft, R. D. Wildman, and R. Hague, "A mechanical property evaluation of graded density al-si10-mg lattice structures manufactured by selective laser melting," *Materials Science and Engineering: A*, vol. 670, pp. 264–274, 2016.
- [14] H. Lei, C. Li, X. Zhang, P. Wang, H. Zhou, Z. Zhao, and D. Fang, "Deformation behavior of heterogeneous multi-morphology lattice core hybrid structures," *Additive Manufacturing*, vol. 37, p. 101674, 2021.
- [15] D. Stamenovic and N. Wang, "Invited review: engineering approaches to cytoskeletal mechanics," *Journal of Applied Physiology*, vol. 89, no. 5, pp. 2085–2090, 2000.
- [16] M. R. Mofrad and R. D. Kamm, *Cytoskeletal mechanics: models and measurements in cell mechanics*. Cambridge University Press, 2006.
- [17] J. D. Deaton and R. V. Grandhi, "A survey of structural and multidisciplinary continuum topology optimization: post 2000," *Structural and Multidisciplinary Optimization*, vol. 49, no. 1, pp. 1–38, 2014.

- [18] A. Seharing, A. H. Azman, and S. Abdullah, "Finite element analysis of gradient lattice structure patterns for bone implant design," *International Journal of Structural Integrity*, vol. 11, no. 4, pp. 535–545, 2020.
- [19] C. Beyer and D. Figueroa, "Design and analysis of lattice structures for additive manufacturing," *Journal of Manufacturing Science and Engineering*, vol. 138, no. 12, 2016.
- [20] A. Beharic, R. R. Egui, and L. Yang, "Drop-weight impact characteristics of additively manufactured sandwich structures with different cellular designs," *Materials & Design*, vol. 145, pp. 122–134, 2018.
- [21] Z. Xiao, Y. Yang, R. Xiao, Y. Bai, C. Song, and D. Wang, "Evaluation of topology-optimized lattice structures manufactured via selective laser melting," *Materials & Design*, vol. 143, pp. 27–37, 2018.
- [22] V. S. Deshpande, N. A. Fleck, and M. F. Ashby, "Effective properties of the octet-truss lattice material," *Journal of the Mechanics and Physics of Solids*, vol. 49, no. 8, pp. 1747–1769, 2001.
- [23] M. Leary, M. Mazur, H. Williams, E. Yang, A. Alghamdi, B. Lozanovski, X. Zhang, D. Shidid, L. Farahbod-Sternahl, G. Witt, *et al.*, "Inconel 625 lattice structures manufactured by selective laser melting (slm): Mechanical properties, deformation and failure modes," *Materials & Design*, vol. 157, pp. 179–199, 2018.
- [24] G. De Pasquale, F. Luceri, and M. Riccio, "Experimental characterization of slm and ebm cubic lattice structures for lightweight applications," *Experimental Mechanics*, vol. 59, no. 4, pp. 469–482, 2019.
- [25] G. De Pasquale and F. Luceri, "Experimental validation of ti6al4v bio-inspired cellular structures from additive manufacturing processes," *Materials Today: Proceedings*, vol. 7, pp. 566–571, 2019.
- [26] G. De Pasquale and S. Sibona, "Hybrid materials based on polymers-filled am steel lattices with energy absorption capabilities," *Mechanics of Advanced Materials and Structures*, vol. 29, no. 18, pp. 2570–2580, 2022.

- [27] J. Harris, R. Winter, and G. McShane, “Impact response of additively manufactured metallic hybrid lattice materials,” *International Journal of Impact Engineering*, vol. 104, pp. 177–191, 2017.
- [28] J. Souza, A. Großmann, and C. Mittelstedt, “Micromechanical analysis of the effective properties of lattice structures in additive manufacturing,” *Additive Manufacturing*, vol. 23, pp. 53–69, 2018.
- [29] R. Alberdi, R. Dingreville, J. Robbins, T. Walsh, B. C. White, B. Jared, and B. L. Boyce, “Multi-morphology lattices lead to improved plastic energy absorption,” *Materials & Design*, vol. 194, p. 108883, 2020.
- [30] C. Yan, L. Hao, A. Hussein, and D. Raymont, “Evaluations of cellular lattice structures manufactured using selective laser melting,” *International Journal of Machine Tools and Manufacture*, vol. 62, pp. 32–38, 2012.
- [31] M. Leary, M. Mazur, J. Elambasseril, M. McMillan, T. Chirent, Y. Sun, M. Qian, M. Easton, and M. Brandt, “Selective laser melting (slm) of als12mg lattice structures,” *Materials & Design*, vol. 98, pp. 344–357, 2016.
- [32] M. Mazur, M. Leary, M. McMillan, S. Sun, D. Shidid, and M. Brandt, *Mechanical properties of Ti6Al4V and AlSi12Mg lattice structures manufactured by Selective Laser Melting (SLM)*.
- [33] T. A. Schaedler, A. J. Jacobsen, A. Torrents, A. E. Sorensen, J. Lian, J. R. Greer, L. Valdevit, and W. B. Carter, “Ultralight metallic microlattices,”
- [34] L. Hao, D. Raymont, C. Yan, A. Hussein, and P. Young, “Design and additive manufacturing of cellular lattice structures,” in *The International Conference on Advanced Research in Virtual and Rapid Prototyping (VRAP)*. Taylor & Francis Group, Leiria, pp. 249–254, 2011.
- [35] C. Liu, Z. Du, W. Zhang, Y. Zhu, and X. Guo, “Additive manufacturing-oriented design of graded lattice structures through explicit topology optimization,” *Journal of Applied Mechanics*, vol. 84, no. 8, 2017.
- [36] M. F. Ashby and R. Medalist, “The mechanical properties of cellular solids,” *Metallurgical Transactions A*, vol. 14, no. 9, pp. 1755–1769, 1983.

- [37] M. Bici, S. Brischetto, F. Campana, C. G. Ferro, C. Seclì, S. Varetti, P. Maggiore, and A. Mazza, “Development of a multifunctional panel for aerospace use through slm additive manufacturing,” *Procedia Cirp*, vol. 67, pp. 215–220, 2018.
- [38] D. L. Miller, G. Kersten, and W. A. Frost, “Systems and methods for protecting a flight recorder,” May 13 2014. US Patent 8,723,057.
- [39] B. Aslan and A. R. Yıldız, “Optimum design of automobile components using lattice structures for additive manufacturing,” *Materials testing*, vol. 62, no. 6, pp. 633–639, 2020.
- [40] G. De Pasquale, E. Bertuccio, M. Montemurro, and A. Catapano, “Modeling of cellular structures under static and fatigue loads,” in *II International Conference on Simulation for Additive Manufacturing-Sim-AM*, 2019.
- [41] A. Fiorentino, G. Zarattini, U. Pazzaglia, and E. Ceretti, “Hip prosthesis design. market analysis, new perspectives and an innovative solution,” *Procedia Cirp*, vol. 5, pp. 310–314, 2013.
- [42] P. S. Ginestra, E. Ceretti, and A. Fiorentino, “Potential of modeling and simulations of bioengineered devices: Endoprostheses, prostheses and orthoses,” *Proceedings of the Institution of Mechanical Engineers, Part H: Journal of Engineering in Medicine*, vol. 230, no. 7, pp. 607–638, 2016.
- [43] M. P. Bendsøe and N. Kikuchi, “Generating optimal topologies in structural design using a homogenization method,” *Computer methods in applied mechanics and engineering*, vol. 71, no. 2, pp. 197–224, 1988.
- [44] M. P. Bendsøe and O. Sigmund, “Material interpolation schemes in topology optimization,” *Archive of applied mechanics*, vol. 69, no. 9, pp. 635–654, 1999.
- [45] M. Y. Wang, X. Wang, and D. Guo, “A level set method for structural topology optimization,” *Computer methods in applied mechanics and engineering*, vol. 192, no. 1-2, pp. 227–246, 2003.
- [46] X. Guo, W. S. Zhang, M. Y. Wang, and P. Wei, “Stress-related topology optimization via level set approach,” *Computer Methods in Applied Mechanics and Engineering*, vol. 200, no. 47-48, pp. 3439–3452, 2011.

- [47] W. S. Zhang, X. Guo, M. Y. Wang, and P. Wei, "Optimal topology design of continuum structures with stress concentration alleviation via level set method," *International journal for numerical methods in engineering*, vol. 93, no. 9, pp. 942–959, 2013.
- [48] G. Meyer, K. Schelleis, O. Weeger, and C. Mittelstedt, "Tensile specimen design proposal for truss-based lattice structures," *Mechanics of Advanced Materials and Structures*, pp. 1–28, 2022.
- [49] A. Seharing, A. H. Azman, and S. Abdullah, "Systematic review: Overview on trends and future opportunities of additive manufactured lattice structures," in *Symposium on Damage Mechanism in Materials and Structures*, pp. 75–90, Springer, 2020.
- [50] C. Beyer and D. Figueroa, "Design and analysis of lattice structures for additive manufacturing," *Journal of Manufacturing Science and Engineering*, vol. 138, no. 12, 2016.
- [51] G. Meyer, J. Musekamp, F. Göbel, F. Gardian, and C. Mittelstedt, "Manufacturability investigation of inclined alsi10mg lattice struts by means of selective laser melting," *Manufacturing Letters*, vol. 31, pp. 101–105, 2022.
- [52] M. site:, <http://www.matweb.com>.
- [53] M. Smith, W. Cantwell, Z. Guan, S. Tsopanos, M. Theobald, G. Nurick, and G. Langdon, "The quasi-static and blast response of steel lattice structures," *Journal of Sandwich Structures & Materials*, vol. 13, no. 4, pp. 479–501, 2011.
- [54] M. Yoder, L. Thompson, and J. Summers, "Size effects in lattice structures and a comparison to micropolar elasticity," *International Journal of Solids and Structures*, vol. 143, pp. 245–261, 2018.
- [55] H. Fan, F. Jin, and D. Fang, "Characterization of edge effects of composite lattice structures," *Composites Science and Technology*, vol. 69, no. 11-12, pp. 1896–1903, 2009.
- [56] J. J. Andrew, J. Schneider, J. Ubaid, R. Velmurugan, N. Gupta, and S. Kumar, "Energy absorption characteristics of additively manufactured plate-lattices under low-velocity impact loading," *International Journal of Impact Engineering*, vol. 149, p. 103768, 2021.
- [57] D. S. Al-Saedi, S. Masood, M. Faizan-Ur-Rab, A. Alomarah, and P. Ponnusamy, "Mechanical properties and energy absorption capability of functionally graded f2bcc lattice fabricated by slm," *Materials & Design*, vol. 144, pp. 32–44, 2018.



- [58] R. Alberdi, R. Dingreville, J. Robbins, T. Walsh, B. C. White, B. Jared, and B. L. Boyce, "Multi-morphology lattices lead to improved plastic energy absorption," *Materials & Design*, vol. 194, p. 108883, 2020.
- [59] A. G. M. Michell, "The limits of economy of material in frame-structures," *The London, Edinburgh, and Dublin Philosophical Magazine and Journal of Science*, vol. 8, no. 47, pp. 589–597, 1904.
- [60] J.-H. Zhu, W.-H. Zhang, and L. Xia, "Topology optimization in aircraft and aerospace structures design," *Archives of Computational Methods in Engineering*, vol. 23, no. 4, pp. 595–622, 2016.
- [61] O. Sigmund and K. Maute, "Topology optimization approaches," *Structural and Multidisciplinary Optimization*, vol. 48, no. 6, pp. 1031–1055, 2013.
- [62] T. Zegard and G. H. Paulino, "Bridging topology optimization and additive manufacturing," *Structural and Multidisciplinary Optimization*, vol. 53, no. 1, pp. 175–192, 2016.
- [63] S. Daynes, S. Feih, W. F. Lu, and J. Wei, "Optimisation of functionally graded lattice structures using isostatic lines," *Materials & Design*, vol. 127, pp. 215–223, 2017.
- [64] S. Y. Choy, C.-N. Sun, K. F. Leong, and J. Wei, "Compressive properties of functionally graded lattice structures manufactured by selective laser melting," *Materials & Design*, vol. 131, pp. 112–120, 2017.
- [65] D. I. für Normung, *Prüfung von metallischen Werkstoffen - Druckversuch an metallischen zellularen Werkstoffen DIN 50134*. DIN Deutsches Institut für Normung e.V., 2008.
- [66] D. Li, R. Qin, J. Xu, B. Chen, and X. Niu, "Effect of heat treatment on alsi10mg lattice structure manufactured by selective laser melting: Microstructure evolution and compression properties," *Materials Characterization*, vol. 187, p. 111882, 2022.
- [67] *Undurchlässige Sintermetallwerkstoffe und Hartmetalle - Ermittlung der Dichte (iso 3369:2006); DIN EN ISO 3369:2010-08*.
- [68] H. Lei, C. Li, J. Meng, H. Zhou, Y. Liu, X. Zhang, P. Wang, and D. Fang, "Evaluation of compressive properties of slm-fabricated multi-layer lattice structures by experimental test and  $\mu$ -ct based finite element analysis," *Materials and Design*, vol. 169, p. 107685, 2019.

- [69] G. Wang, X. Chen, and C. Qiu, “On the macro-and micro-deformation mechanisms of selectively laser melted damage tolerant metallic lattice structures,” *Journal of Alloys and Compounds*, vol. 852, p. 156985, 2021.

# Appendix A

## Stress extraction in table format

### A.1 Initial uniform configuration

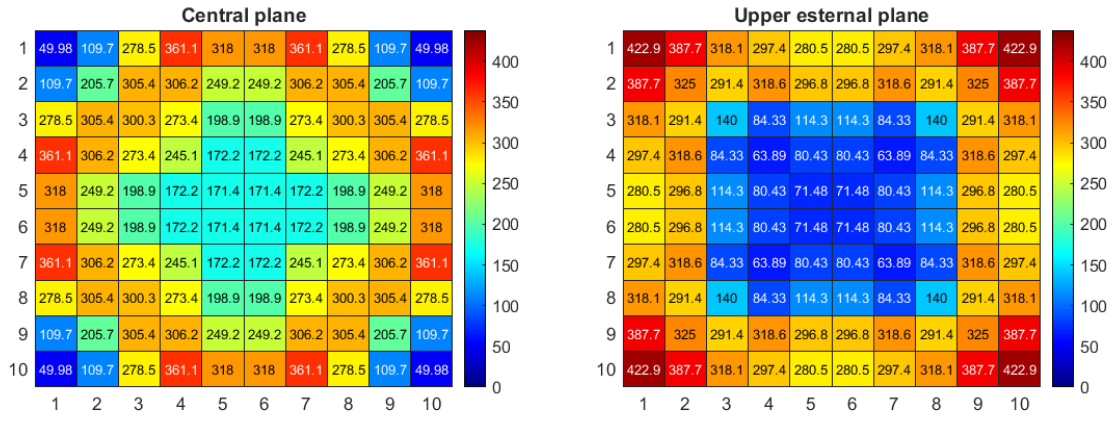


Figure A.1: Central plane (x,y) and upper plane (x,y) for BCC samples.

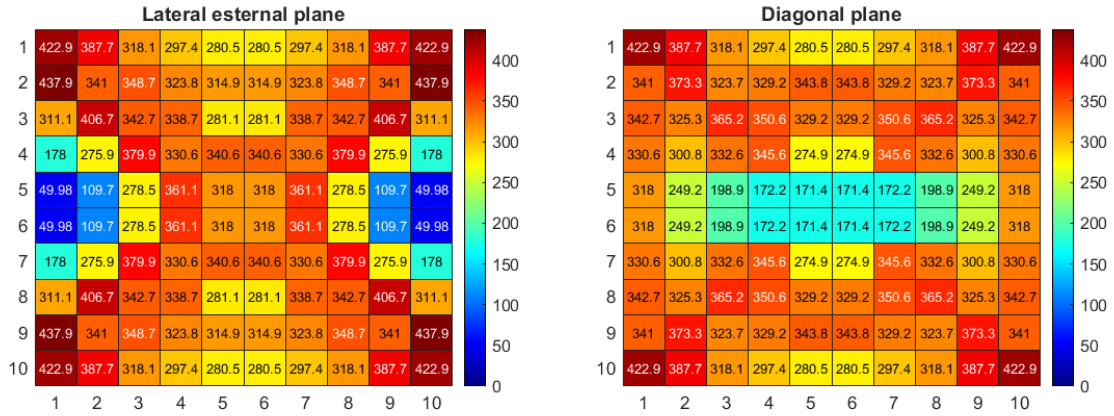


Figure A.2: Lateral external plane (y,z) and diagonal plane for BCC samples.

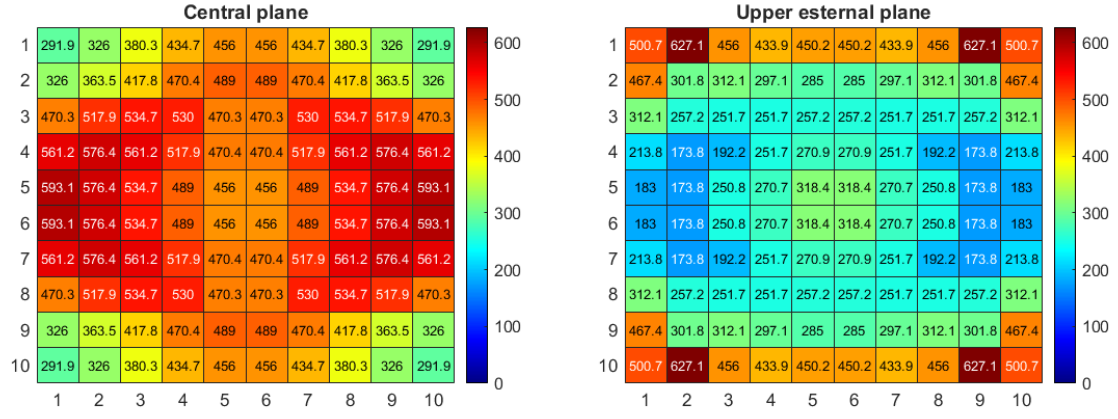


Figure A.3: Central plane (x,y) and upper plane (x,y) for BCCZ samples.

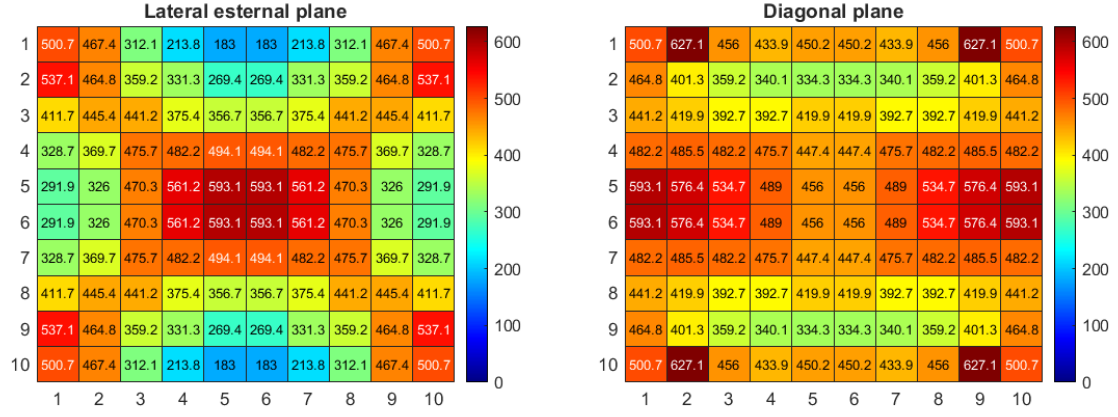


Figure A.4: Lateral external plane (y,z) and diagonal plane for BCCZ samples.

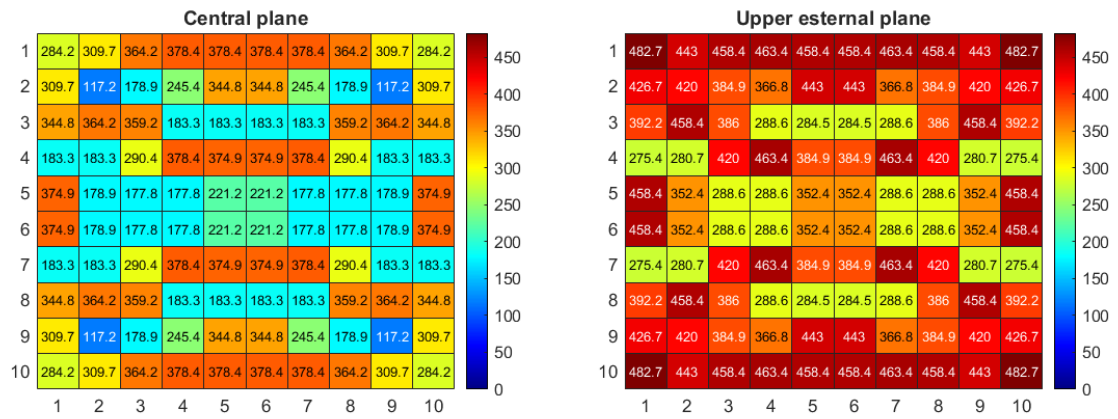


Figure A.5: Central plane (x,y) and upper plane (x,y) for FCC samples.

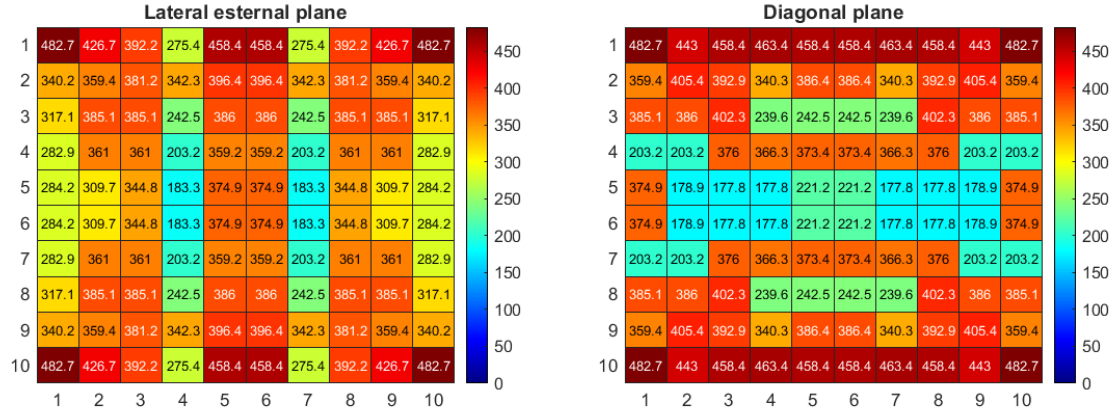


Figure A.6: Lateral external plane (y,z) and diagonal plane for FCC samples.

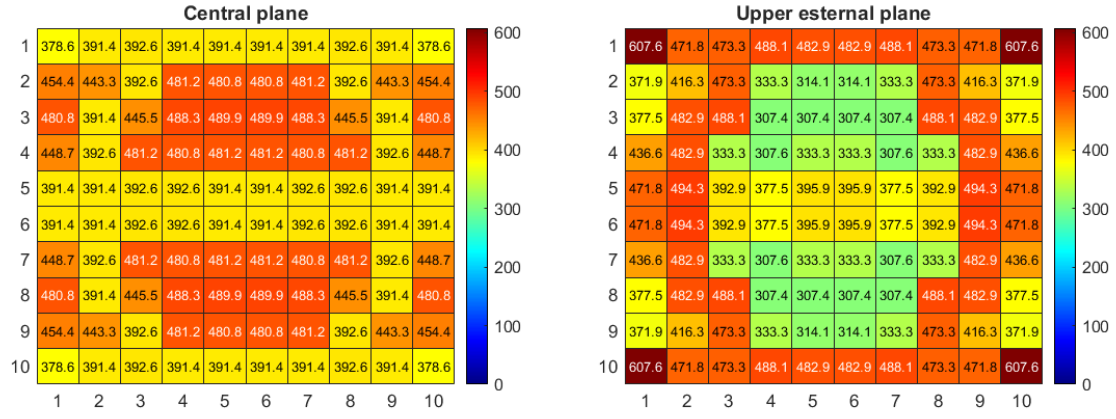


Figure A.7: Central plane (x,y) and upper plane (x,y) for FCCZ samples.

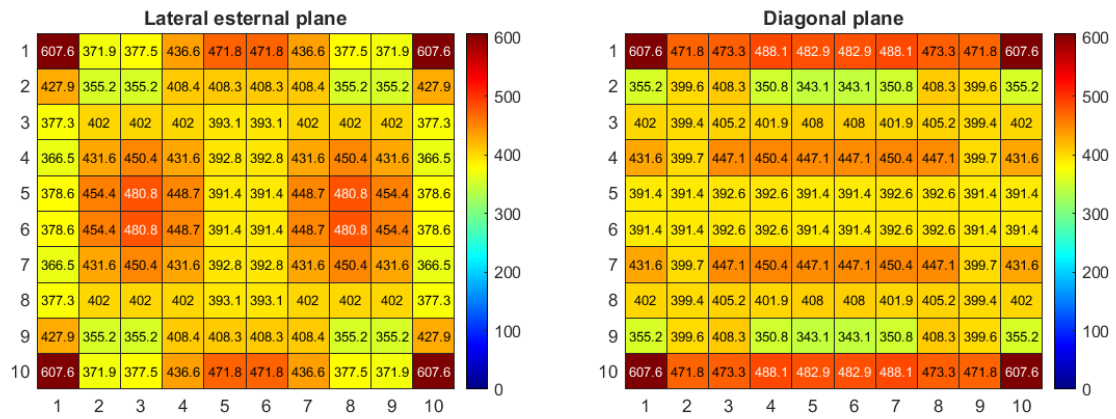


Figure A.8: Lateral external plane (y,z) and diagonal plane for FCCZ samples.

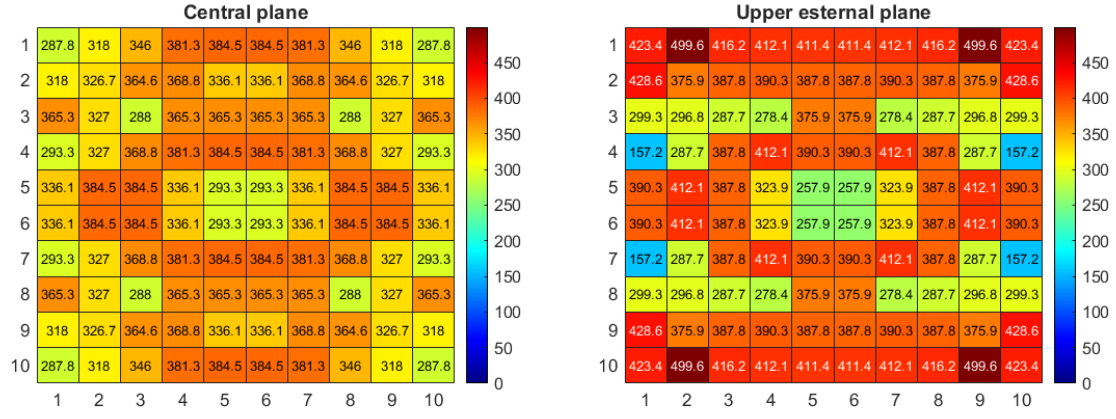


Figure A.9: Central plane (x,y) and upper plane (x,y) for FBCC samples.

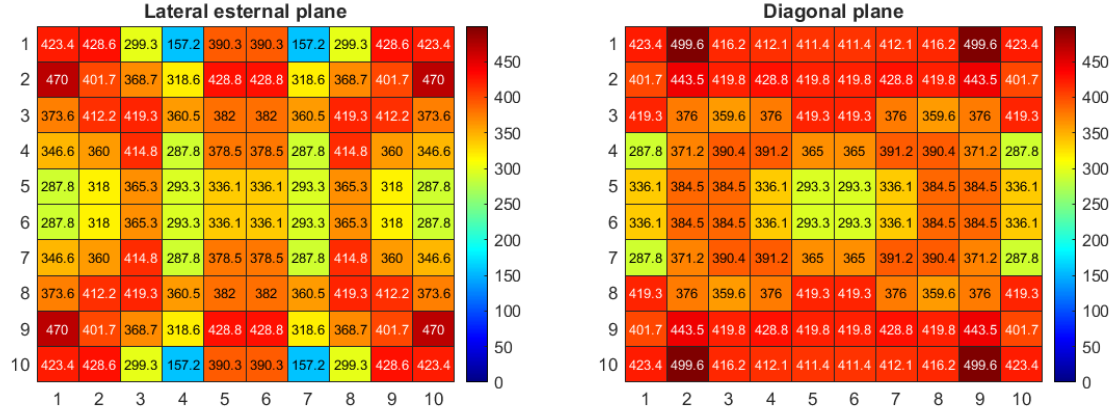


Figure A.10: Lateral external plane (y,z) and diagonal plane for FBCC samples.

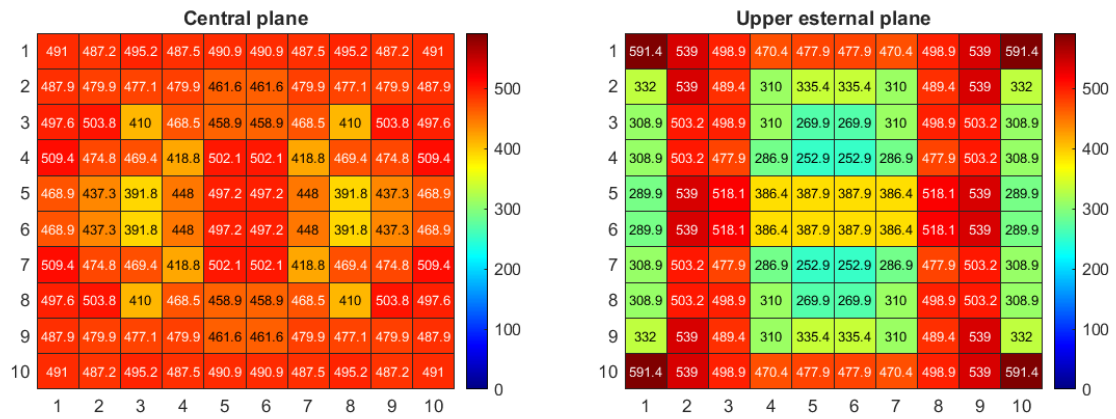


Figure A.11: Central plane (x,y) and upper plane (x,y) for FBCCZ samples.

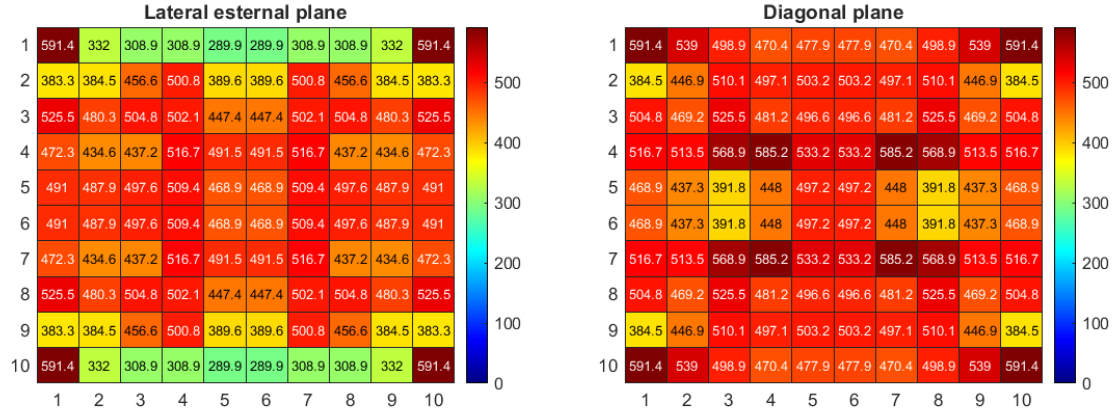


Figure A.12: Lateral external plane ( $y,z$ ) and diagonal plane for FBCCZ samples.

## A.2 Optimized samples

### A.2.1 Threshold equal to the mean value - Process 1 and 2

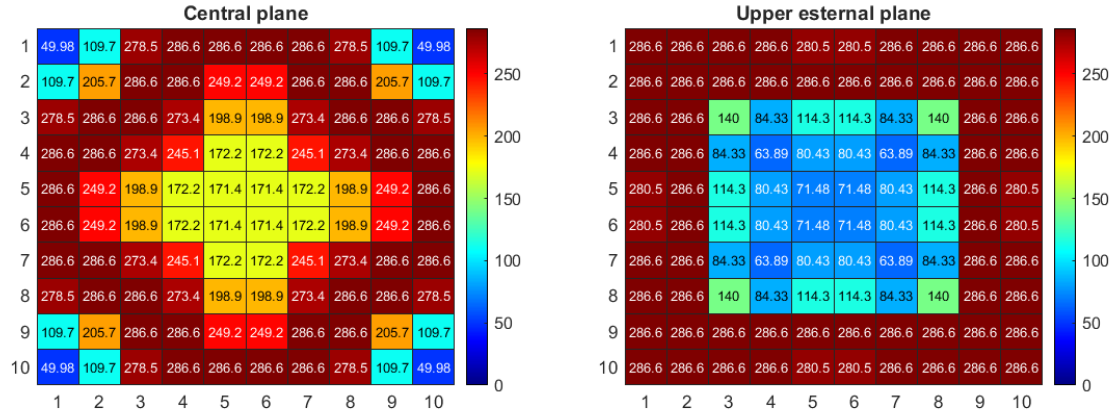


Figure A.13: Central plane ( $x,y$ ) and upper plane ( $x,y$ ) - BCC optimized sample.

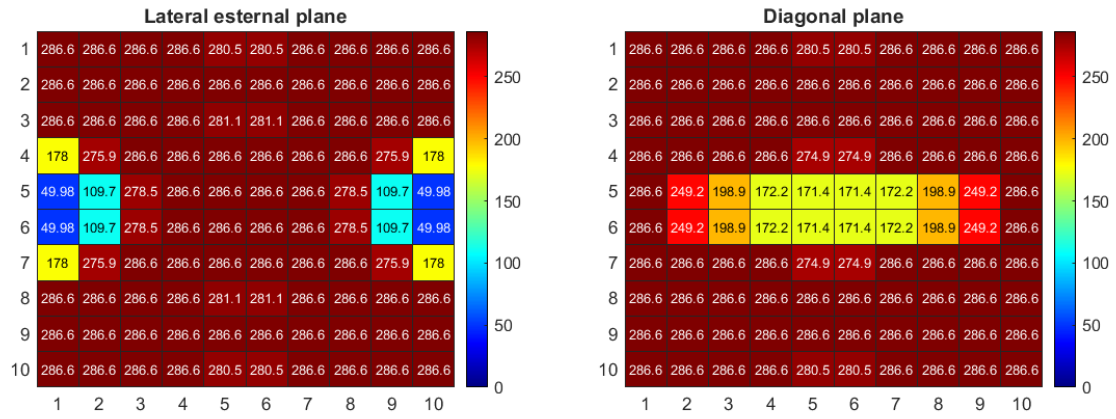


Figure A.14: Lateral external plane (y,z) and diagonal plane - BCC optimized sample.

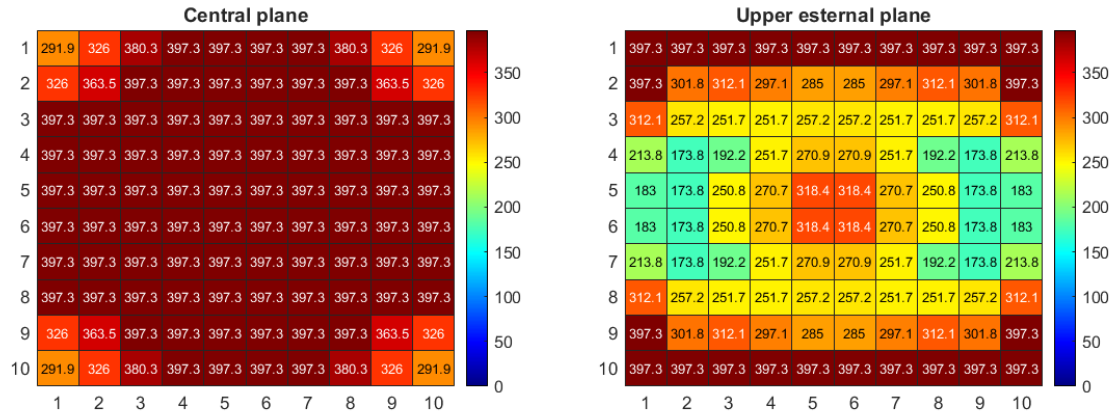


Figure A.15: Central plane (x,y) and upper plane (x,y) - BCCZ optimized sample.

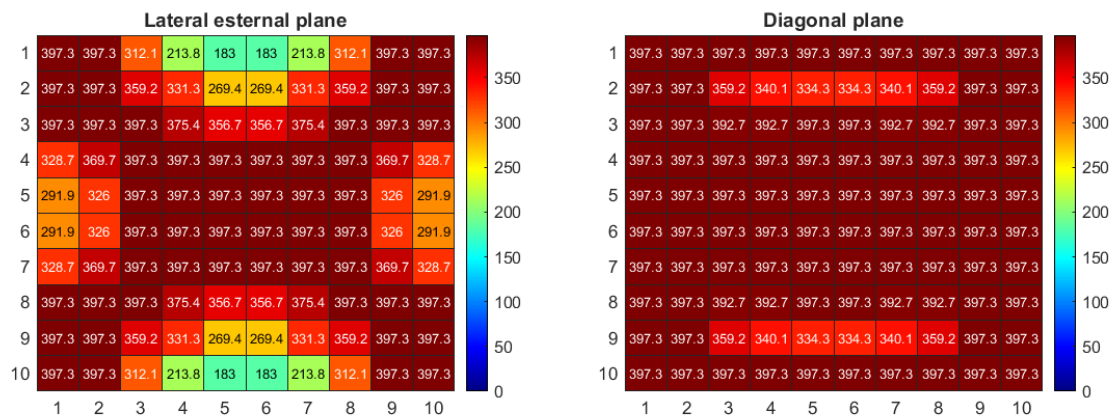


Figure A.16: Lateral external plane (y,z) and diagonal plane - BCCZ optimized sample.



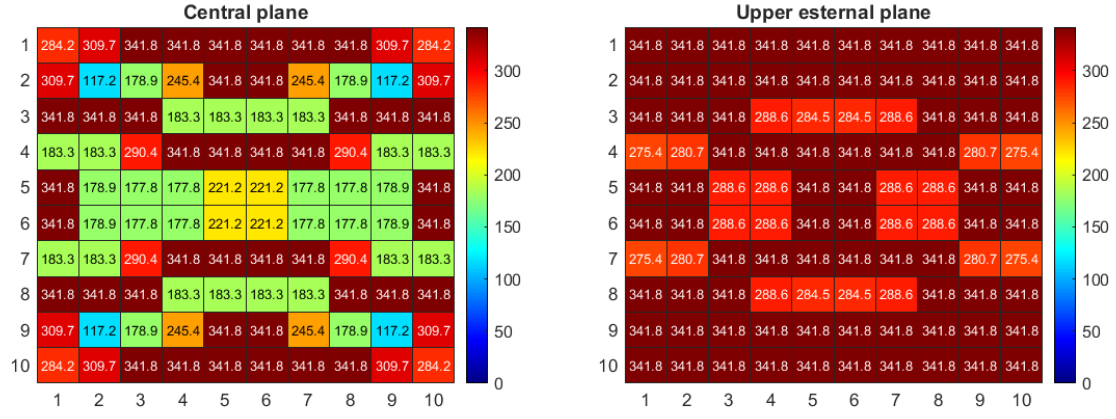


Figure A.17: Central plane (x,y) and upper plane (x,y) - FCC optimized sample.

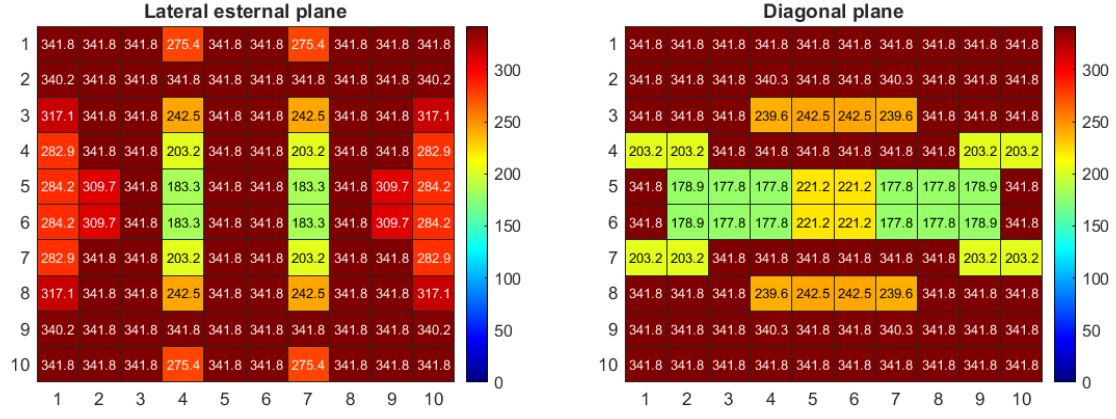


Figure A.18: Lateral external plane (y,z) and diagonal plane - FCC optimized sample.

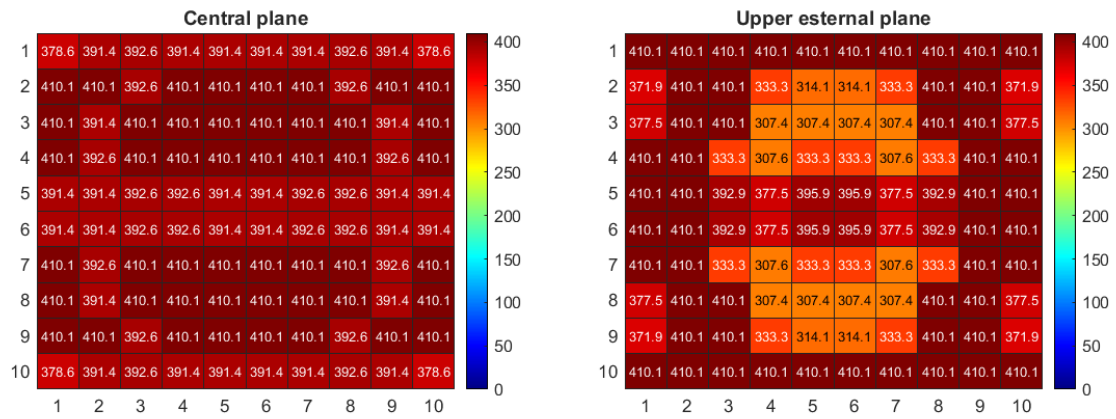


Figure A.19: Central plane (x,y) and upper plane (x,y) - FCCZ optimized sample.

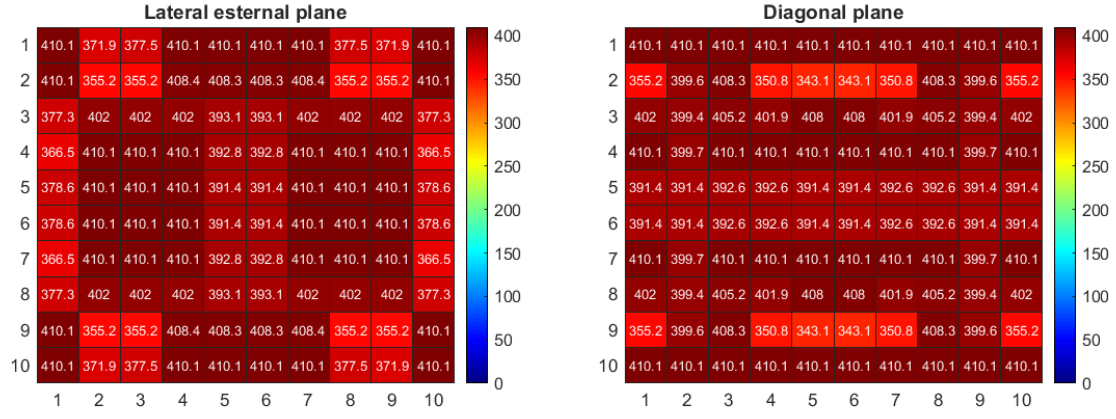


Figure A.20: Lateral external plane (y,z) and diagonal plane - FCCZ optimized sample.

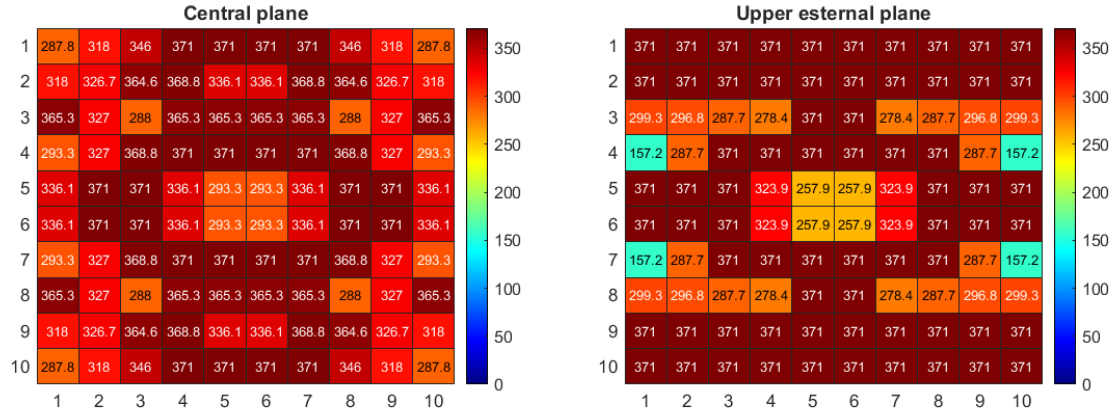


Figure A.21: Central plane (x,y) and upper plane (x,y) - FBCC optimized sample.

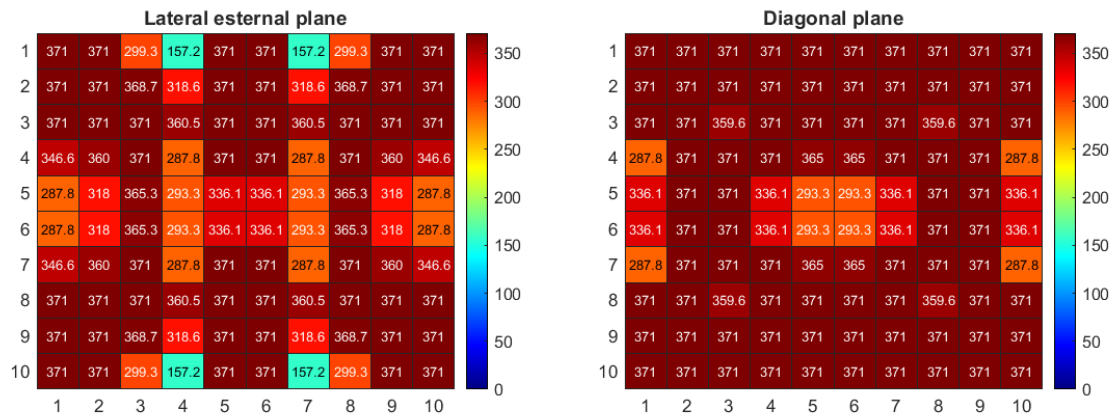


Figure A.22: Lateral external plane (y,z) and diagonal plane - FBCC optimized sample.

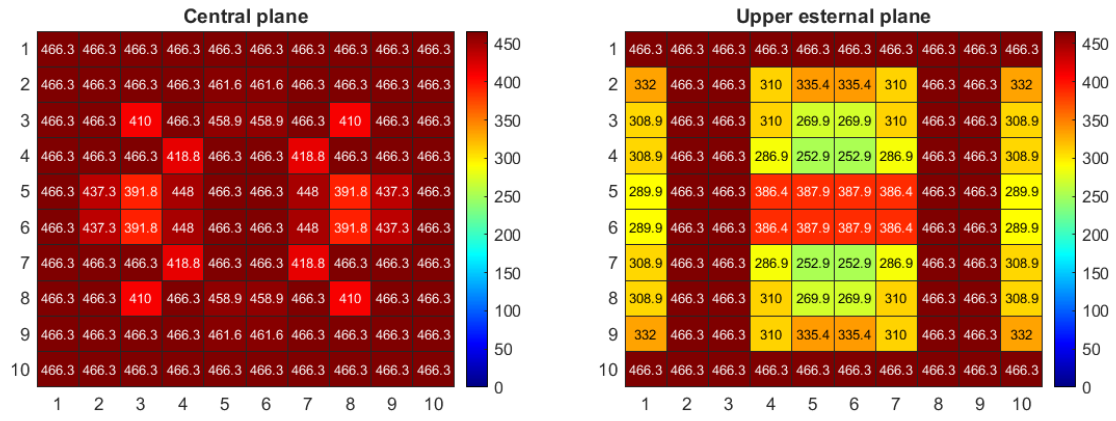


Figure A.23: Central plane (x,y) and upper plane (x,y) - FBCCZ optimized sample.

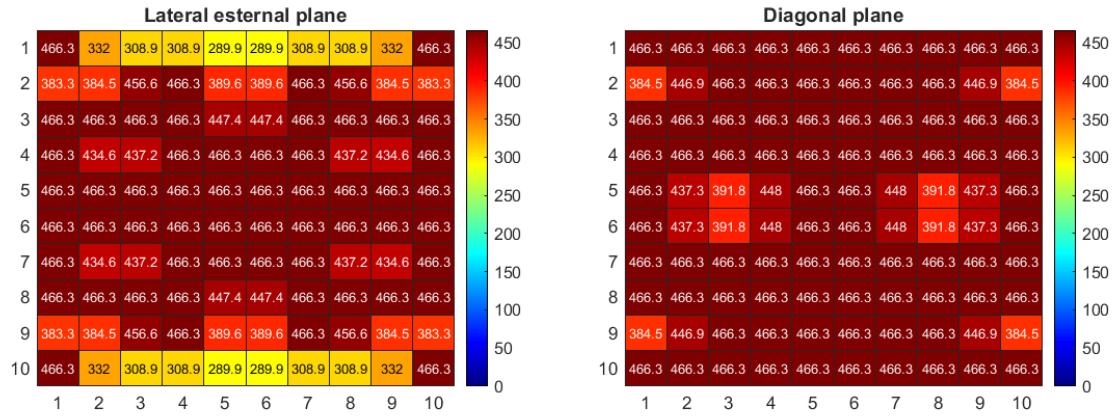


Figure A.24: Lateral external plane (y,z) and diagonal plane - FBCCZ optimized sample.

# Appendix B

## Optimized samples: new thicknesses extraction in table format

### B.1 Threshold equal to the mean value - Process 1

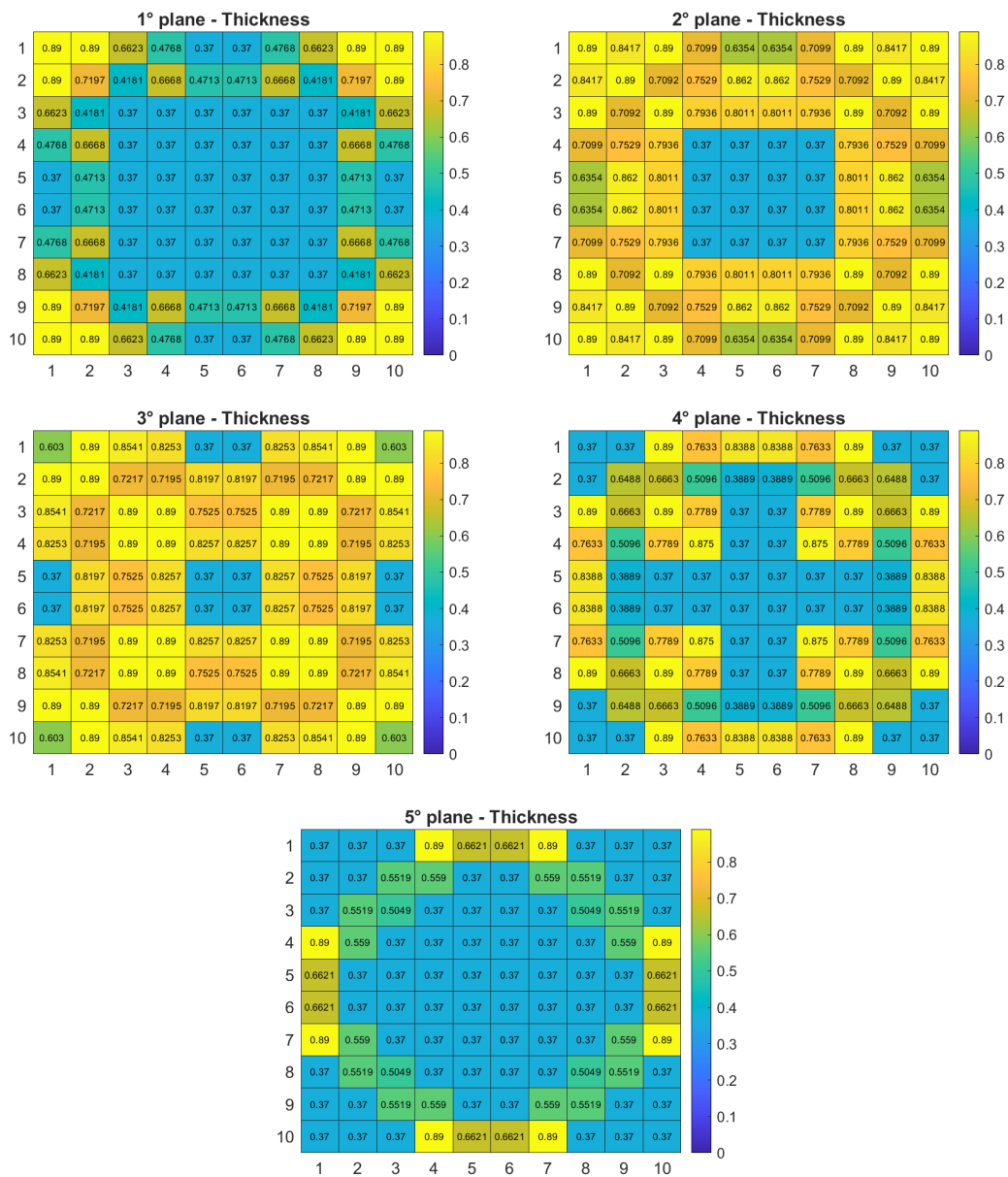


Figure B.1: Diameter of struts per cell - BCC1.

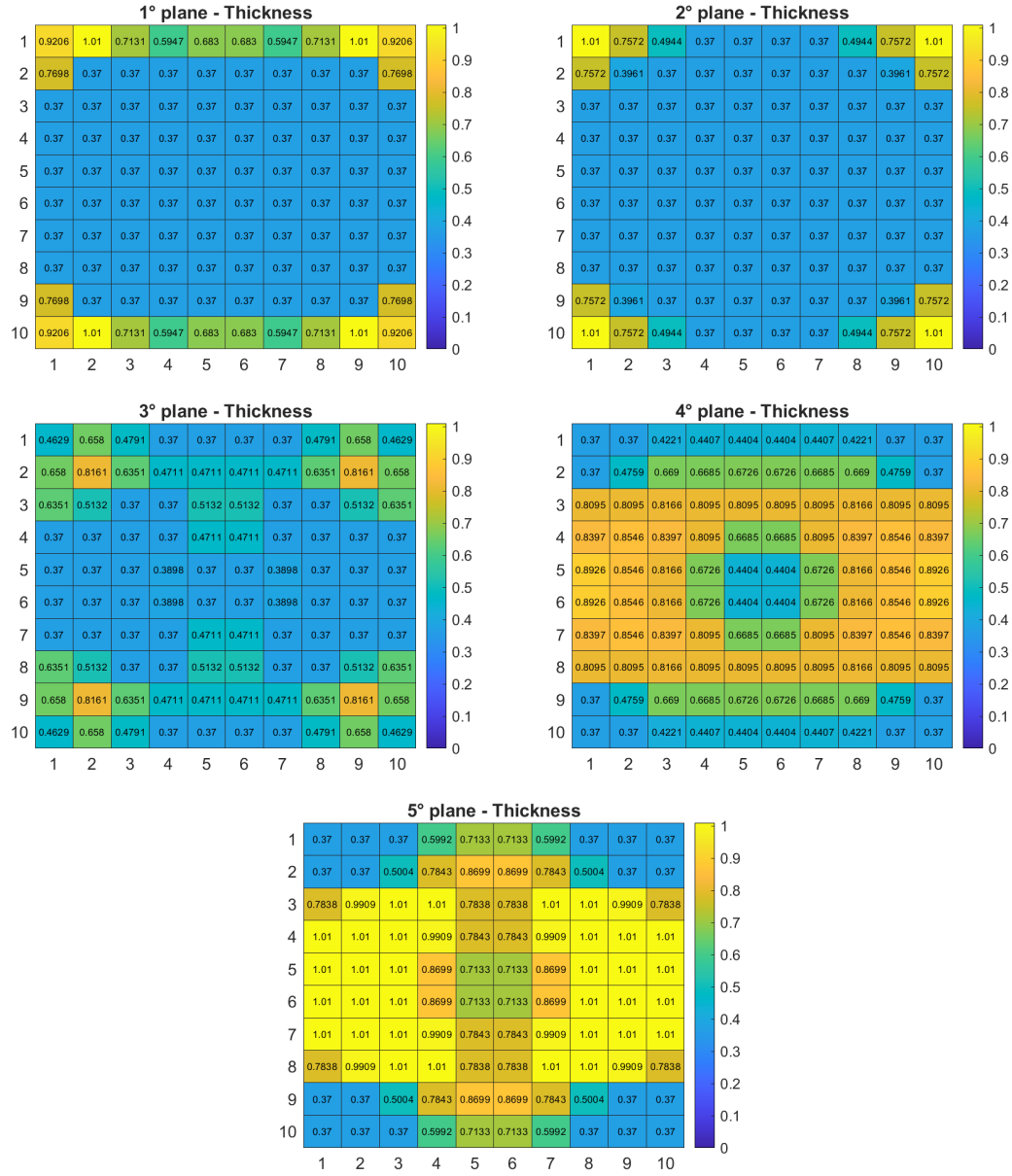


Figure B.2: Diameter of struts per cell - BCCZ1.

## B.2 Threshold equal to the mean value - Process 2

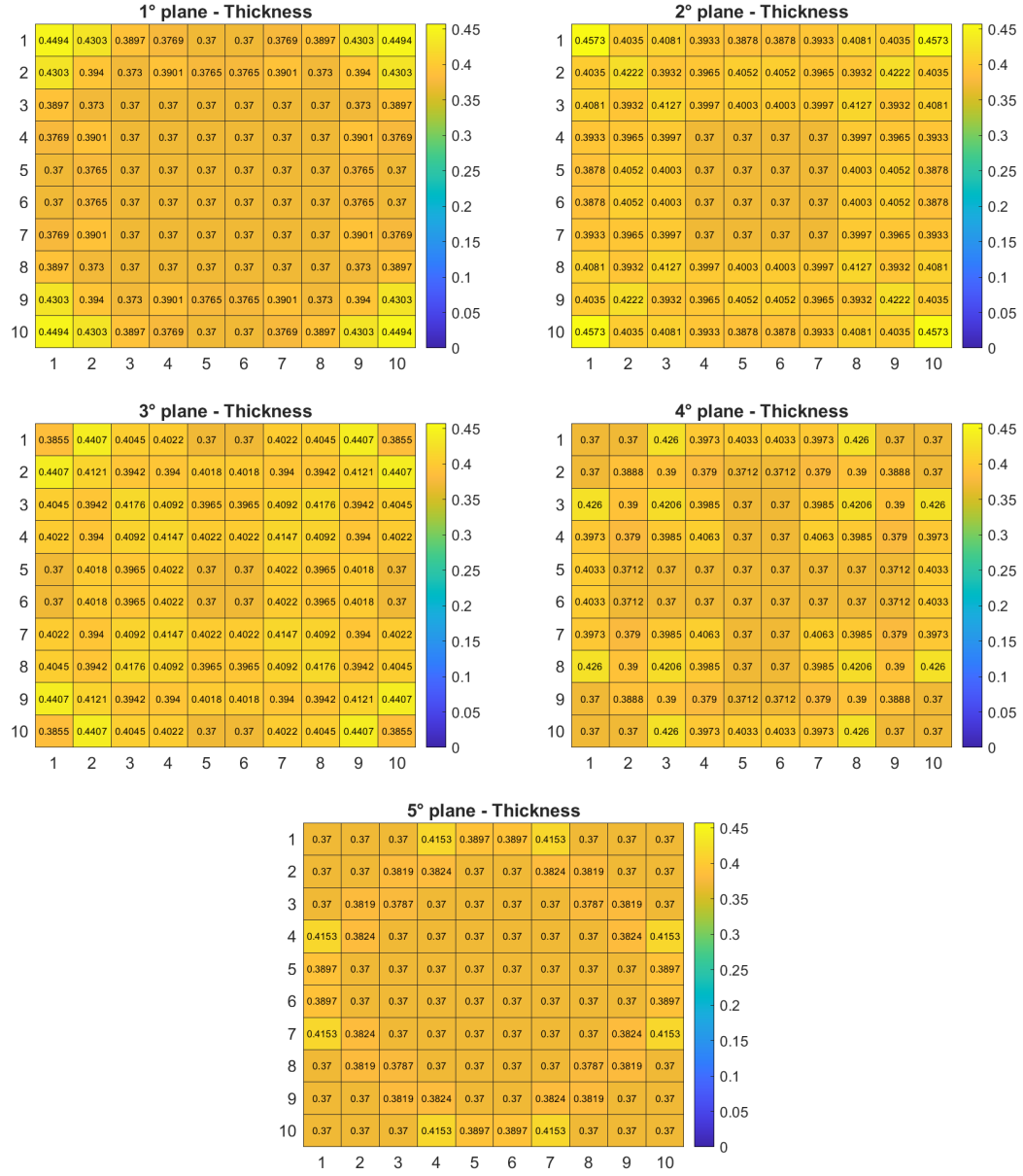


Figure B.3: Diameter of struts per cell - BCC2.

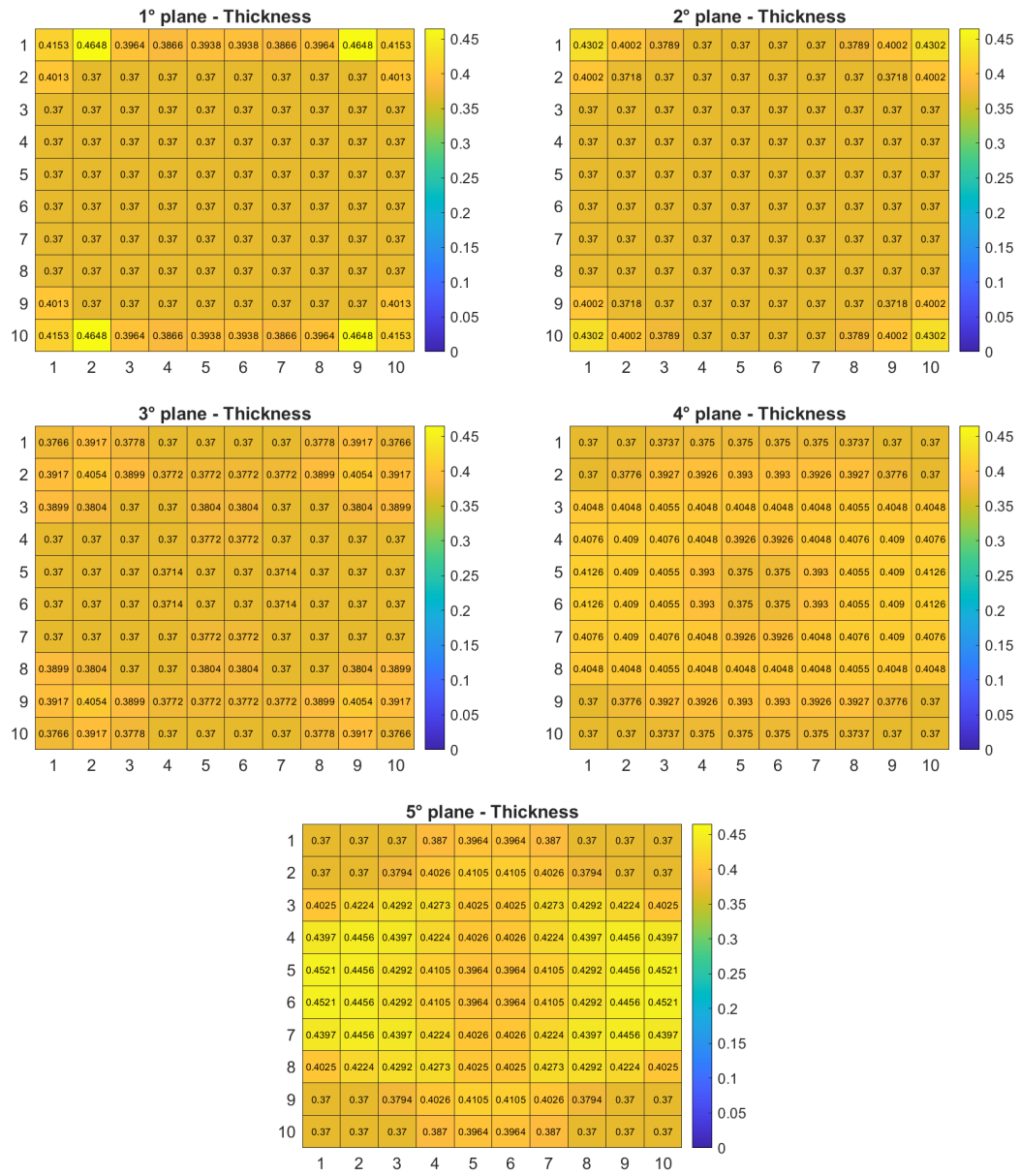


Figure B.4: Diameter of struts per cell - BCCZ2.

# Appendix C

## Optimized samples: SEA extraction in table format

### C.1 Threshold equal to the mean value - Process 1

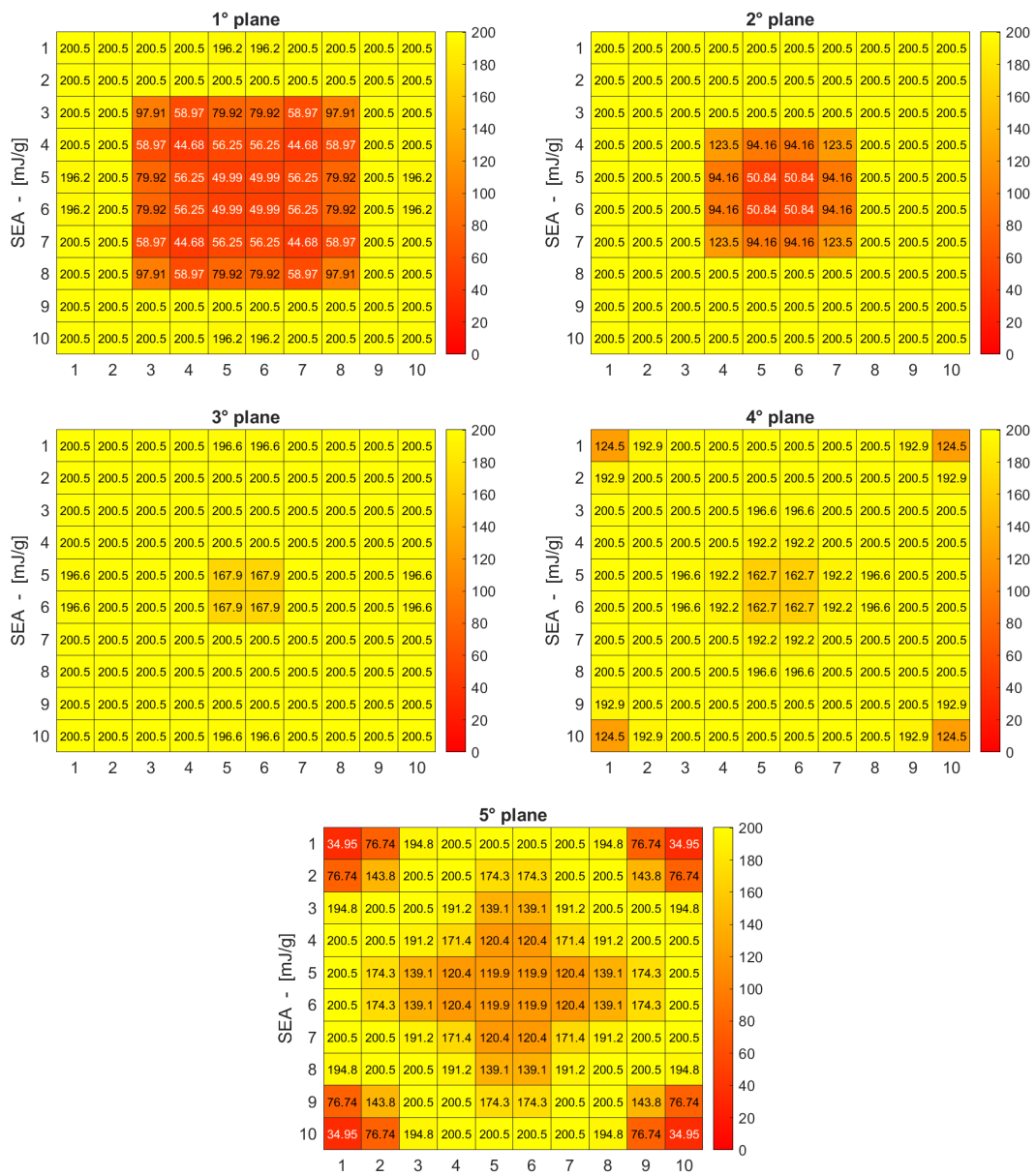


Figure C.1: SEA per cell - BCC1.



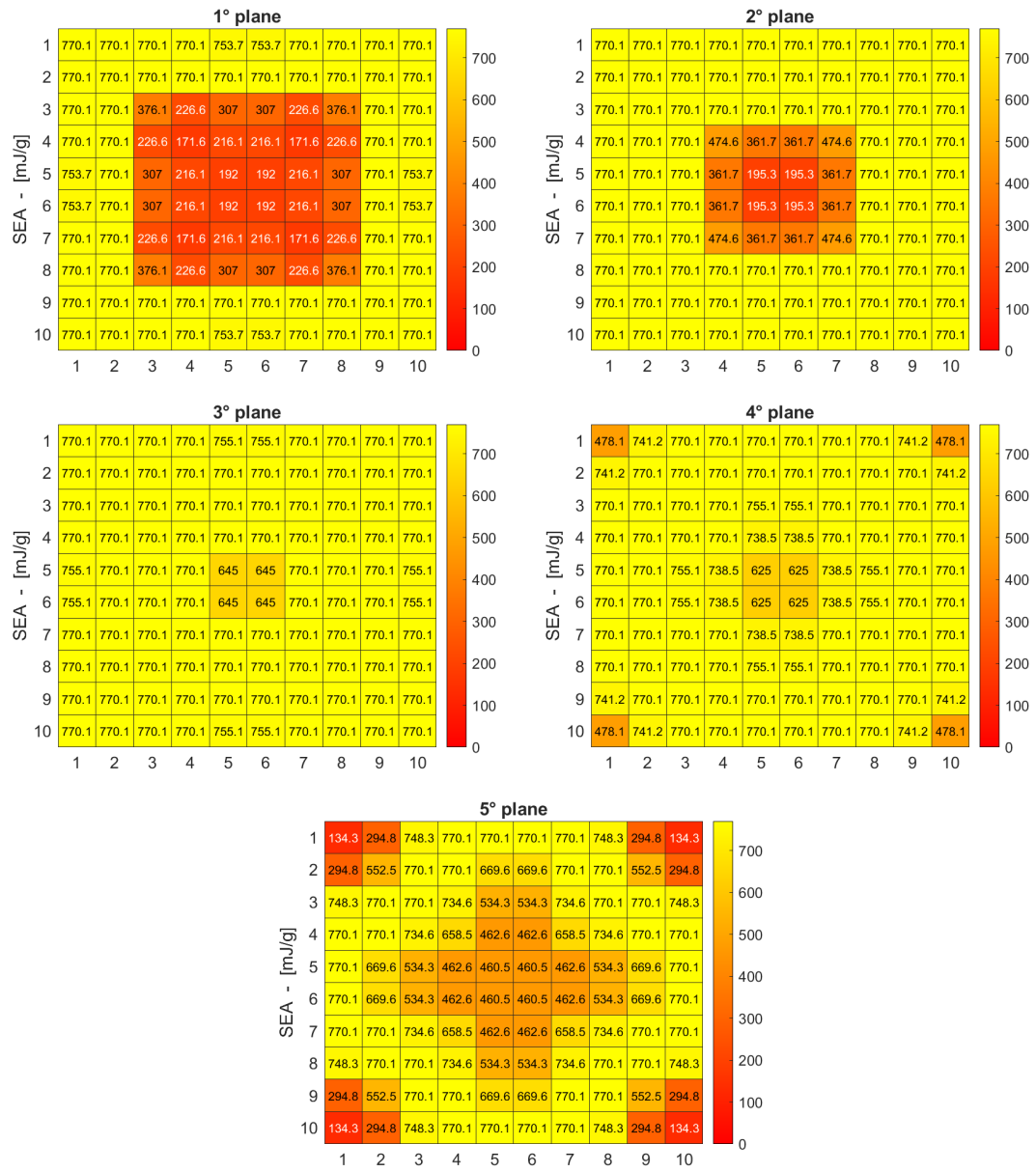


Figure C.2: SEA per cell - BCCZ1.

## C.2 Threshold equal to the mean value - Process 2

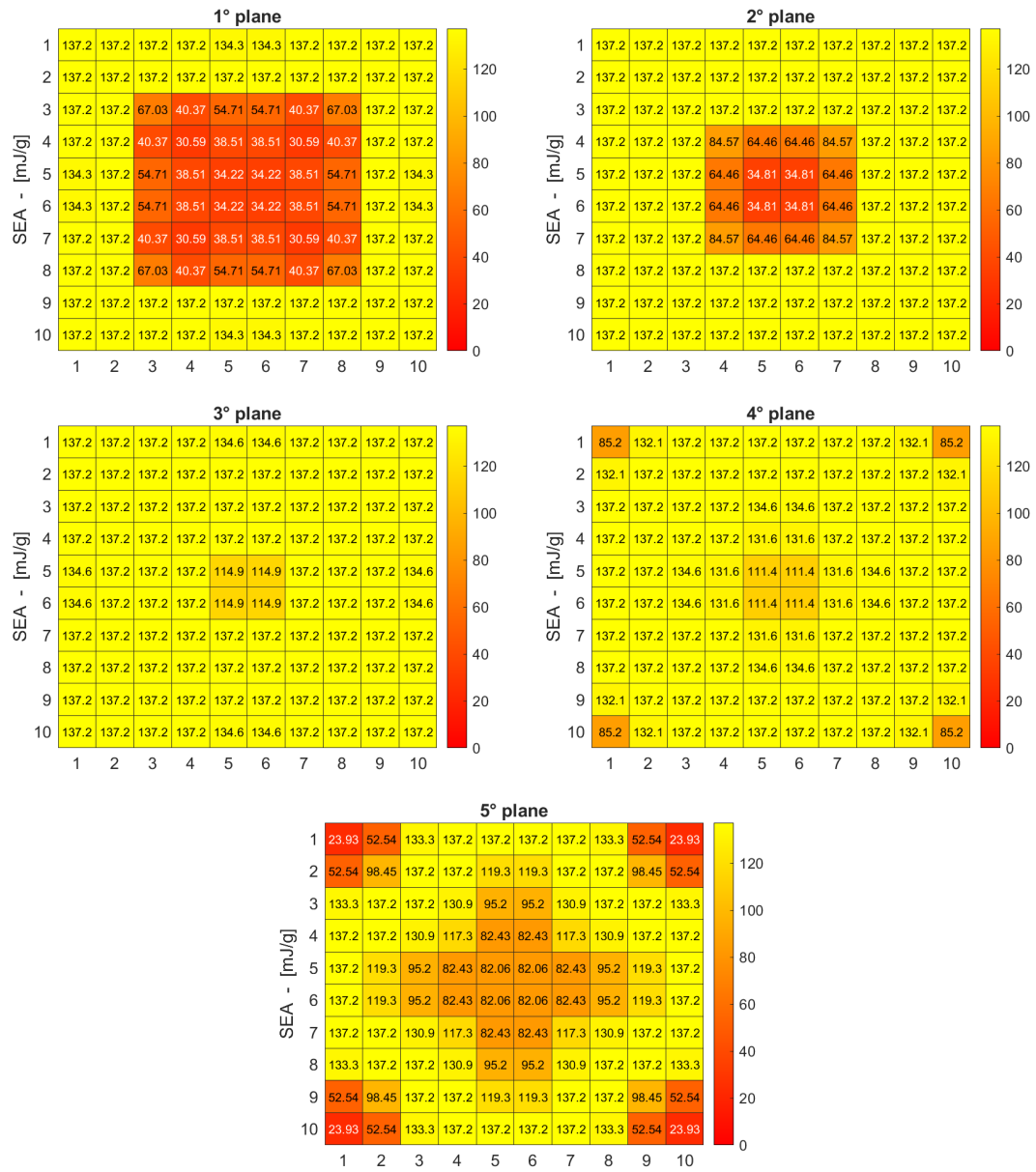


Figure C.3: SEA per cell - BCC2.

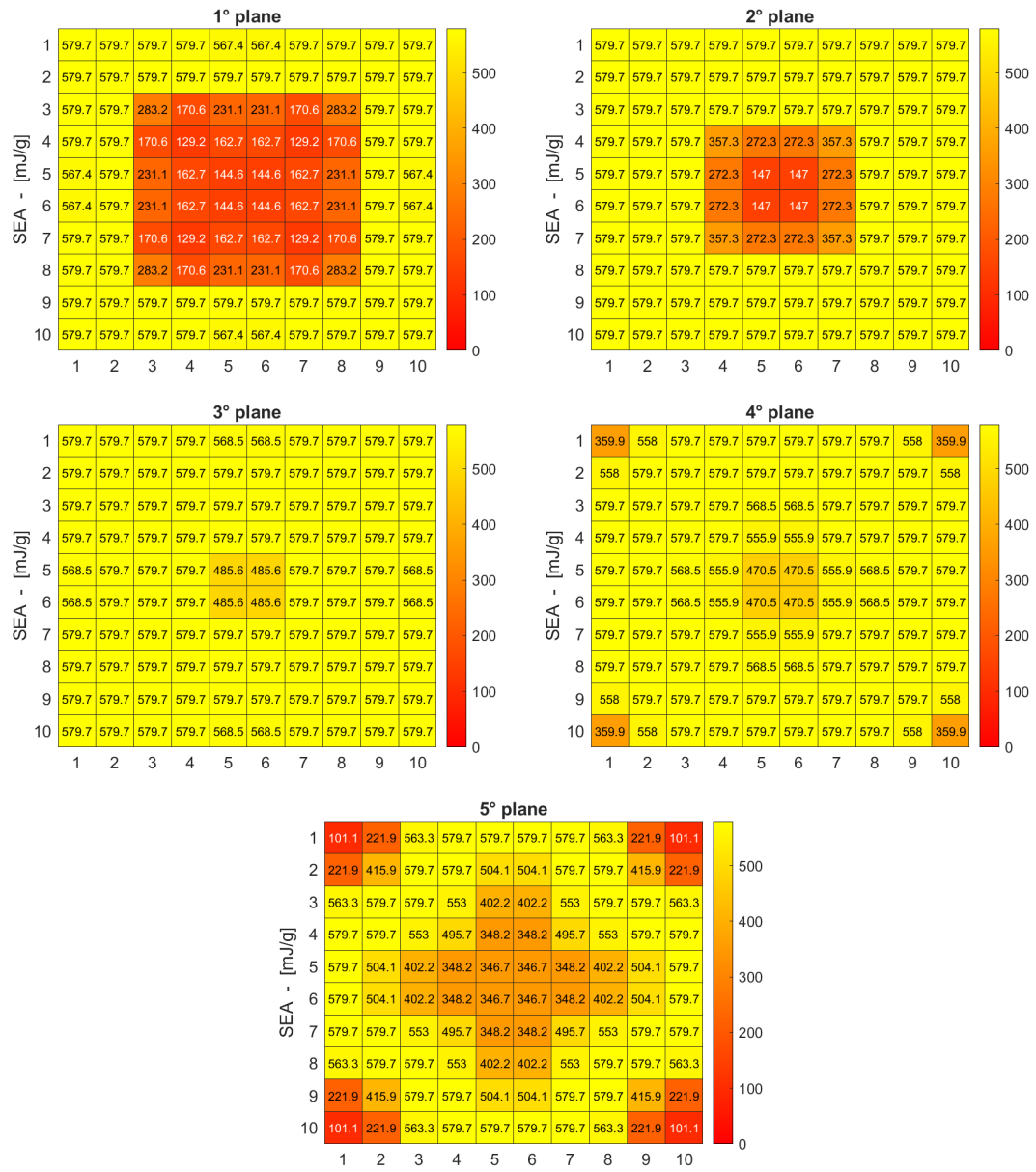


Figure C.4: SEA per cell - BCCZ2.

# Appendix D

## Optimized samples: VEA extraction in table format

### D.1 Threshold equal to the mean value - Process 1

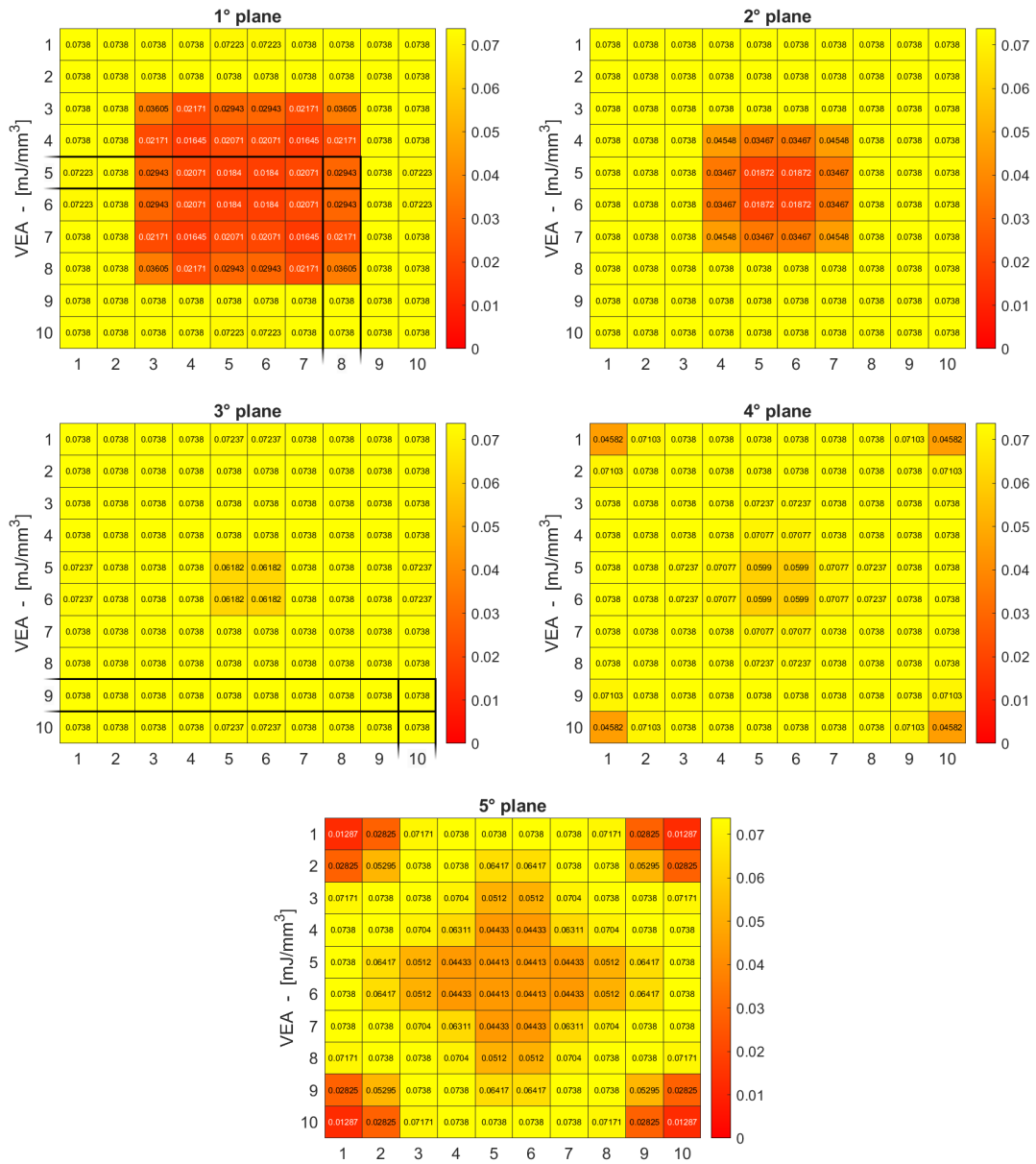


Figure D.1: VEA per cell - BCC1.

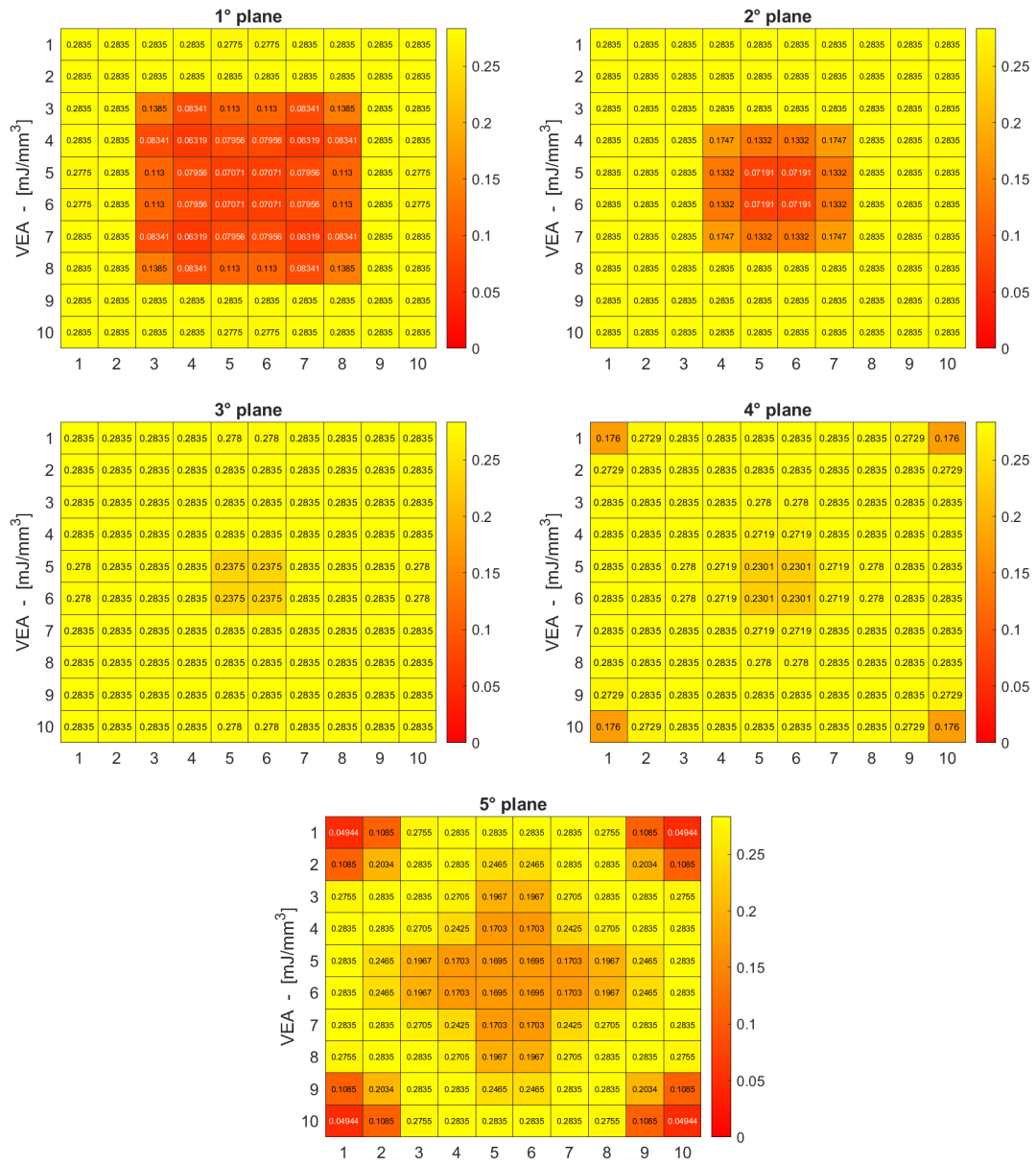


Figure D.2: VEA per cell - BCCZ1.

## D.2 Threshold equal to the mean value - Process 2

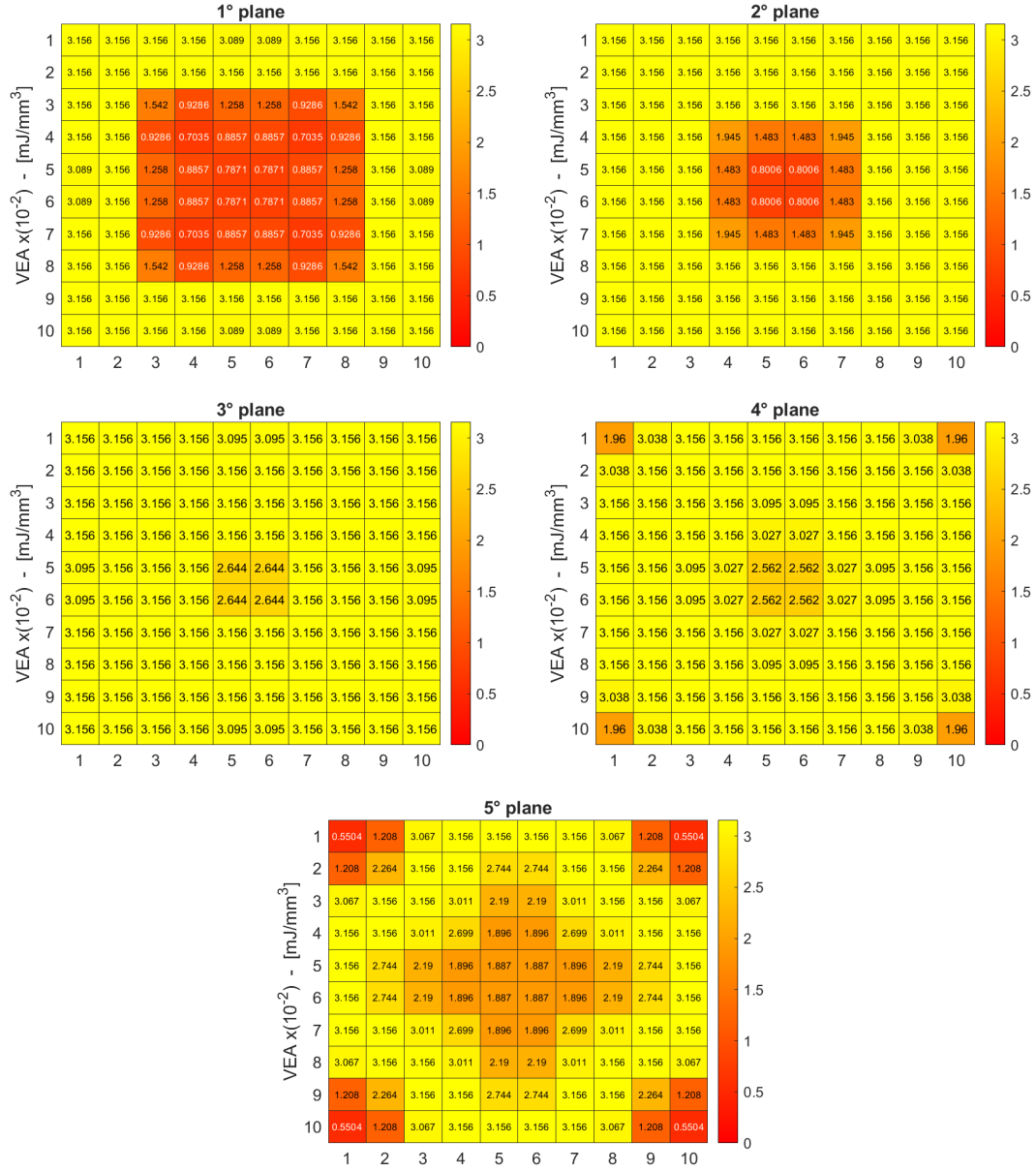


Figure D.3: VEA per cell - BCC2.

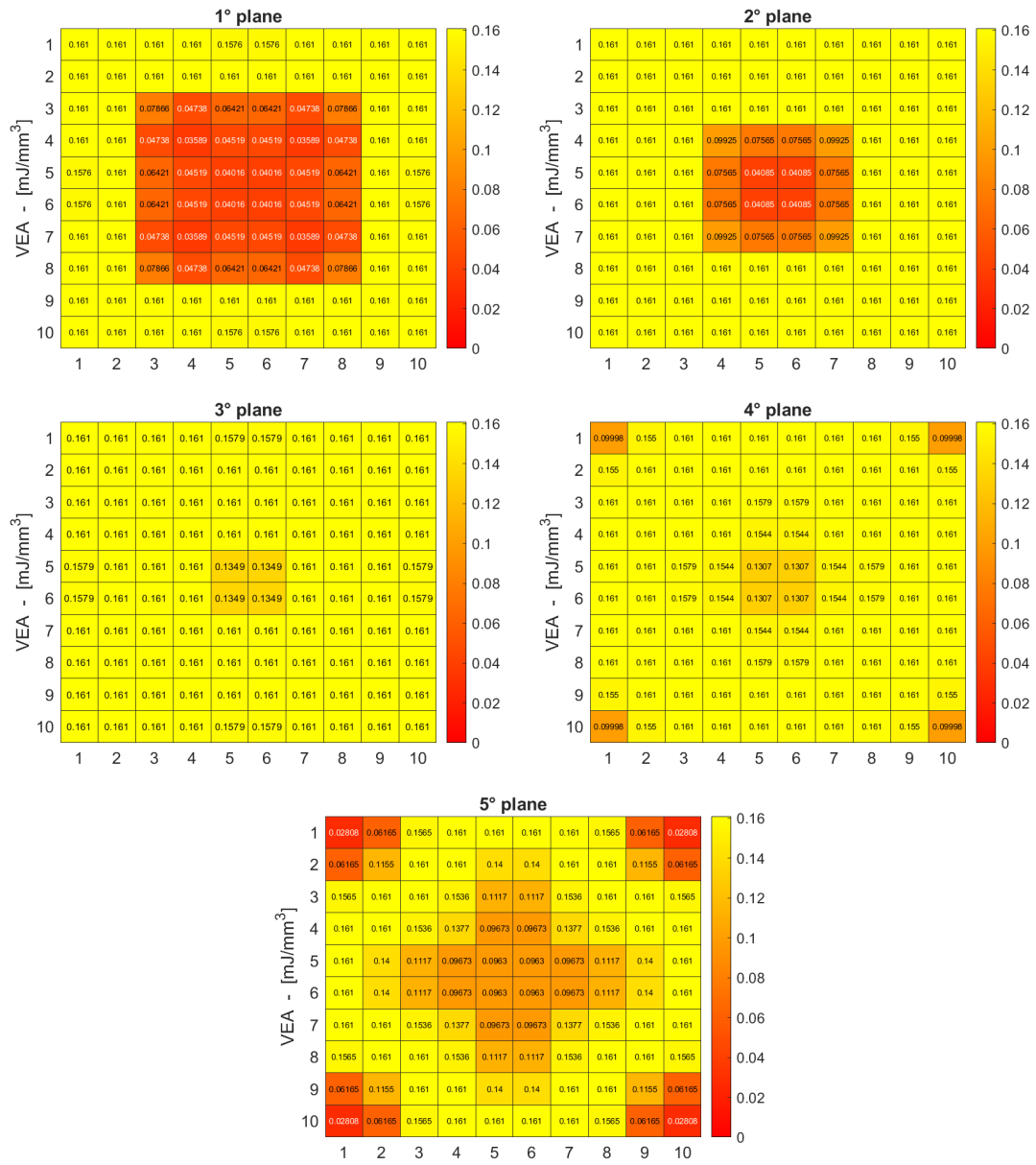


Figure D.4: VEA per cell - BCCZ2.

# Acknowledgments

First and foremost, I would like to express my immense gratitude to my supervisor Prof. De Pasquale for this opportunity, for the continuous guidance, and for believing in me from the beginning. It has been an honor and a pleasure to be your master thesis student.

Deepest thanks go to Dipl.-Ing. Meyer, this work would not have been possible without your constant support, teachings, and assistance. I am extremely thankful and indebted to you for the valuable guidance. Your approach to research and your dedication have taught me more than I expected.

I would like to render my warmest thanks to my co-tutor, Dott. Antonio Coluccia. Your friendly mentoring and expert advice have been essential throughout all stages of the work. Thank you for all the suggestions, for every meeting, and for sharing your immense passion for research. You have been a key reference point during all the activities, as a tutor, and as a friend.

I could not have undertaken this journey without my father, who taught me to get back up after every failure, and without my mother, for whom I try to improve every day to live up to her.

Special thanks to my half, Melania. I will never be thankful enough for having you in my life, you are my rock, the only certainty when nothing was certain.

Immense gratitude as always to Greta, Rosario, Rosanna, and Piero, for never leaving me alone, for making home every place I will be.

Another special thanks to Federica, Mauro, and Carmen for always believing in me and supporting me throughout my entire journey.

Finally, Mirko. You were always there, wherever and whenever that was. Each midnight wreck, each early morning rant, each time I smiled or cried. Your name should be on this thesis as much as mine.